Lecture Notes on Condensed Matter Physics

Bands, Transport, Magnetism
and Superconductivity

English edition

Course materials of Dong-Hui Xu
School of Physics, Chongqing University

Revised November 2026

Preface

Condensed matter physics studies collective behaviour in systems of many interacting particles. Periodic potentials determine electronic bands and wavefunctions, interactions produce magnetic and superconducting order, and external probes connect microscopic structure to electrical, thermal and optical observables. Spectra, symmetry, statistics and response provide a common language for understanding materials.

The classical Drude model describes conduction using free electrons and collisions, relating conductivity and the Hall coefficient to a relaxation time. Sommerfeld theory replaces classical statistics with Fermi statistics, explaining electronic heat capacity and low-temperature thermal transport while retaining the Drude conductivity for a parabolic band. Comparing the two theories separates the roles of classical dynamics and quantum statistics and exposes the limitations of the free-electron approximation in real crystals.

Band theory then introduces the periodic crystal potential. Translational symmetry and Bloch's theorem lead to calculable nearly-free-electron and tight-binding descriptions. The geometry of wavefunctions introduces Berry phases, Chern numbers and topological boundary states. Graphene, the SSH chain, Chern insulators and time-reversal-invariant topological insulators provide concrete applications of model construction, analytic solutions and numerical calculation.

With band structure established, semiclassical wavepackets and the Boltzmann equation describe orbital motion, scattering and thermoelectric response. Landau quantization, the Kubo formula and Landauer theory address quantum oscillations, interband transitions and coherent devices. Different measurements impose different constraints: oscillation frequencies determine extremal Fermi-surface areas, thermal damping gives cyclotron masses, and thermopower probes the energy dependence of scattering. Comparing these observables within one model helps establish its domain of validity.

Magnetism and superconductivity illustrate two central forms of interaction-driven order. Exchange models and Hubbard mean-field theory describe the self-consistent coupling between moments and electronic spectra, while spin groups express the symmetry constraints imposed by magnetic order. Cooper pairing, BCS theory and Bogoliubov–de Gennes equations describe superconductivity microscopically; London and Ginzburg–Landau theories connect it to electromagnetic response, vortices and critical fields. Unconventional pairing and topological superconductivity reveal how order-parameter symmetry and quasiparticle topology shape the low-energy physics.

Notation and units

Electrons carry charge $-e$, with $e > 0$. SI units apply unless lattice or dimensionless units are explicitly stated. The Berry connection is $\mathbf{A} = i\langle u|\nabla_k u\rangle$, the curvature is $\mathbf{\Omega} = \nabla_k \times \mathbf{A}$, and the Chern number of occupied two-dimensional bands is $C = (2\pi)^{-1}\int \Omega_z \,\mathrm{d}^2k$. We use $j_i = \sigma_{ij}E_j$, giving intrinsic Hall conductivity $\sigma_{xy} = -Ce^2/h$ for filled two-dimensional bands. Reversing the connection convention or the Hall-index order can reverse the displayed sign; definitions must therefore accompany comparisons.

Spin degeneracy is specified in each model. We denote chemical potential by μ, positive mobility by μ_{tr} or u, and transport, spectral, node-imbalance and coherence lifetimes by $\tau_{\mathrm{tr}}, \tau_q, \tau_v, \tau_\phi$. For superconductivity, ω_D is the pairing energy cutoff and ν_0 the density of states per spin.

Contents

Preface **i**

I Free electrons and transport foundations **1**

1 From an electron gas to measured transport coefficients **2**

1.1 Circuit quantities and material transport coefficients 2

1.2 Collision statistics and the Drude equation 2

1.3 Conductivity and resistivity tensors in a magnetic field 3

1.4 AC response and optical spectral weight 3

1.5 Limitations of classical thermal transport 4

1.6 Sommerfeld expansion and the thermally active electrons 4

1.7 DC conductivity with Fermi statistics 4

1.8 Exercises and solution notes 6

II Bands and topology **7**

2 Band theory: foundations and applications **8**

2.1 Direct and reciprocal lattices 8

2.2 Bloch theorem and the central equation 9

2.3 Nearly free electrons and Bragg gaps 9

2.4 Linear combinations of atomic orbitals and nonorthogonal bases 10

2.5 Wannier functions and second quantization 10

2.6 Square-lattice bands and density of states 11

2.7 Band-theory exercises and solution notes 12

2.8 Graphene and low-dimensional bands 12

3 Topological band theory and applications **16**

3.1 Landau levels and state counting 16

3.2 From Kubo sums to Berry curvature 16

3.3 Analytic geometry of a two-band Hamiltonian 17

3.4 Masses and phase boundaries of the Haldane model 17

3.5 The QWZ model and a discrete Chern number 18

3.6 Boundary spectra and the meaning of conductance 19

3.7 Chern-band exercises . . . 20
3.8 Topology protected by time reversal and crystal symmetries . . . 20

III Semiclassical and quantum transport 25

4 Motion and quantum geometry in periodic bands 26
4.1 From a Bloch eigenstate to a localized packet . . . 26
4.2 Bloch oscillations and scattering . . . 27
4.3 Position, Berry connection and anomalous velocity . . . 27
4.4 Orbital moments and phase-space state counting . . . 28
4.5 Exercises and solution notes . . . 28

5 Boltzmann transport and thermoelectric response 29
5.1 The Boltzmann equation and collision integral . . . 29
5.2 Trajectory history and the Chambers formula . . . 29
5.3 Heat current and thermoelectric response tensors . . . 30
5.4 Transport in compensated spin channels . . . 31
5.5 Intrinsic and scattering mechanisms of the anomalous Hall effect . . . 31
5.6 Berry-curvature dipoles and nonlinear Hall response . . . 31
5.7 Exercises and numerical implementation . . . 32
5.8 Finite-field transport and thermoelectric boundaries . . . 32

6 Quantum oscillations and band measurements in the quantum limit 35
6.1 Orbital deflection, Landau quantization and the quantum limit . . . 35
6.2 Landau levels and their degeneracy for a parabolic band . . . 35
6.3 Onsager quantization and Fermi-surface cross sections . . . 35
6.4 Deriving Lifshitz–Kosevich thermal damping . . . 36
6.5 Dingle damping and spin zeros . . . 36
6.6 Fermi-surface geometry and angular quantum oscillations . . . 37
6.7 Landau-fan phases and topological inference . . . 38
6.8 The graphene zero Landau level and Hall sequence . . . 38
6.9 Hall plateaux, localization and contacts . . . 38
6.10 Thermoelectric response in the Weyl quantum limit . . . 39
6.11 Exercises and solution notes . . . 41

7 Quantum response and transport through finite devices 42
7.1 Quantum coherence and interband response . . . 42
7.2 Density-matrix linear response and the Kubo formula . . . 42

7.3 Connecting intrinsic DC Hall response to band geometry . . . 43
7.4 Spin and orbital Hall response and observables . . . 43
7.5 Incident-state flux and the Landauer formula . . . 45
7.6 A Green-function algorithm for a finite tight-binding device . . . 45
7.7 Coherent corrections and weak-localization scales . . . 46
7.8 Analytic limits and numerical convergence . . . 46
7.9 Exercises and solution notes . . . 46

IV Magnetism 48

8 Foundations of Magnetism and Mean-Field Theory 49
8.1 Atomic moments and metallic susceptibility . . . 49
8.2 Exchange interactions, mean fields and spin waves . . . 52
8.3 Magnetic mean-field theory of the Hubbard model . . . 55
8.4 Mean-field applications to magnetic semiconductors and quantum wells . . . 58

9 Magnetic-Order Symmetry and Altermagnetism 63
9.1 Magnetic compensation and alternating splitting . . . 63
9.2 Magnetic space groups and spin space groups . . . 63
9.3 Symmetry conditions for degeneracy at the same momentum . . . 64
9.4 Alternating spin splitting and spin transport . . . 64
9.5 Spin-group classification and spin-orbit coupling . . . 66
9.6 Material evidence and low-dimensional magnetic order . . . 66
9.7 Symmetry breaking and magnetic stability . . . 67
9.8 Spin textures and the topological Hall response . . . 68
9.9 Bulk quantum oscillations of altermagnetic CrSb . . . 68

V Superconductivity 70

10 Superconductivity: foundations and applications 71
10.1 Experimental characteristics of superconductivity . . . 71
10.2 The Cooper problem and its binding energy . . . 72
10.3 Effective attractive interactions . . . 72
10.4 From a variational state to the mean-field Hamiltonian . . . 73
10.5 Bogoliubov transformation and quasiparticle spectra . . . 73
10.6 Finite-temperature gap and number equations . . . 74
10.7 Zero temperature and the transition temperature . . . 74
10.8 Free energy and thermodynamic checks . . . 76

10.9 Density of states and tunnelling coherence peaks 77
10.10 The attractive Hubbard model on a lattice band 77
10.11 Inhomogeneous Bogoliubov–de Gennes calculations 78
10.12 Microscopic-superconductivity exercises and solution notes 79
10.13 Superconducting electrodynamics and Ginzburg–Landau theory 79

11 Unconventional pairing and topological superconductivity **85**
11.1 Antisymmetry and the pairing matrix 85
11.2 Pairing as an eigenvalue problem 85
11.3 Nodal quasiparticles and low-temperature powers 86
11.4 Phase-sensitive evidence and interpretation in materials 86
11.5 BdG wavefunctions and topological classification 87
11.6 The Kitaev chain from a matrix to end modes 87
11.7 Two-dimensional chiral pairing and Majorana edge transport 88
11.8 From effective models to heterostructures 89
11.9 Experimental criteria for topological superconductivity 89
11.10 Unconventional and topological superconductivity: exercises 90

Part I

Free electrons and transport foundations

Chapter 1

From an electron gas to measured transport coefficients

Electronic transport connects microscopic spectra and scattering processes to resistance, Hall voltage, thermal conductivity and thermopower. The Drude model describes the competition between external driving and momentum relaxation; Sommerfeld theory introduces Fermi statistics and the distinct weights with which electrons contribute to charge and heat responses. Electrons carry charge $-e$, with $e > 0$, and SI units are used. The chemical potential is μ; a positive mobility is μ_{tr}. With $j_i = \sigma_{ij} E_j$, the measured Hall coefficient $E_y/(j_x B_z)$ is negative in the isotropic single-electron-band Drude model.

1.1 Circuit quantities and material transport coefficients

For a uniform bar of length L and cross-sectional area A, $I = jA$ and $V = EL$. Combining these relations with $j = \sigma E$ gives $R = \rho L/A$. Resistance depends on geometry; only $\rho = 1/\sigma$ is the scalar material coefficient. In a two-dimensional device, use sheet current and sheet conductivity: $G = \sigma_{2D} W/L$. A sheet conductivity in siemens should not be turned into a three-dimensional conductivity by inserting an arbitrary thickness. Four-terminal measurements reduce contact-voltage contributions, but do not automatically remove inhomogeneous current flow, probe-position effects or current jetting.

1.2 Collision statistics and the Drude equation

Let a momentum-randomizing collision occur with probability $\mathrm{d}t/\tau$ in a short interval. Electrons that do not collide acquire the external impulse, while the mean drift momentum of the collided population is set to zero. The population-weighted average, keeping first-order terms, gives

$$\langle \mathbf{p}(t + \mathrm{d}t) \rangle = (1 - \mathrm{d}t/\tau)[\langle \mathbf{p}(t) \rangle + \mathbf{F}\mathrm{d}t], \tag{1.1}$$

$$\frac{\mathrm{d}\mathbf{p}}{\mathrm{d}t} = -e(\mathbf{E} + \mathbf{v} \times \mathbf{B}) - \frac{\mathbf{p}}{\tau}, \qquad \mathbf{j} = -ne\mathbf{v}. \tag{1.2}$$

Here τ relaxes electric current; it need not equal the time between all microscopic scattering events. Forward scattering can broaden a spectral line while relaxing current only weakly. The distinction follows from different angular weights in the collision integral. At zero field, the stationary solution is $\mathbf{v}_d = -e\tau\mathbf{E}/m$ and $\sigma_0 = ne^2\tau/m$. The drift velocity is normally far below the Fermi velocity. The two velocities cannot be interchanged when estimating a mean free path.

1.2.1 Worked example T1 Copper resistivity and microscopic parameters

Take the parameters $n = 8.5 \times 10^{28}\,\mathrm{m}^{-3}$, $\rho = 1.7 \times 10^{-8}\,\Omega\mathrm{m}$, $m = m_e$ and $T = 300\,\mathrm{K}$. First infer a relaxation time from resistivity; then determine a speed by quantum state counting:

$$\tau = \frac{m_e}{ne^2\rho} = 2.456 \times 10^{-14}\,\mathrm{s}, \qquad k_F = (3\pi^2 n)^{1/3} = 1.360 \times 10^{10}\,\mathrm{m}^{-1}, \tag{1.3}$$

$$E_F = \frac{\hbar^2 k_F^2}{2m_e} = 7.049\,\mathrm{eV}, \qquad T_F = E_F/k_B = 8.180 \times 10^4\,\mathrm{K}, \tag{1.4}$$

$$v_F = \hbar k_F/m_e = 1.575 \times 10^6\,\mathrm{m\,s}^{-1}, \qquad \ell = v_F\tau = 38.67\,\mathrm{nm}. \tag{1.5}$$

For $j = 10^6\,\mathrm{A\,m}^{-2}$, $|v_d| = j/(ne) = 7.34 \times 10^{-5}\,\mathrm{m\,s}^{-1}$, roughly ten orders of magnitude below v_F. A one-metre wire with $A = 1\,\mathrm{mm}^2$ has $R = 0.017\,\Omega$. These observables follow from the same density, mass and scattering parameters. The actual copper Fermi surface is not a free-electron sphere, so this is a leading estimate within the free-electron approximation. A resistivity measurement alone constrains $n\tau/m$, not all three factors independently.

1.3 Conductivity and resistivity tensors in a magnetic field

Let $\mathbf{B} = B\hat{z}$ and $\omega_c = eB/m$. The steady Drude equation is a pair of coupled linear equations. Its inverse gives

$$\boldsymbol{\sigma} = \frac{\sigma_0}{1 + (\omega_c\tau)^2}\begin{pmatrix} 1 & -\omega_c\tau \\ \omega_c\tau & 1 \end{pmatrix}, \tag{1.6}$$

$$\boldsymbol{\rho} = \boldsymbol{\sigma}^{-1} = \frac{1}{\sigma_0}\begin{pmatrix} 1 & \omega_c\tau \\ -\omega_c\tau & 1 \end{pmatrix}. \tag{1.7}$$

Consequently $\rho_{xx} = m/(ne^2\tau)$ is independent of field, while $\rho_{yx} = -B/(ne)$. This is exact within the isotropic one-band, constant-τ model. Although σ_{xx} decreases with field, the Hall field redirects the current. Thus $1/\sigma_{xx}$ is not the longitudinal resistivity under an open transverse boundary. The copper inputs give $R_H = -7.34 \times 10^{-11}\,\mathrm{m}^3\,\mathrm{C}^{-1}$; a real Hall coefficient also tests Fermi-surface shape and scattering.

1.4 AC response and optical spectral weight

With the convention $e^{-i\omega t}$, Eq. (1.2) at $B = 0$ yields

$$\sigma(\omega) = \frac{ne^2\tau/m}{1 - i\omega\tau}, \qquad \mathrm{Re}\,\sigma = \frac{\sigma_0}{1 + \omega^2\tau^2}, \quad \mathrm{Im}\,\sigma = \frac{\sigma_0\omega\tau}{1 + \omega^2\tau^2}, \tag{1.8}$$

$$\epsilon_r(\omega) = \epsilon_\infty + \frac{i\sigma(\omega)}{\epsilon_0\omega} = \epsilon_\infty - \frac{\omega_p^2}{\omega(\omega + i/\tau)}, \qquad \omega_p^2 = \frac{ne^2}{\epsilon_0 m}, \tag{1.9}$$

$$\int_0^\infty \mathrm{Re}\,\sigma(\omega)\,\mathrm{d}\omega = \frac{\pi ne^2}{2m}. \tag{1.10}$$

Scattering changes the height and width of the peak without changing its integrated Drude weight in this model. Combining an optical width and a DC resistivity can therefore constrain τ and n/m separately. The

T1 inputs give $\omega_p = 1.645 \times 10^{16}\,\mathrm{s}^{-1}$, $\hbar\omega_p \simeq 10.83\,\mathrm{eV}$ and $1/(2\pi\tau) = 6.48\,\mathrm{THz}$. A measured reflectivity edge also depends on background screening, interband transitions and band masses; it is not automatically the bare plasma energy.

1.5 Limitations of classical thermal transport

A classical gas gives $C_V/V = 3nk_B/2$, and kinetic theory estimates $\kappa \sim C_V v^2\tau/3$. Using $v^2 = 3k_BT/m$ gives $\kappa/(\sigma T) \sim (3/2)(k_B/e)^2$. Its superficially reasonable scale hides two incorrect inputs: the classical heat capacity and the classical thermal speed. More precisely, a three-dimensional parabolic band with $\tau(\epsilon) \propto \epsilon^r$ has a spectral conductivity $\Sigma(\epsilon) \propto \epsilon^{r+3/2}$. With Maxwell occupation, the current-weighted mean energy is $(r + 5/2)k_BT$ and its variance is $(r + 5/2)(k_BT)^2$. Under the zero-current thermal boundary, this yields

$$S_{\mathrm{MB}} = -\frac{k_B}{e}\left(r + \frac{5}{2} - \frac{\mu}{k_BT}\right), \qquad L_{\mathrm{MB}} = \frac{\kappa}{\sigma T} = \left(r + \frac{5}{2}\right)\left(\frac{k_B}{e}\right)^2. \tag{1.11}$$

The integrals must converge at the band bottom. For $r = 0$, the precise classical Lorenz ratio is $5(k_B/e)^2/2$, rather than the elementary kinetic estimate above. A metal is not a dilute Maxwell gas. Applying this expression at $T \ll T_F$ already violates its premise. Fermi occupation is needed to explain the electronic heat capacity and the microvolt-per-kelvin scale of metallic thermopower.

1.6 Sommerfeld expansion and the thermally active electrons

State counting for a spin-degenerate three-dimensional gas gives $N/V = 2\int_{k<k_F} \mathrm{d}^3k/(2\pi)^3$. Its density of states includes both spins: $\nu(E_F) = 3n/(2E_F)$. For a function Φ smooth around μ, subtract the zero-temperature step, set $x = (\epsilon - \mu)/(k_BT)$, and use parity to obtain

$$\int \Phi(\epsilon) f(\epsilon)\,\mathrm{d}\epsilon = \int^{\mu} \Phi(\epsilon)\,\mathrm{d}\epsilon + \frac{\pi^2}{6}(k_BT)^2\Phi'(\mu) + O(T^4), \tag{1.12}$$

$$\mu(T) = E_F\left[1 - \frac{\pi^2}{12}\left(\frac{T}{T_F}\right)^2 + \cdots\right], \tag{1.13}$$

$$\frac{C_V}{V} = \frac{\pi^2}{3}k_B^2T\nu(E_F) = \frac{\pi^2}{2}nk_B\frac{T}{T_F}. \tag{1.14}$$

At fixed particle number, solve for $\mu(T)$ before differentiating the internal energy. Artificially fixing μ gives an inconsistent heat capacity. Only electrons in an energy window of order k_BT can change occupation, but their characteristic speed remains v_F. T1 gives $C_V/V \simeq 2.12 \times 10^4\,\mathrm{J\,m^{-3}K^{-1}}$, compared with the classical 1.76×10^6, a factor of about 83. This is the electronic contribution; the room-temperature total also contains a large lattice contribution.

1.7 DC conductivity with Fermi statistics

An electric field produces $\delta f = -e\tau E_x v_x(-\partial f/\partial\epsilon)$. Hence

$$\sigma_{xx} = e^2\tau \int \frac{\mathrm{d}^3k}{(2\pi)^3}\, g_s v_x^2 \left(-\frac{\partial f}{\partial \epsilon}\right) \xrightarrow{T\to 0} \frac{e^2\tau}{3}\nu(E_F)v_F^2 = \frac{ne^2\tau}{m}. \tag{1.15}$$

The identical coefficient does not validate the classical occupation used by Drude. A displaced Fermi sea changes occupations near its boundary; $\nu(E_F)v_F^2/3 = n/m$ is an identity specific to a parabolic band. For nonparabolic, multiband or anisotropic materials, retain the integral.

1.7.1 Worked example T2 Thermal conductivity and thermopower of the same model

With elastic scattering in the degenerate regime, the Sommerfeld expansion of energy moments gives

$$L_0 = \frac{\pi^2 k_B^2}{3e^2} = 2.443 \times 10^{-8}\,\mathrm{W\,\Omega\,K^{-2}}, \qquad S = -\frac{\pi^2 k_B^2 T}{3e}\left.\frac{\mathrm{d}\ln\Sigma}{\mathrm{d}\epsilon}\right|_{\mu}. \tag{1.16}$$

Thus $\kappa_e = L_0 T/\rho = 431\,\mathrm{W\,m^{-1}K^{-1}}$. If τ is energy independent, $\Sigma \propto \epsilon^{3/2}$ and $S = -1.56\,\mu\mathrm{V/K}$. If the mean free path is constant, $\tau \propto \epsilon^{-1/2}$ and $S = -1.04\,\mu\mathrm{V/K}$. The metallic scale is reasonable, but a positive measured copper thermopower in part of its temperature range is not explained. Its actual band structure and energy-dependent scattering are missing. The discrepancy reflects the limits of the free-electron approximation for the sign of thermopower.

Electronic heat capacity and the Lorenz coefficient provide complementary tests of classical and degenerate electron descriptions (Fig. 1.1).

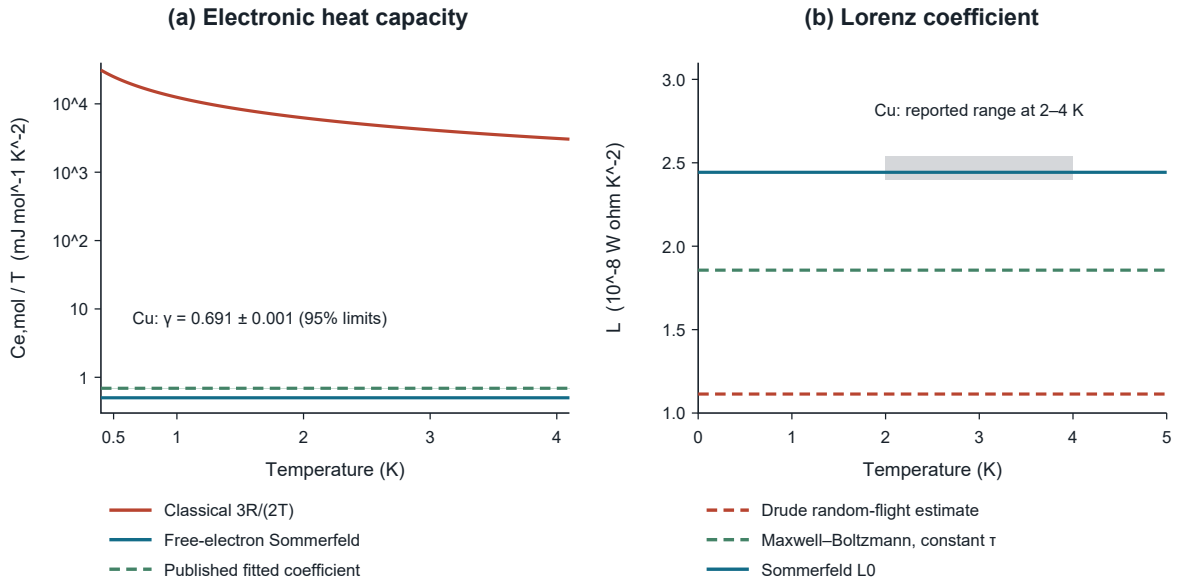

Figure 1.1: Electronic heat capacity and Lorenz coefficient of copper. (a) Classical and Sommerfeld predictions for $C_{e,\mathrm{mol}}/T$; the green band represents the experimental fitted coefficient $\gamma = 0.691 \pm 0.001\,\mathrm{mJ\,mol^{-1}K^{-2}}$ with 95% statistical limits. (b) Theoretical Lorenz coefficients and the reported high-purity copper range $(2.40\text{–}2.54) \times 10^{-8}\,\mathrm{W\,\Omega\,K^{-2}}$ at 2–4 K (grey rectangle). The band and rectangle represent a fitted parameter and a reported range, respectively, rather than temperature-resolved experimental traces.[53, 54]

The fit $C_{\mathrm{mol}} = \gamma T + \beta T^3 + \cdots$ separates electronic and lattice contributions. The classical increase $C_e/T \propto 1/T$ is inconsistent with experiment. Sommerfeld theory gives an approximately constant coefficient, but the free-electron estimate $\gamma \simeq 0.502\,\mathrm{mJ\,mol^{-1}K^{-2}}$ remains below the measured value, reflecting

the actual band density of states and renormalization. In the right panel, L_0 lies within the reported range, supporting the Wiedemann–Franz relation under nearly elastic low-temperature conditions. Phonon contributions must still be separated from thermal conductivity; agreement in this regime does not establish the relation at arbitrary temperature.

Copper thermopower further tests the energy dependence of the transport spectrum (Fig. 1.2).

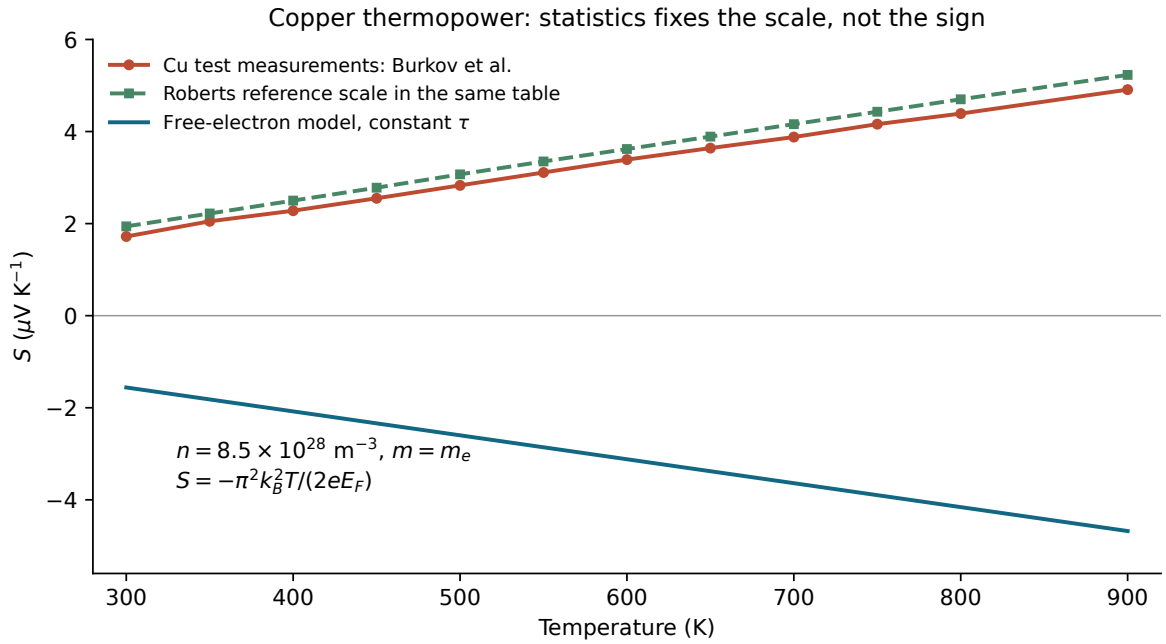

Figure 1.2: Copper Seebeck coefficient. Circles are the test measurements in Table 2 of Burkov et al.; squares are the Roberts reference-scale values in the same table. Connecting segments guide the eye. The blue curve is the constant-τ free-electron prediction $S = -\pi^2 k_B^2 T/(2eE_F)$ for $n = 8.5 \times 10^{28}\,\mathrm{m}^{-3}$ and $m = m_e$. Measurement and model have comparable magnitudes but opposite signs.[55]

At 300 K, the test value is $+1.72\,\mu\mathrm{V/K}$ and the reference-scale value is $+1.94\,\mu\mathrm{V/K}$, both opposite in sign to the free-electron prediction. Fermi statistics sets the small scale controlled by $k_B T/E_F$, whereas the sign depends on $\partial_\epsilon \ln \Sigma$ in the Mott relation. Band velocities, the density of states and energy-dependent scattering all enter this derivative; phonon drag can also matter in some temperature ranges. Seebeck and ordinary Hall coefficients weight states differently, so positive thermopower alone does not identify a single hole band.

1.8 Exercises and solution notes

1. Double resistivity at fixed density and mass. Which T1 quantities change? Solution: τ, ℓ and σ halve; k_F, E_F, T_F, v_F stay fixed. If heating caused the change, the scattering energy dependence need not remain fixed.

2. Verify the electron Hall sign directly from ρ, and check $\rho\sigma = I$.

3. Derive $\int x^2[-f'(x)]\mathrm{d}x = \pi^2/3$. Explain why a sharp band edge invalidates direct use of the Mott relation. Solution: Σ must be smooth throughout a $k_B T$ window; near edges, resonances or small gaps, integrate the full moments.

Part II

Bands and topology

Chapter 2

Band theory: foundations and applications

The Drude model describes conduction using classical free electrons and a relaxation time. The Sommerfeld model introduces Fermi statistics to account for electron degeneracy and low-temperature thermodynamics. A free-electron dispersion, however, cannot directly explain band gaps, anisotropy, or complex Fermi surfaces in crystals. Once the periodic lattice potential is included, translation symmetry converts the real-space Schrödinger equation into an eigenvalue problem over the Brillouin zone. The eigenvalues determine the density of states, effective masses, and Fermi surfaces; the eigenvectors determine transition matrix elements, boundary responses, and band geometry. Bloch theory, the nearly-free-electron approximation, and tight binding provide the foundations, while graphene, the SSH chain, and moiré bands illustrate applications at different scales. We use $e > 0$ and electron charge $-e$. A band does not implicitly include spin degeneracy unless stated.

2.1 Direct and reciprocal lattices

A lattice translation is $\mathbf{R} = \sum_i n_i \mathbf{a}_i$. A crystal places the same basis in every translation-equivalent cell. The honeycomb structure has a two-atom basis and is not a one-atom Bravais lattice. Fourier components of a periodic function satisfy $e^{i\mathbf{G}\cdot\mathbf{R}} = 1$, hence $\mathbf{G} = \sum_i m_i \mathbf{b}_i$ and $\mathbf{a}_i \cdot \mathbf{b}_j = 2\pi\delta_{ij}$. In three dimensions,

$$\mathbf{b}_1 = 2\pi \frac{\mathbf{a}_2 \times \mathbf{a}_3}{\mathbf{a}_1 \cdot (\mathbf{a}_2 \times \mathbf{a}_3)}, \tag{2.1}$$

with cyclic expressions for the other two vectors. The first Brillouin zone is the reciprocal Wigner–Seitz cell, with volume $(2\pi)^d/v_c$. Changing reciprocal primitive vectors also changes coordinates. Identical labels for high-symmetry points in two papers do not guarantee identical coordinate conventions.

2.1.1 Example B1 Reciprocal space of the triangular Bravais lattice

Using the carbon bond length a_0, choose $\mathbf{a}_1 = a_0(3, \sqrt{3})/2$ and $\mathbf{a}_2 = a_0(3, -\sqrt{3})/2$. Direct multiplication verifies

$$\mathbf{b}_1 = \frac{2\pi}{3a_0}(1, \sqrt{3}), \quad \mathbf{b}_2 = \frac{2\pi}{3a_0}(1, -\sqrt{3}), \quad v_c = \frac{3\sqrt{3}}{2}a_0^2. \tag{2.2}$$

For $a_0 = 0.142\,\text{nm}$, the cell area is $0.05239\,\text{nm}^2$. This is not the area per atom: a graphene cell contains two carbon atoms. Before computing a carrier density, specify whether states are counted per cell, per atom, or per area. This example checks the normalization of graphene's density of states and explains the spurious factors of $\sqrt{3}$ produced by confusing the bond length $0.142\,\text{nm}$ with the lattice constant $0.246\,\text{nm}$.

2.2 Bloch theorem and the central equation

Consider the effective one-electron Hamiltonian

$$H = \frac{\mathbf{p}^2}{2m} + U(\mathbf{r}), \qquad U(\mathbf{r}+\mathbf{R}) = U(\mathbf{r}). \tag{2.3}$$

Define $T_{\mathbf{R}}\psi(\mathbf{r}) = \psi(\mathbf{r}+\mathbf{R})$. Since $[H, T_{\mathbf{R}}] = 0$ and lattice translations commute with one another, simultaneous eigenstates can be chosen. Unitarity and $T_{\mathbf{R}}T_{\mathbf{R}'} = T_{\mathbf{R}+\mathbf{R}'}$ require translation eigenvalues $e^{i\mathbf{k}\cdot\mathbf{R}}$. Thus

$$\psi_{n\mathbf{k}}(\mathbf{r}) = e^{i\mathbf{k}\cdot\mathbf{r}}u_{n\mathbf{k}}(\mathbf{r}), \qquad u_{n\mathbf{k}}(\mathbf{r}+\mathbf{R}) = u_{n\mathbf{k}}(\mathbf{r}). \tag{2.4}$$

The labels $\mathbf{k}$ and $\mathbf{k}+\mathbf{G}$ specify the same translation representation. Their eigenfunctions can be related by a gauge choice; eigenvectors returned by an arbitrary numerical solver need not have identical phases.

Born–von Karman conditions $\psi(\mathbf{r}+N_i\mathbf{a}_i) = \psi(\mathbf{r})$ give $\mathbf{k} = \sum_i (m_i/N_i)\mathbf{b}_i$. With $N = \prod_i N_i$ cells, each nondegenerate band contains exactly N allowed $\mathbf{k}$ states. A spin-degenerate orbital band accommodates $2N$ electrons.

Insert $U = \sum_{\mathbf{G}} U_{\mathbf{G}} e^{i\mathbf{G}\cdot\mathbf{r}}$ and $\psi = \sum_{\mathbf{G}} c_{\mathbf{G}} e^{i(\mathbf{k}+\mathbf{G})\cdot\mathbf{r}}$ into the Schrödinger equation. Equating plane-wave coefficients yields

$$\sum_{\mathbf{G}'} \left[\frac{\hbar^2|\mathbf{k}+\mathbf{G}|^2}{2m}\delta_{\mathbf{G}\mathbf{G}'} + U_{\mathbf{G}-\mathbf{G}'} \right] c_{\mathbf{G}'} = E c_{\mathbf{G}}. \tag{2.5}$$

This central equation becomes a finite matrix after imposing a kinetic-energy cutoff $\hbar^2|\mathbf{k}+\mathbf{G}|^2/(2m) < E_{\mathrm{cut}}$. Increase the cutoff until the bands of interest change by less than the prescribed tolerance. A visually smooth band plot does not establish basis convergence.

2.2.1 Crystal momentum and mechanical momentum

In general, $\hbar\mathbf{k}$ is not a mechanical-momentum eigenvalue, because $\mathbf{p}\psi = e^{i\mathbf{k}\cdot\mathbf{r}}(\hbar\mathbf{k} - i\hbar\nabla)u$. Define

$$H_{\mathbf{k}} = e^{-i\mathbf{k}\cdot\mathbf{r}} H e^{i\mathbf{k}\cdot\mathbf{r}} = \frac{(\mathbf{p}+\hbar\mathbf{k})^2}{2m} + U. \tag{2.6}$$

The Hellmann–Feynman theorem gives

$$\frac{\partial E_n}{\partial k_i} = \langle u_n | \partial_{k_i} H_{\mathbf{k}} | u_n \rangle = \hbar\langle v_i \rangle, \qquad (m_n^{-1})_{ij} = \frac{1}{\hbar^2}\frac{\partial^2 E_n}{\partial k_i \partial k_j}. \tag{2.7}$$

The periodic potential is already incorporated in the band. Passing an ion is therefore not another Drude collision. Momentum relaxation instead comes from defects, phonons, and allowed interaction processes. The mass above is a local curvature mass; the cyclotron mass measured by quantum oscillations is an equal-energy-area derivative. They coincide only for particular dispersions.

2.3 Nearly free electrons and Bragg gaps

Away from degeneracy, second-order perturbation theory gives $\delta E_{\mathbf{k}} = \sum_{\mathbf{G}\neq 0} |U_{\mathbf{G}}|^2/(E^0_{\mathbf{k}} - E^0_{\mathbf{k}-\mathbf{G}})$. When a denominator becomes small, diagonalize the nearly degenerate subspace first. Retaining $|\mathbf{k}\rangle$ and $|\mathbf{k}-\mathbf{G}\rangle$ gives

$$H_2 = \begin{pmatrix} E^0_{\mathbf{k}} & U_{\mathbf{G}} \\ U^*_{\mathbf{G}} & E^0_{\mathbf{k}-\mathbf{G}} \end{pmatrix}, \quad E_{\pm} = \frac{E^0_{\mathbf{k}} + E^0_{\mathbf{k}-\mathbf{G}}}{2} \pm \sqrt{\left(\frac{E^0_{\mathbf{k}} - E^0_{\mathbf{k}-\mathbf{G}}}{2}\right)^2 + |U_{\mathbf{G}}|^2}. \tag{2.8}$$

On the Bragg plane the uncoupled energies coincide, producing a gap $2|U_{\mathbf{G}}|$. The phase of $U_{\mathbf{G}}$ determines the standing-wave position relative to the ions, but not this two-state gap.

2.3.1 Example B2 A one-dimensional gap and negative curvature mass

Take $a = 0.4\,\mathrm{nm}$, $U_G = 0.2\,\mathrm{eV}$, $G = 2\pi/a$, and $k = G/2 + q$. With $E_B = \hbar^2 G^2/(8m) = 2.350\,\mathrm{eV}$,

$$E_{\pm}(q) = E_B + \frac{\hbar^2 q^2}{2m} \pm \sqrt{|U_G|^2 + \left(\frac{\hbar^2 G q}{2m}\right)^2}. \tag{2.9}$$

At $q = 0$ the energies are 2.150 and $2.550\,\mathrm{eV}$. Expanding the square root gives

$$\frac{1}{m^*_{\pm}} = \frac{1}{m}\left(1 \pm \frac{2E_B}{|U_G|}\right). \tag{2.10}$$

The lower-band maximum has $m^*_-/m \simeq -0.0444$, while the upper-band minimum has $m^*_+/m \simeq 0.0408$. A negative curvature does not imply a negative bare electron mass; positive-charge holes provide a convenient description near a filled band. The expansion requires $|\hbar^2 G q/(2m)| \ll |U_G|$, with other plane waves well separated. Extrapolating this small band-edge mass across the entire Brillouin zone is unjustified.

2.4 Linear combinations of atomic orbitals and nonorthogonal bases

For localized orbitals $\phi_\alpha(\mathbf{r} - \mathbf{R})$, form Bloch sums $|\phi_{\alpha\mathbf{k}}\rangle = N^{-1/2}\sum_{\mathbf{R}} e^{i\mathbf{k}\cdot\mathbf{R}}|\phi_{\alpha\mathbf{R}}\rangle$. A variational state $|\psi\rangle = \sum_\alpha c_\alpha |\phi_{\alpha\mathbf{k}}\rangle$ satisfies

$$H(\mathbf{k})c = ES(\mathbf{k})c, \quad H_{\alpha\beta} = \langle\phi_{\alpha\mathbf{k}}|H|\phi_{\beta\mathbf{k}}\rangle, \quad S_{\alpha\beta} = \langle\phi_{\alpha\mathbf{k}}|\phi_{\beta\mathbf{k}}\rangle. \tag{2.11}$$

Normalization means $c^\dagger S c = 1$. If S is positive definite, $\widetilde{H} = S^{-1/2} H S^{-1/2}$ is an ordinary Hermitian eigenproblem. Near-zero eigenvalues of S usually signal a nearly linearly dependent basis. Resolve that problem before interpreting divergent energies as physical bands. Slater–Koster parametrization organizes orbital matrix elements using bond directions and a small set of two-center integrals[1].

2.4.1 Example B3 A nonorthogonal one-dimensional chain

With nearest-neighbor hopping $-t$ and overlap s,

$$H(k) = \epsilon_0 - 2t\cos ka, \quad S(k) = 1 + 2s\cos ka, \quad E(k) = \frac{\epsilon_0 - 2t\cos ka}{1 + 2s\cos ka}. \tag{2.12}$$

For $\epsilon_0 = 0$, $t = 1\,\mathrm{eV}$, and $s = 0.1$, one obtains $E(0) = -1.6667\,\mathrm{eV}$, $E(\pi/2a) = 0$, and $E(\pi/a) = 2.5\,\mathrm{eV}$. Dropping overlap gives the symmetric interval $[-2, 2]\,\mathrm{eV}$, altering both bandwidth and electron–hole asymmetry. Positive definiteness requires $|s| < 1/2$. Expansion around the band bottom gives $\hbar^2/(2m^*) = ta^2/(1 + 2s)^2$, so overlap also changes the transport mass. Check energies, S-normalization, and velocity together rather than comparing bandwidth alone.

2.5 Wannier functions and second quantization

For an isolated collection of Bloch bands, define

$$|w_{\alpha\mathbf{R}}\rangle = \frac{1}{\sqrt{N}}\sum_{\mathbf{k}n} e^{-i\mathbf{k}\cdot\mathbf{R}}|\psi_{n\mathbf{k}}\rangle U_{n\alpha}(\mathbf{k}). \tag{2.13}$$

The matrix $U(\mathbf{k})$ is unitary within the selected subspace. Gauge changes alter Wannier shapes without changing its spectrum. Orthogonal Bloch states and unitarity imply $\langle w_{\alpha\mathbf{R}}|w_{\beta\mathbf{R}'}\rangle = \delta_{\alpha\beta}\delta_{\mathbf{R}\mathbf{R}'}$. Orthogonality

does not guarantee exponential localization: a two-dimensional occupied subspace with nonzero Chern number cannot have a globally smooth periodic gauge yielding exponentially localized orthonormal Wannier functions. This is a topological obstruction, not insufficient numerical convergence.

Expand the field operator in the orthonormal basis, $\hat{\psi}(\mathbf{r}) = \sum_{\mathbf{R}\alpha} w_{\alpha\mathbf{R}}(\mathbf{r}) c_{\mathbf{R}\alpha}$. The one-particle Hamiltonian becomes

$$\hat{H} = \sum_{\mathbf{R}\mathbf{R}'\alpha\beta} t_{\alpha\beta}(\mathbf{R}-\mathbf{R}') c^{\dagger}_{\mathbf{R}\alpha} c_{\mathbf{R}'\beta}, \tag{2.14}$$

$$c_{\mathbf{R}\alpha} = \frac{1}{\sqrt{N}} \sum_{\mathbf{k}} e^{i\mathbf{k}\cdot\mathbf{R}} c_{\mathbf{k}\alpha}, \qquad \hat{H} = \sum_{\mathbf{k}} c^{\dagger}_{\mathbf{k}} H(\mathbf{k}) c_{\mathbf{k}}. \tag{2.15}$$

Either count each undirected bond once and add its Hermitian conjugate, or sum both directed bonds. Mixing the conventions doubles the hopping. Also specify whether orbital positions enter the Fourier phase. This affects matrix periodicity and Berry-connection expressions, but not physical predictions when treated consistently.

2.6 Square-lattice bands and density of states

The nearest-neighbor tight-binding Hamiltonian of the square lattice is $H = -t \sum_{\langle ij\rangle\sigma} (c^{\dagger}_i c_j + \text{h.c.})$. Forward and backward hopping along each lattice axis give

$$\epsilon(\mathbf{k}) = -2t(\cos k_x a + \cos k_y a). \tag{2.16}$$

The energies at Γ, $X = (\pi/a, 0)$, and $M = (\pi/a, \pi/a)$ are $-4t$, 0, and $4t$, respectively. The bandwidth is $8t$. Near the minimum, $\epsilon \simeq -4t + ta^2k^2$, so $m^* = \hbar^2/(2ta^2)$. Taking $t = 1\,\text{eV}$ and $a = 0.4\,\text{nm}$ gives $m^* = 0.2381 m_e$.

2.6.1 Example B4 Fermi surface nesting and the van Hove peak

At spin-degenerate half filling there is one electron per cell, $n_c = 1$, and $\mu = 0$. The Fermi contour $\cos k_x a + \cos k_y a = 0$ is a diamond connecting the four X points. Its enclosed area is half the Brillouin zone; multiplying by two spins gives one electron per cell. The vector $\mathbf{Q} = (\pi/a, \pi/a)$ satisfies $\epsilon(\mathbf{k}+\mathbf{Q}) = -\epsilon(\mathbf{k})$. This nesting is relevant to antiferromagnetic Hubbard mean field, but nesting alone does not establish magnetic order.

Near X, write $k_x = \pi/a + q_x$ and $k_y = q_y$, obtaining $\epsilon \simeq ta^2(q_y^2 - q_x^2)$. Hyperbolic constant-energy contours produce a logarithmic density-of-states singularity. Per cell and per spin,

$$D(E) = \frac{1}{2\pi^2 t} K\left(1 - \frac{E^2}{16t^2}\right), \qquad |E| < 4t, \tag{2.17}$$

where $K(m) = \int_0^{\pi/2} (1 - m\sin^2\theta)^{-1/2} d\theta$ uses the parameter m, not the modulus. Near zero energy, $D(E) \simeq (2\pi^2 t)^{-1} \ln(16t/|E|)$. The normalization is $\int D(E) dE = 1$; it becomes 2 only after including spin.

A direct numerical calculation on an $N_k \times N_k$ grid uses

$$D_\eta(E) = \frac{1}{N_k^2} \sum_{\mathbf{k}} \frac{\eta/\pi}{(E - \epsilon_{\mathbf{k}})^2 + \eta^2}. \tag{2.18}$$

Compare $N_k = 100, 200, 400$ and $\eta/t = 0.1, 0.05, 0.025$. If broadening is smaller than the discrete level spacing, the DOS acquires grid artifacts. Converge the grid before reducing broadening. Lorentzian tails extend beyond the nominal band, so integrating over a finite window can give less than one without indicating a programming error. Adding $-4t' \cos k_x a \cos k_y a$ moves the saddle energy to $4t'$ and destroys perfect nesting, an important step toward more realistic band structures.

2.7 Band-theory exercises and solution notes

1. Halve U_G in B2. The gap halves, the absolute band-edge masses decrease, and the range of q for which the expansion is valid also narrows. Explain all three changes.
2. Shift the energy origin in B3 using $H \to H + \Delta S$. Every eigenvalue must increase by Δ. The incorrect replacement $H \to H + \Delta I$ produces an artificial momentum-dependent shift in a nonorthogonal basis.
3. For B4 verify the integrated number of states, the half-filled electron count, and the band-bottom mass. All three should be correct before reusing the grid for magnetism or transport.

2.8 Graphene and low-dimensional bands

The two sublattices of graphene produce a Dirac low-energy dispersion, while boundaries and relative layer rotation introduce edge states and moiré bands. Minimal models resolve the main features of these structures. Quantitative descriptions of particular samples also require longer-range hopping, interactions, edge reconstruction, and lattice relaxation. The parameters below specify the energy and length scales of each model.

2.8.1 Two sublattices of the honeycomb structure

Choose nearest-neighbor vectors $\boldsymbol{\delta}_1 = a_0(1, 0)$ and $\boldsymbol{\delta}_{2,3} = a_0(-1/2, \pm\sqrt{3}/2)$. In the A, B basis,

$$H(\mathbf{k}) = -t \begin{pmatrix} 0 & f(\mathbf{k}) \\ f^*(\mathbf{k}) & 0 \end{pmatrix}, \quad f = e^{ik_x a_0} + 2e^{-ik_x a_0/2} \cos \frac{\sqrt{3} k_y a_0}{2}. \tag{2.19}$$

Solving the characteristic equation gives

$$E_\pm = \pm t \sqrt{1 + 4 \cos \frac{3k_x a_0}{2} \cos \frac{\sqrt{3} k_y a_0}{2} + 4 \cos^2 \frac{\sqrt{3} k_y a_0}{2}}. \tag{2.20}$$

Zero energy lies at the half-filled Dirac points. Energies at Γ are $\pm 3t$ and those at the saddle points are $\pm t$. Two inequivalent valleys can be chosen as $\mathbf{K}_\tau = (0, \tau 4\pi/(3\sqrt{3}a_0))$. A different sublattice Fourier convention can multiply f by a unit-modulus phase; compare eigenvalues and basis definitions before comparing matrix entries.

Expand at $\mathbf{k} = \mathbf{K}_\tau + \mathbf{q}$. After a fixed basis change the result can be written

$$H_\tau(\mathbf{q}) = \hbar v_F (\tau q_x \sigma_x + q_y \sigma_y), \qquad v_F = \frac{3ta_0}{2\hbar}. \tag{2.21}$$

The displayed local coordinates are rotated relative to those used above. The Pauli matrices act on sublattice pseudospin, not the physical electron spin. The linear dispersion results from destructive interference between orbital amplitudes; it does not turn crystal electrons into free particles propagating in relativistic vacuum.

Example B5 Fermi energy from a gate-controlled density

A circular two-dimensional Fermi surface contains $k_F^2/(4\pi)$ states per area for each spin and valley. With $g_s g_v = 4$,

$$n = \frac{k_F^2}{\pi}, \qquad E_F = \hbar v_F \sqrt{\pi |n|}\,\mathrm{sgn}\, n, \qquad D(E) = \frac{2|E|}{\pi(\hbar v_F)^2}. \tag{2.22}$$

For $t = 2.7\,\mathrm{eV}$ and $a_0 = 0.142\,\mathrm{nm}$, $v_F = 8.737 \times 10^5\,\mathrm{m/s}$. At $n = 10^{12}\,\mathrm{cm}^{-2}$, $k_F = 1.772 \times 10^8\,\mathrm{m}^{-1}$ and $E_F = 0.1019\,\mathrm{eV}$. The cyclotron mass is $m_c = (\hbar^2/2\pi)\partial A/\partial E = |E_F|/v_F^2 = 0.0235 m_e$. A linear band thus has a nonzero cyclotron mass at nonzero density. Choosing the commonly used $v_F = 10^6\,\mathrm{m/s}$ instead gives $E_F = 0.1167\,\mathrm{eV}$; the difference is a parameter choice, not an inconsistency in the formula.

2.8.2 Pseudospin and Klein transmission

A positive-energy eigenvector can be chosen as $|u_+\rangle = (1, e^{i\theta})^T/\sqrt{2}$. Its pseudospin rotates with momentum. Smooth scalar potentials weakly mix valleys, and their scattering probability contains

$$|\langle u_+(\theta')|u_+(\theta)\rangle|^2 = \frac{1 + \cos(\theta' - \theta)}{2}. \tag{2.23}$$

Exact backscattering is suppressed in this model. Atomic-scale defects, sublattice mass terms, magnetic scattering, and intervalley mixing can invalidate the result.

Example B6 A barrier at normal incidence

For $H = -i\hbar v_F \sigma_x \partial_x + V(x)$ at $k_y = 0$, $[H, \sigma_x] = 0$. Pseudospin is conserved in the right-moving channel, whose wavefunction only accumulates phase:

$$\psi_+(x) = \chi_+ \exp\left[\frac{i}{\hbar v_F}\int^x (E - V(x'))dx'\right], \quad \sigma_x \chi_+ = \chi_+. \tag{2.24}$$

With identical leads and a valley-preserving barrier, a reflected state would have the wrong pseudospin, so $T(0) = 1$. This includes a barrier whose interior lies in the valence band. For $E = 0.10\,\mathrm{eV}$, $V_0 = 0.20\,\mathrm{eV}$, and width $50\,\mathrm{nm}$, changing width changes the propagation phase while normal-incidence transmission remains one. Oblique incidence generally permits reflection. The result does not imply dissipationless transport for all graphene carriers. It connects eigenvector structure directly to the angular weighting of transport scattering.

2.8.3 Boundary spectra of nanoribbons

For a ribbon, Fourier transform only along the translation-invariant edge and retain a finite number of transverse chains. Diagonalize the finite Hermitian matrix at each $k_\parallel$, then inspect eigenvector weights to distinguish bulk and edge states. An in-gap eigenvalue without spatial information is insufficient evidence for an edge state.

Example B7 A recursion relation for zigzag edge states

In a massless, nearest-neighbor, semi-infinite zigzag ribbon, a zero-energy solution can occupy one sublattice only. Let A_j denote its amplitude on transverse chain j, and let $a_\parallel = \sqrt{3}a_0$ be the edge period. The zero-energy equation is

$$A_{j+1} = -2\cos(k_\parallel a_\parallel/2) A_j \equiv r(k_\parallel) A_j. \tag{2.25}$$

Normalizability requires $|r| < 1$. For $k_\parallel a_\parallel \in [0, 2\pi]$, the allowed interval is $2\pi/3 < k_\parallel a_\parallel < 4\pi/3$. A normalized state is $A_j = \sqrt{1-r^2}\, r^{j-1}$, with localization length $\xi = -1/\ln|r|$ in units of transverse chain spacing. At $k_\parallel a_\parallel = \pi$, $r = 0$ and the state resides on the outermost chain. Approaching a projected valley gives $|r| \to 1$: the localization length diverges and the edge solution merges into the bulk.

Two edges hybridize in a finite-width ribbon, producing an exponentially small splitting. The ideal flat band is not universal for physical edges. Armchair boundaries mix valleys, lack the same flat-band interval, and have width-family-dependent gaps. Passivation, reconstruction, and further-neighbor hopping alter the spectrum. Enhanced edge DOS favors interaction instabilities, but magnetic order requires a self-consistent Hubbard calculation and a finite-temperature assessment. A noninteracting flat band is not itself proof of ferromagnetism.

2.8.4 One-dimensional topology of the SSH chain

An SSH cell contains sites A, B, intracell hopping t_1, and intercell hopping t_2. For a specified cell boundary,

$$H(k) = \begin{pmatrix} 0 & t_1 + t_2 e^{-ika} \\ t_1 + t_2 e^{ika} & 0 \end{pmatrix} = (t_1 + t_2 \cos ka)\sigma_x + t_2 \sin ka\, \sigma_y. \tag{2.26}$$

Chiral symmetry is $\sigma_z H \sigma_z = -H$. The energies are $E_\pm = \pm\sqrt{t_1^2 + t_2^2 + 2t_1 t_2 \cos ka}$, and the bulk gap $2|t_1 - t_2|$ closes at $t_1 = t_2$.

Example B8 Winding number edge states and finite size

The complex function $q(k) = t_1 + t_2 e^{ika}$ traces a circle of radius $|t_2|$ centered at t_1. For positive hoppings,

$$w = \frac{1}{2\pi}\int_{-\pi/a}^{\pi/a} \partial_k \arg q(k)\, dk = \begin{cases} 1 & t_2 > t_1, \\ 0 & t_2 < t_1. \end{cases} \tag{2.27}$$

Choose the lower-band state $|u_-\rangle = (-e^{-i\arg q}, 1)^T/\sqrt{2}$. Then $A_k = i\langle u_-|\partial_k u_-\rangle = \frac{1}{2}\partial_k \arg q$, giving Zak phase $\gamma = \pi w \pmod{2\pi}$. For an open chain beginning with an A site, the zero-energy recursion is $A_{j+1} = -(t_1/t_2)A_j$. With $t_1 = 0.6$, $t_2 = 1$, and 40 cells, the bulk gap is 0.8, the probability ratio is $|A_{j+1}|^2/|A_j|^2 = 0.36$, and $\xi/a = 1.958$. Hybridization between opposite ends is exponentially small. Reversing the parameters to $t_1 = 1$, $t_2 = 0.6$ removes this pair of edge states for the same termination.

A change of cell convention can change the integer representation of w, so the termination must also be reported. Observable statements compare bulk polarization with a fixed physical termination. Adding $\Delta\sigma_z$ breaks chiral symmetry: edge levels need not stay at zero and the Zak phase is generally not quantized. Preserving a gap alone does not preserve every protecting symmetry. The SSH and Majorana chains have related mechanisms of boundary localization, but an SSH edge state is an ordinary complex-fermion state, not a Majorana zero mode.

2.8.5 Moiré bands and estimates of competing scales

Two rotated lattices generate the long wavelength

$$L_M = \frac{a}{2\sin(\theta/2)}, \quad k_\theta = 2K\sin(\theta/2), \quad \alpha = \frac{w}{\hbar v_F k_\theta}. \tag{2.28}$$

Here $a = \sqrt{3}a_0$ is graphene's lattice constant and w is interlayer tunneling. A continuum model couples the two layer Dirac Hamiltonians through three dominant momentum-transfer components and diagonalizes a

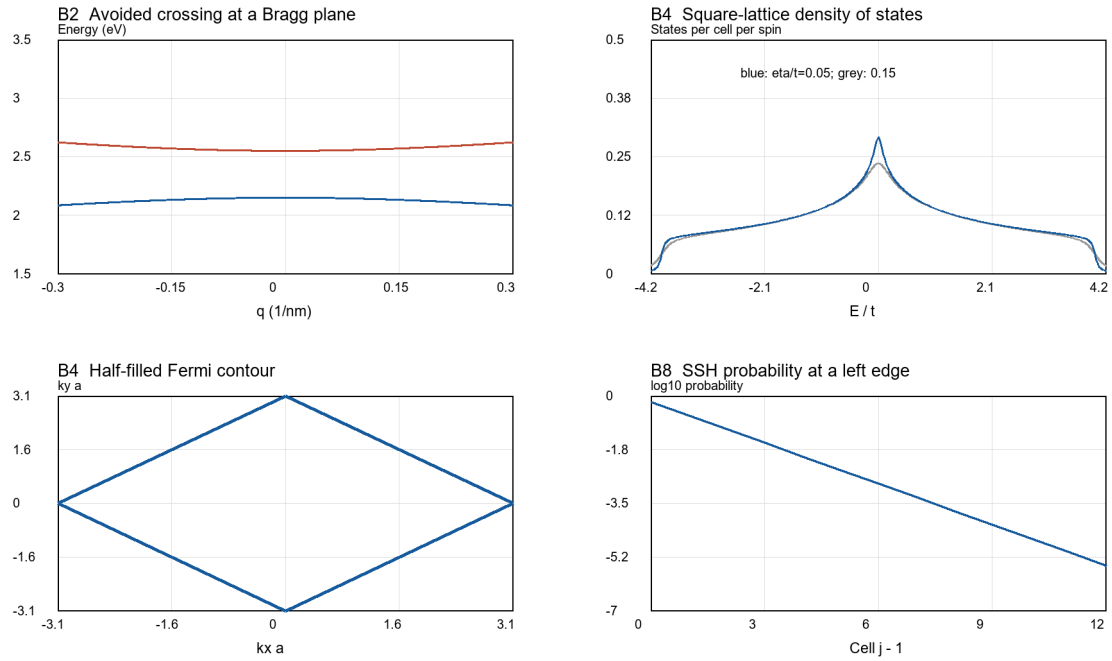

Figure 2.1: Numerical band and boundary-state results. Top left: the avoided crossing of B2. Top right: the square-lattice DOS in B4 with two Lorentzian broadenings. Bottom left: the half-filled Fermi contour. Bottom right: the semi-infinite SSH left-edge probability in B8. All panels use the stated model parameters.

truncated moiré reciprocal-space matrix[8]. The ratio α compares tunneling and single-layer kinetic energy. It explains stronger hybridization at small angles but cannot replace a full band calculation.

Example B9 Filling density of a moiré cell

For $a = 0.246\,\text{nm}$ and $\theta = 1.1°$, $L_M = 12.81\,\text{nm}$ and $A_M = \sqrt{3}L_M^2/2 = 142.2\,\text{nm}^2$. A narrow band with two spins and two valleys contains $n_s = 4/A_M = 2.81 \times 10^{12}\,\text{cm}^{-2}$ states per area. The variable $\nu = nA_M$ therefore converts gate density into carriers per moiré cell.

For $w = 110\,\text{meV}$ and $v_F = 10^6\,\text{m/s}, \hbar v_F k_\theta \simeq 215\,\text{meV}$ and $\alpha \simeq 0.51$. This is not a precise magic-angle prediction: relaxation, unequal AA/AB tunneling, and remote bands matter. If bandwidth W decreases more rapidly than the Coulomb scale $E_C \sim e^2/(4\pi\epsilon_0\epsilon_r L_M)$, the ratio E_C/W increases and a one-electron description becomes less reliable. For $\epsilon_r = 10$, $E_C \simeq 11.2\,\text{meV}$. Correlated insulators and superconductivity require additional many-body evidence; flatness does not select a unique pairing mechanism.

2.8.6 Low-dimensional-band exercises and solution notes

1. Compute the honeycomb DOS and check its low-energy linearity, saddles at $\pm t$, and integrated count of two states per cell per spin.

2. Add second-neighbor hopping to a zigzag ribbon and plot energies with edge weights. Breaking chiral symmetry generally makes the edge band dispersive and releases zero-energy pinning.

3. Compare periodic and open SSH spectra and add weak random bonds. Chiral-preserving bond disorder differs from random onsite disorder; compare identical terminations.

Chapter 3

Topological band theory and applications

Topological band theory describes properties of occupied-state geometry that cannot be determined from the local energy dispersion alone. Landau levels and the quantum Hall effect connect the Chern number to quantized conductance; time reversal and crystal symmetries permit further topological classes. Relations between invariants, boundary spectra, and transport require appropriate gap and symmetry conditions. Hall signs use $j_x = \sigma_{xy} E_y$ and $A_i = i\langle u|\partial_i u\rangle$. The opposite tensor component σ_{yx} has the opposite sign.

3.1 Landau levels and state counting

For a two-dimensional electron of charge $-e$, SI units give $H = (\mathbf{p}+e\mathbf{A})^2/(2m)$. Choose $\mathbf{A} = (-By, 0, 0)$, so that $p_x = \hbar k_x$ is conserved:

$$H_{k_x} = \frac{p_y^2}{2m} + \frac{1}{2} m\omega_c^2 (y - y_0)^2, \quad \omega_c = \frac{e|B|}{m}, \quad y_0 = \frac{\hbar k_x}{eB}, \quad \ell_B = \sqrt{\frac{\hbar}{e|B|}}. \tag{3.1}$$

The energies are $E_n = \hbar\omega_c(n+1/2)$. With $\Delta k_x = 2\pi/L_x$, restricting the guiding centers to the sample gives $N_\phi = A/(2\pi\ell_B^2) = e|B|A/h$ states per spin branch. Resolved quantization requires level spacing larger than temperature and broadening; $\omega_c\tau > 1$ alone does not summarize every experimental requirement.

3.1.1 Example B10 Landau scales in GaAs and graphene

For $m^* = 0.067 m_e$ and $B = 5\,\mathrm{T}$, $\hbar\omega_c = 8.64\,\mathrm{meV}$, $\ell_B = 11.47\,\mathrm{nm}$, and the degeneracy per spin is $n_B = 1.209 \times 10^{11}\,\mathrm{cm}^{-2}$. A total density $3.0 \times 10^{11}\,\mathrm{cm}^{-2}$ gives filling $n/n_B = 2.48$; actual plateaus also depend on spin splitting and localization. For graphene, ladder operators constructed from covariant momenta yield

$$E_n = \mathrm{sgn}(n) v_F \sqrt{2e\hbar|B||n|}, \qquad n = 0, \pm 1, \ldots. \tag{3.2}$$

With $v_F = 10^6\,\mathrm{m/s}$ at $5\,\mathrm{T}$, $E_1 = 81.1\,\mathrm{meV}$, and a zero-energy $n = 0$ level exists. Linear-B versus square-root-B spacing is a useful experimental signature of the underlying dispersion.

3.2 From Kubo sums to Berry curvature

Differentiate the eigenvalue equation and project onto another band:

$$\langle u_m|\partial_i u_n\rangle = \frac{\langle u_m|\partial_i H|u_n\rangle}{E_n - E_m}, \qquad m \neq n. \tag{3.3}$$

Substitution into $\Omega_{n,xy} = i(\langle\partial_x u_n|\partial_y u_n\rangle - \langle\partial_y u_n|\partial_x u_n\rangle)$ gives

$$\Omega_{n,xy} = -2\,\mathrm{Im} \sum_{m\neq n} \frac{\langle u_n|\partial_x H|u_m\rangle\langle u_m|\partial_y H|u_n\rangle}{(E_n - E_m)^2}. \tag{3.4}$$

Interband velocity matrix elements in the Kubo response become band geometry. For a two-dimensional band insulator,

$$C = \frac{1}{2\pi} \sum_{n \in \mathrm{occ}} \int_{\mathrm{BZ}} \Omega_{n,xy}\, d^2k, \qquad \sigma_{xy} = -\frac{e^2}{h} C. \tag{3.5}$$

Integrality follows from gauge patching on the Brillouin torus, not from a pointwise integer curvature. A metal integrates only occupied portions of bands and is generally not quantized. In disordered Hall plateaus a mobility gap and real-space topology are the appropriate concepts; a completely empty spectral interval is not essential.

The gauge transformation $|u\rangle \to e^{i\chi}|u\rangle$ changes A_i to $A_i - \partial_i \chi$ while leaving curvature invariant. Numerical eigenvectors have independent arbitrary phases at neighboring momenta. Direct finite differences of their components are therefore unreliable unless a gauge is controlled. Matrix-element expressions or gauge-invariant overlap loops avoid this problem.

3.3 Analytic geometry of a two-band Hamiltonian

For $H = d_0 I + \mathbf{d} \cdot \boldsymbol{\sigma}$, the energies are $E_s = d_0 + sd$, with $s = \pm 1$, and projectors are $P_s = (I + s\hat{\mathbf{d}} \cdot \boldsymbol{\sigma})/2$. Using $\sigma_i \sigma_j = \delta_{ij} + i\epsilon_{ijk}\sigma_k$ yields

$$\Omega_{s,xy} = -\frac{s}{2} \hat{\mathbf{d}} \cdot (\partial_x \hat{\mathbf{d}} \times \partial_y \hat{\mathbf{d}}), \qquad g_{ij} = \frac{1}{4} \partial_i \hat{\mathbf{d}} \cdot \partial_j \hat{\mathbf{d}}. \tag{3.6}$$

The scalar d_0 changes energies without changing eigenvectors or geometry. It can nevertheless create indirect band overlap, so an unchanged Chern-band structure need not remain insulating.

3.3.1 Example B11 Massive Dirac valleys and the limit of half integers

Take $H_\tau = \hbar v(\tau q_x \sigma_x + q_y \sigma_y) + m_\tau \sigma_z$. The lower-band curvature is

$$\Omega_{-,\tau}(\mathbf{q}) = \frac{\tau m_\tau (\hbar v)^2}{2[(\hbar v q)^2 + m_\tau^2]^{3/2}}. \tag{3.7}$$

Integration over the continuum plane gives $C_\tau = \tau\, \mathrm{sgn}(m_\tau)/2$. This single-valley half integer is not a valid total Chern number for an isolated two-dimensional lattice band. The other valley and ultraviolet regularization complete the integer. Equal masses at the valleys cancel their contributions, though valley-resolved transverse responses can remain. Opposite masses make them add. With $\hbar v = 0.6582\,\mathrm{eV\,nm}$ and $m = 0.05\,\mathrm{eV}$, the valley-center curvature magnitude is $86.64\,\mathrm{nm}^2$. Smaller gaps produce taller, narrower curvature peaks and require finer numerical meshes.

3.4 Masses and phase boundaries of the Haldane model

Add sublattice onsite energies $\pm M$ and directed second-neighbor hoppings $t_2 e^{\pm i\phi}$ to the honeycomb model. The flux per unit cell vanishes, so translation symmetry can survive. Choose valley and bond-orientation conventions such that

$$m_\tau = M - \tau 3\sqrt{3} t_2 \sin\phi, \qquad C_- = \frac{1}{2}[\mathrm{sgn}(m_+) - \mathrm{sgn}(m_-)]. \tag{3.8}$$

Opposite masses occur for $|M| < 3\sqrt{3}|t_2 \sin\phi|$, giving $|C| = 1$. At a phase boundary one valley closes its gap, allowing the invariant to change[2]. The $t_2 \cos\phi$ term contributes $d_0(\mathbf{k})$, so the global indirect gap must also be checked before calling the state an insulator.

3.4.1 Example B12 Predicting a QAH phase from mass signs

Set $t_1 = 1$, $t_2 = 0.1$, and $\phi = \pi/2$. The critical mass is $M_c = 0.519615$. At $M = 0.2$, $m_+ = -0.319615$ and $m_- = 0.719615$, giving $C = -1$ for the lower band and $\sigma_{xy} = +e^2/h$ in our convention. The direct gaps at the two valleys are 0.63923 and 1.43923; scan the full Brillouin zone to verify the global gap. At $M = 0.8$, both masses are positive and $C = 0$.

Both parameter sets are gapped, but their mass patterns differ. Opening a gap alone therefore does not diagnose topology. The 2013 observation of QAH in a magnetic topological insulator[9] is a material realization, not an assertion that the material implements every term of the minimal honeycomb model. The QAH mechanism in magnetically doped InAs/GaSb likewise depends on its effective bands and exchange field, without a term-by-term identification with the honeycomb model.

3.5 The QWZ model and a discrete Chern number

A two-band model on the square lattice is

$$H(\mathbf{k}) = \sin k_x \sigma_x + \sin k_y \sigma_y + (m + \cos k_x + \cos k_y)\sigma_z, \tag{3.9}$$

with lattice and energy units set to one. This is a convention for a standard two-orbital Chern model[7]. The possible gap closures are at Γ, X, Y, M, with masses $m + 2, m, m, m - 2$ and Dirac chiralities $+, -, -, +$. Thus

$$C_- = \frac{1}{2}[\mathrm{sgn}(m + 2) - 2\,\mathrm{sgn}(m) + \mathrm{sgn}(m - 2)]. \tag{3.10}$$

The result is zero for $|m| > 2$, $+1$ for $-2 < m < 0$, and -1 for $0 < m < 2$. At $m = -2, 0, 2$, the occupied subspace is not smooth and an insulating-band Chern number is undefined.

3.5.1 Example B13 A Chern calculation without gauge fixing

On a periodic mesh $k_i = -\pi + 2\pi i/N$, obtain lower-band eigenvectors u_{ij}. To match $A = i\langle u|\nabla u\rangle$, use *reverse overlaps*:

$$U_x(i, j) = \frac{\langle u_{i+1,j}|u_{i,j}\rangle}{|\langle u_{i+1,j}|u_{i,j}\rangle|}, \quad U_y(i, j) = \frac{\langle u_{i,j+1}|u_{i,j}\rangle}{|\langle u_{i,j+1}|u_{i,j}\rangle|}. \tag{3.11}$$

The plaquette flux and Chern number are

$$F_{ij} = \mathrm{Arg}[U_x(i, j)U_y(i + 1, j)U_x(i, j + 1)^* U_y(i, j)^*], \quad C_N = \frac{1}{2\pi}\sum_{ij} F_{ij}. \tag{3.12}$$

Indices are periodic modulo N, and the principal argument lies in $(-\pi, \pi]$. This is an equivalent sign convention for the Fukui–Hatsugai–Suzuki lattice method[3]. With forward overlaps, reverse the sign of the summed flux. The parameters $m = -1, 1, 3$ must yield $C = 1, -1, 0$. First verify signs against the analytic phase diagram, then multiply every eigenvector by an independent random phase to test gauge invariance, and finally compare $N = 21, 41, 81$.

An integer answer is not sufficient validation: a coarse mesh can give the wrong integer. Also inspect the minimum energy gap, minimum neighboring overlap, and maximum plaquette flux relative to the branch cut $\pm\pi$. For multiple occupied bands, use the normalized determinant of the occupied-subspace overlap matrix. Do not follow an arbitrary single band through an occupied-band degeneracy.

3.6 Boundary spectra and the meaning of conductance

For a QWZ strip open along x and periodic along y, the onsite matrix is $h_0(k_y) = \sin k_y \sigma_y + (m + \cos k_y)\sigma_z$. Neighboring layers couple through

$$T_x = \frac{\sigma_z - i\sigma_x}{2}, \qquad H = \sum_j c_j^\dagger h_0 c_j + \sum_j (c_j^\dagger T_x c_{j+1} + \text{h.c.}). \tag{3.13}$$

At each k_y diagonalize a $2N_x$ matrix and color eigenvalues by their probability on the leftmost and rightmost layers. In a topological phase, edge bands cross the bulk gap. Opposite edges propagate oppositely; the net chirality on a given edge is fixed by C.

An ideal chiral channel carries the Landauer current

$$I = \frac{e}{h} \int dE\, [f_L(E) - f_R(E)], \qquad G = \frac{e^2}{h} = 38.74\,\mu\text{S}. \tag{3.14}$$

This conductance is defined with contacts. Topological protection suppresses specified elastic backscattering processes; it does not make every part of a sample, lead, and contact dissipationless at arbitrary temperature. QAH applications require control of bulk carriers, magnetic domains, Fermi energy, and temperature, none of which is guaranteed by an integer alone.

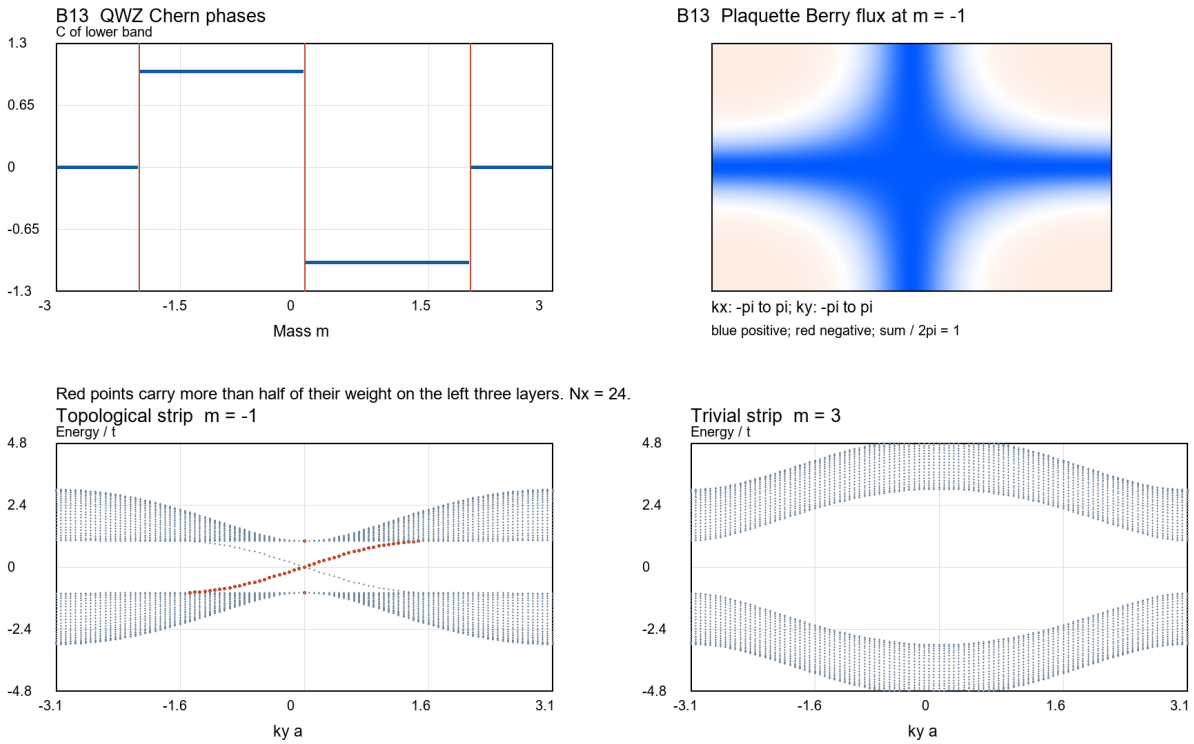

Figure 3.1: B13 and its strip check. Top: the QWZ phase diagram and discrete Berry flux at $m = -1$. Bottom: topological and trivial spectra for 24 layers. Red points carry more than half their weight in the leftmost three layers. Bulk Chern number, boundary dispersion, and localization provide complementary checks.

3.7 Chern-band exercises

1. Exchange the traversal directions k_x, k_y in B13 and explain the Chern sign change. Coordinate axes and Hall-tensor conventions must be exchanged consistently, not just plot labels.
2. Add $0.2(\cos k_x + \cos k_y)I$ to QWZ. Eigenvectors and Chern number remain unchanged, but dispersions, indirect gaps, and occupations at a fixed chemical potential can change.
3. Add weak random onsite disorder to a strip and compare localization and transmission. The absence of a visible momentum-space crossing is not a valid diagnostic after translation symmetry has been lost.

3.8 Topology protected by time reversal and crystal symmetries

The Kane–Mele and BHZ models describe two-dimensional topological insulators protected by time reversal. Three-dimensional systems admit strong and weak indices, while crystal symmetries permit mirror and higher-order topology. Classification depends on dimension, filling, bulk gap, and preserved symmetries. These conditions jointly determine the existence and stability of boundary states.

3.8.1 The tenfold symmetry classification

For a gapped noninteracting or mean-field Hamiltonian, check three spectral symmetries: time reversal $\Theta H(\mathbf{k})\Theta^{-1} = H(-\mathbf{k})$, particle–hole symmetry $\Xi H(\mathbf{k})\Xi^{-1} = -H(-\mathbf{k})$, and unitary chiral symmetry $\Pi H(\mathbf{k})\Pi^{-1} = -H(\mathbf{k})$. The first two are antiunitary and can square to $+1$ or -1. Spectral chiral symmetry is not the same as structural crystal chirality. These conditions organize the tenfold classification[13].

Class	Θ^2	Ξ^2	Π	Selected dimension	Example
A	0	0	0	$d = 2 : \mathbb{Z}$	Chern insulator
AIII	0	0	1	$d = 1 : \mathbb{Z}$	Chiral chain
AII	-1	0	0	$d = 2, 3 : \mathbb{Z}_2$	QSH and strong TI
D	0	$+1$	0	$d = 1 : \mathbb{Z}_2$	Majorana chain
DIII	-1	$+1$	1	$d = 3 : \mathbb{Z}$	TR-invariant superconductor

Here 0 means that a symmetry is not imposed, not that an operator literally squares to zero. The table lists five representative classes of stable noninteracting strong topology. Real-hopping SSH also has additional BDI symmetries; imposing only chiral protection permits its AIII description. Crystal symmetries, fragile topology at a fixed small band count, and interactions can extend or modify the classification. BdG particle–hole constraints arise from the Nambu representation and are not synonymous with approximate electron–hole symmetry of a normal metal. Verify the Hamiltonian's conditions before consulting a table.

3.8.2 Kramers pairs and the quantum spin Hall state

For physical spin one half, $\Theta = is_yK$ and $\Theta^2 = -1$. A time-reversal-invariant momentum satisfies $\mathbf{\Lambda} = -\mathbf{\Lambda} + \mathbf{G}$. At such a point, $|u\rangle$ and $\Theta|u\rangle$ are orthogonal and degenerate. Time reversal makes the total Berry curvature odd in momentum, enforcing zero total two-dimensional Chern number without requiring an atomic-limit occupied subspace.

If s_z is conserved, Kane–Mele can be viewed as two time-reversed Haldane blocks[4]. With $C_\uparrow = 1$ and $C_\downarrow = -1$, charge Hall conductance cancels but $\nu = C_\uparrow \bmod 2 = 1$. A time-reversal-preserving Rashba coupling breaks s_z conservation, so separate spin Chern numbers generally lose this simple interpretation. The $\mathbb{Z}_2$ invariant survives if the bulk gap remains open. Strictly quantized spin Hall conductance is not then a universal statement: the robust property is an odd number of helical Kramers edge pairs.

A time-reversal-symmetric single-particle elastic potential cannot scatter one state of an isolated Kramers edge pair into its time-reversed partner. Multiple pairs can couple and gap in pairs, leaving an odd/even distinction. Magnetic impurities, inelastic processes, and sufficiently strong interactions require separate analysis. A noninteracting proof should not be extrapolated to every experimental condition.

3.8.3 Band inversion and edges in the BHZ model

Using $E1, H1$ orbitals and two Kramers components, the BHZ Hamiltonian is[5]

$$H(\mathbf{k}) = \begin{pmatrix} h(\mathbf{k}) & 0 \\ 0 & h^*(-\mathbf{k}) \end{pmatrix}, \quad h = (C - Dk^2)I + Ak_x\sigma_x - Ak_y\sigma_y + (M - Bk^2)\sigma_z. \tag{3.15}$$

A has dimensions energy times length, B, D energy times length squared, and M is a band-edge mass. With the Bk^2 continuum regularization, $M/B > 0$ means the mass changes sign between zero and infinite momentum. The criterion $M < 0$ alone has no universal meaning without the sign of B. Time reversal makes the two block Chern numbers opposite.

Example B14 Computing an edge decay length

As illustrative parameters, take $C = D = 0$, $A = 364.5\,\text{meV nm}$, $B = -686\,\text{meV nm}^2$, and $M = -10\,\text{meV}$. In the half-plane $x > 0$ at $k_y = 0$, seek $\psi \propto e^{-\lambda x}\chi$. Substitution gives $(M + B\lambda^2)^2 = A^2\lambda^2$. Two positive roots combine to satisfy a hard wall:

$$\lambda_{1,2} = \frac{A \pm \sqrt{A^2 - 4BM}}{2|B|}, \qquad \psi(x) \propto (e^{-\lambda_1 x} - e^{-\lambda_2 x})\chi. \tag{3.16}$$

Numerically, $\lambda_1 \simeq 0.5023\,\text{nm}^{-1}$ and $\lambda_2 \simeq 0.02902\,\text{nm}^{-1}$, giving lengths about 1.99 and $34.5\,\text{nm}$. The longer length controls hybridization between narrow-strip edges. Projecting the k_y term gives two Kramers branches $E = \pm Ak_y$ and speed $A/\hbar = 5.54 \times 10^5\,\text{m/s}$. Changing M to positive while retaining $B < 0$ eliminates this normalizable combination for the same half-space boundary.

In InAs/GaSb wells, electronlike and holelike subbands can hybridize at finite momentum. A four-band effective model remains useful, but its parameters, structural inversion asymmetry, and self-consistent electrostatics depend on the heterostructure. Exchange fields introduced by magnetic doping modify both the masses and energy offsets of the two blocks. The analytic edge solution above applies to the specified parameters and boundary conditions; it cannot replace an eight-band Kane calculation containing additional subbands and exchange couplings.

3.8.4 Parity tests and Wilson loops

With both inversion P and time reversal, take one parity $\xi_{2m} = \pm 1$ from each occupied Kramers pair at each TRIM. Define

$$\delta_i = \prod_{m=1}^{N_{\text{occ}}/2} \xi_{2m}(\mathbf{\Lambda}_i), \qquad (-1)^\nu = \prod_{i=1}^{4} \delta_i. \tag{3.17}$$

Multiplying both partners would square every parity to one and incorrectly label all systems trivial. The criterion uses symmetry representations of the occupied subspace at TRIM[6].

Example B15 Two-dimensional topology from four parity products

If $\delta_\Gamma = -1$ while $\delta_X = \delta_Y = \delta_M = +1$, the product is -1 and $\nu = 1$. A further inversion of occupied and unoccupied states of opposite parity at M changes δ_M to -1, making the product $+1$. Thus a band inversion by itself is not a complete diagnostic: include every relevant TRIM and every occupied Kramers pair. Exchanging same-parity bands need not change the product.

Without inversion, calculate a Wilson loop of the occupied subspace. Define neighboring overlaps $F_j^{mn} = \langle u_m(k_{j+1}, k_y)|u_n(k_j, k_y)\rangle$. An SVD $F_j = V_j \Sigma_j W_j^\dagger$ supplies the unitary part $\widetilde{F}_j = V_j W_j^\dagger$. The closed product

$$\mathcal{W}(k_y) = \widetilde{F}_{N-1} \cdots \widetilde{F}_1 \widetilde{F}_0 \tag{3.18}$$

has eigenvalues $e^{i\theta_a(k_y)}$, giving hybrid Wannier centers $\theta_a/(2\pi)$ along x. Keep the complete occupied subspace continuously: separate Zak phases of individual bands fail at degeneracies. The parity of Kramers partner switching as k_y runs from 0 to π gives the $\mathbb{Z}_2$ invariant. Numerically track spectral flow with its 2π periodicity rather than judging an unconnected scatter plot.

3.8.5 Strong and weak three-dimensional insulators

There are eight TRIM and four invariants:

$$(-1)^{\nu_0} = \prod_{n_1,n_2,n_3=0,1} \delta_{n_1 n_2 n_3}, \qquad (-1)^{\nu_i} = \prod_{n_i=1} \delta_{n_1 n_2 n_3}. \tag{3.19}$$

$\nu_0 = 1$ defines a strong topological insulator. If $\nu_0 = 0$ but some weak index is nonzero, the phase is weak. Stacked two-dimensional QSH layers *can* form a weak TI; simple weakly coupled stacking does not in general produce a strong TI. Whether interlayer coupling changes the strong index must therefore be determined from the complete three-dimensional occupied subspace.

Example B16 Strong and weak indices from eight parity products

If only $\Gamma = (0,0,0)$ has $\delta = -1$, with all other values positive, the indices are $(\nu_0; \nu_1\nu_2\nu_3) = (1; 000)$. If the only negatives occur at $(0,0,0)$ and $(0,0,\pi)$, the result is $(0; 001)$, consistent with stacking along z. Surface spectra depend on orientation; a weak phase need not exhibit the same stable Dirac structure on every surface.

A minimal strong-TI surface model is $H_s = \hbar v(k_x s_y - k_y s_x)$, displaying spin–momentum locking. A perpendicular magnetic mass $m s_z$ opens a gap, connecting to magnetic topology and QAH. The half-quantized response of one continuum surface must be interpreted with the full three-dimensional sample, other surface, and boundaries. It is not a stand-alone half-integer Hall invariant of an isolated two-dimensional lattice.

3.8.6 Weyl nodes as sources of Berry flux

The minimal Weyl Hamiltonian $H = \sum_i v_i q_i \sigma_i$ has chirality $\chi = \mathrm{sgn}(v_x v_y v_z)$. Integrating lower-band Berry curvature over an enclosing sphere gives Chern number χ. Total chirality vanishes in a lattice Brillouin

zone, so a single isolated Weyl node cannot be a complete lattice model. Breaking inversion or time reversal can split a degeneracy into nodes, but symmetry breaking alone does not guarantee their existence.

Example B17 Decomposing a three-dimensional model into Chern slices

Consider

$$H = \sin k_x \sigma_x + \sin k_y \sigma_y + (2 - \cos k_x - \cos k_y - \cos k_z)\sigma_z. \tag{3.20}$$

The only zeros require $k_x = k_y = 0$ and $\cos k_z = 0$, giving $(0, 0, \pm\pi/2)$. Near these points $d_z \simeq \pm q_z$, hence opposite chirality. At fixed k_z, the four two-dimensional Dirac masses are $-\cos k_z$, $2 - \cos k_z$, $2 - \cos k_z$, and $4 - \cos k_z$. The lower-band slice Chern number is -1 for $|k_z| < \pi/2$ and zero outside. A node marks a jump in the slice invariant.

If the chemical potential lies at the nodes and no other Fermi surfaces occur,

$$\sigma_{xy}^{3D} = -\frac{e^2}{h} \int \frac{dk_z}{2\pi} C(k_z) = \frac{e^2}{2ha}, \tag{3.21}$$

where a restores the lattice constant. At $a = 0.5$ nm this is about $3.87 \times 10^4\,\mathrm{S/m}$. Surface Fermi arcs arise from edges of the nontrivial slices and connect projected nodes. A surface on which the projections coincide need not show an equally clear arc. A tilt $\mathbf{w} \cdot \mathbf{q} I$ leaves eigenvectors unchanged but can overtilt the cone into type II, changing the Fermi surface and transport assumptions.

3.8.7 Mirror topology higher-order phases and real-space methods

On a mirror-invariant plane with spin–orbit coupling, mirror eigenvalues are usually $\pm i$. Compute Chern numbers in the two occupied mirror sectors and define $C_M = (C_{+i} - C_{-i})/2$. Time reversal may enforce zero total Chern while allowing nonzero C_M. Mirror-symmetric surfaces can then protect an even number of Dirac cones; a mirror-breaking surface mass can gap them[10, 14]. An even number of surface cones is therefore not automatically trivial when crystalline symmetries are part of the classification.

Higher-order topology relates gapped edges or surfaces to lower-dimensional corner or hinge states. A calculable four-orbital quadrupole representative is[11]

$$H = (\gamma_x + \lambda_x \cos k_x)\Gamma_4 + \lambda_x \sin k_x \Gamma_3 + (\gamma_y + \lambda_y \cos k_y)\Gamma_2 + \lambda_y \sin k_y \Gamma_1, \tag{3.22}$$

where $\Gamma_{1,2,3} = -\tau_y \otimes \sigma_{1,2,3}$ and $\Gamma_4 = \tau_x \otimes I$ mutually anticommute. Its energies are $\pm E$, each doubly degenerate, with

$$E = \sqrt{\gamma_x^2 + \lambda_x^2 + 2\gamma_x\lambda_x \cos k_x + \gamma_y^2 + \lambda_y^2 + 2\gamma_y\lambda_y \cos k_y}. \tag{3.23}$$

The anticommuting structure and corresponding signed hoppings implement the required flux pattern. This differs from simply adding two independent ordinary SSH chains.

Example B18 Corner localization and protection conditions

Take $\lambda_x = \lambda_y = 1$ and $\gamma_x = \gamma_y = 0.5$ with compatible open boundaries. A corner-state amplitude decreases by $|\gamma_i/\lambda_i| = 0.5$ in each direction, so its probability decreases by a factor $1/4$ per cell. The localization length is $1/\ln 2 = 1.443$ cells. Finite samples have exponentially small hybridization between their four corners. Exact zero-energy pinning requires an additional spectral symmetry. Quantized corner charge also requires specified filling, ionic background, and protecting symmetries. A local corner DOS peak alone does not identify a quadrupole phase.

Boundary mass domain walls give another useful picture. For $H_{\text{edge}} = -iv\sigma_z\partial_s + m(s)\sigma_y$, opposite mass signs on adjacent edges permit one normalizable zero-energy branch, $\psi \propto \exp[-\int^s m(s')ds'/v]\chi_+$ or its opposite-sign counterpart. Rotation or mirror symmetry can require neighboring edge masses to have opposite signs and pin a state to a corner. Without such bulk and boundary constraints, a local potential can create an ordinary corner bound state. Symmetry tests and adiabatic deformations distinguish the mechanisms.

Quasicrystals lack ordinary translation periodicity, so a Bloch Brillouin-zone integral cannot be applied blindly. Higher-order topology in quasicrystals can be described through real-space models and boundary masses[12]. Numerically construct a finite Hamiltonian and occupied projector P, then cross-check appropriate real-space invariants, local density, and size scaling. A few corner states in a finite image are not sufficient independent evidence: exclude geometric defects, local potentials, and accidental effects of termination.

3.8.8 Material criteria for topological bands

A material analysis should form a connected sequence: select relevant orbitals and symmetry representations; construct or fit a low-energy Hamiltonian; check the global gap and Fermi energy; compute occupied-subspace invariants; calculate the corresponding surface spectrum; then predict observables and symmetry-breaking perturbations. Each step constrains the others. An attractive surface plot cannot replace a bulk invariant, while a nonzero bulk invariant does not ensure that chemical potential and contacts satisfy transport conditions.

1. Add a time-reversal-preserving but inversion-breaking perturbation to B15. Replace the parity test with a Wilson loop, because parity is no longer a conserved label.

2. Continuously shrink the node separation in B17 and compute the Hall response and arc length. Local Weyl theory remains useful before annihilation, but the complete lattice model describes the final transition.

3. Perturb B18 with and without its protecting symmetries. Record bulk gap, edge gap, corner-state energy, and corner charge. These quantities need not change together: departure from zero energy and loss of every topological feature are different statements.

Part III

Semiclassical and quantum transport

Chapter 4

Motion and quantum geometry in periodic bands

4.1 From a Bloch eigenstate to a localized packet

The eigenvalue equation in a periodic crystal is $H_{\mathbf{k}}u_{n\mathbf{k}} = \epsilon_n(\mathbf{k})u_{n\mathbf{k}}$. A single Bloch state extends throughout the crystal and cannot specify a localized particle position. Semiclassics uses a narrow packet in one isolated band, $|W\rangle = \int a(\mathbf{k})\,|\psi_{n\mathbf{k}}\rangle\,\mathrm{d}\mathbf{k}$. It requires $a \ll \Delta r \ll L_{\text{field}}$, so that $\Delta k \sim 1/\Delta r$ covers only a smooth patch of the band. Drive frequency, scattering width and field-induced interband matrix elements must also be small relative to band separation. Near a degeneracy, a multiband subspace is necessary; a finite-density Dirac orbit can still admit a single-band treatment when it stays away from the node. The Hellmann–Feynman identity gives the group velocity and inverse effective-mass tensor:

$$v_{n,i} = \hbar^{-1}\langle u_n|\partial_{k_i}H_{\mathbf{k}}|u_n\rangle = \hbar^{-1}\partial_{k_i}\epsilon_n, \tag{4.1}$$

$$\hbar\dot{\mathbf{k}} = -e(\mathbf{E} + \mathbf{v}_n \times \mathbf{B}), \qquad (M_n^{-1})_{ij} = \hbar^{-2}\partial_{k_i}\partial_{k_j}\epsilon_n. \tag{4.2}$$

Crystal momentum $\hbar\mathbf{k}$ is not the bare mechanical momentum. Mass is generally a momentum-dependent tensor. Negative curvature near a band maximum can be described using holes. The group-velocity current of a filled band is $-(e/\hbar)\int_{\text{BZ}}[\mathrm{d}k]\nabla_k\epsilon = 0$, because opposite Brillouin-zone faces cancel. After removing electrons near a maximum, define $\mathbf{q}_h = -(\mathbf{k}_e - \mathbf{k}_v)$ and $\epsilon_h(\mathbf{q}_h) = \epsilon_v - \epsilon_e(\mathbf{k}_v - \mathbf{q}_h)$. Then $\mathbf{v}_h = \mathbf{v}_e$ and $\hbar\dot{\mathbf{q}}_h = +e(\mathbf{E} + \mathbf{v}_h \times \mathbf{B})$. A vanishing filled-band group current does not imply a vanishing topological Hall response.

4.1.1 Worked example T3 Orbit mass and a graphene device

A magnetic field does no work. Energy and the momentum component along $\mathbf{B}$ remain fixed, so an orbit is the intersection of a constant-energy surface and a plane normal to the field. Integrating around it gives

$$T_c = \frac{\hbar^2}{e|B|}\oint \frac{\mathrm{d}\ell_k}{|\nabla_{k,\perp}\epsilon|}, \qquad m_c = \frac{\hbar^2}{2\pi}\left|\frac{\partial A}{\partial\epsilon}\right|, \qquad \omega_c = \frac{e|B|}{m_c}. \tag{4.3}$$

The area derivative follows by moving the contour normally by $\mathrm{d}\epsilon/|\nabla\epsilon|$ and summing the added strips. An elliptic parabola, $\epsilon = \hbar^2k_x^2/(2m_x) + \hbar^2k_y^2/(2m_y)$, gives $m_c = \sqrt{m_xm_y}$. For graphene, $\epsilon = \hbar v_F k$ and spin-valley degeneracy $g = 4$ imply $n = k_F^2/\pi$ and $m_c = \hbar k_F/v_F = E_F/v_F^2$. A zero radial second derivative does not imply zero orbit mass: the magnetic field rotates the velocity direction. Take $n = 10^{12}\,\mathrm{cm}^{-2}$, $v_F = 10^6\,\mathrm{m/s}$ and $\mu_{\text{tr}} = 1\,\mathrm{m}^2/(\mathrm{Vs})$:

$$k_F = 1.7725\times10^8\,\mathrm{m}^{-1}, \qquad E_F = 116.67\,\mathrm{meV}, \qquad m_c = 0.02052m_e, \tag{4.4}$$

$$\tau_{\text{tr}} = \mu_{\text{tr}}m_c/e = 0.11667\,\mathrm{ps}, \qquad \ell = 116.67\,\mathrm{nm}, \qquad k_F\ell = 20.68, \tag{4.5}$$

$$\sigma_{2D} = ne\mu_{\text{tr}} = 1.6022\,\mathrm{mS}, \qquad R_\square = 624.15\,\Omega. \tag{4.6}$$

A uniform diffusive channel of length $2\,\mu$m and width $5\,\mu$m gives $G = 4.006\,$mS. If its length is reduced to $20\,$nm $\ll \ell$, extrapolating $G = \sigma W/L$ is no longer justified. Contacts and transmission become essential. The same band thus requires a different transport description at a different device length.

4.2 Bloch oscillations and scattering

4.2.1 Worked example T4 Bloch oscillations and their scattering limit

Consider a cosine miniband of period d and full width Δ. Integrating the acceleration theorem and velocity in a constant positive field yields

$$\epsilon(k) = -\frac{\Delta}{2}\cos(kd), \qquad k(t) = k_0 - eEt/\hbar, \qquad \omega_B = eEd/\hbar, \quad (4.7)$$

$$v(t) = \frac{\Delta d}{2\hbar}\sin(k_0 d - \omega_B t), \quad x(t) - x(0) = \frac{\Delta}{2eE}[\cos(k_0 d - \omega_B t) - \cos(k_0 d)]. \quad (4.8)$$

The conserved quantity is $\epsilon(k) + eEx$, and the peak-to-peak excursion is $\Delta/(e|E|)$. For $d = 10\,$nm, $\Delta = 20\,$meV and $E = 4\,$kV/cm, $f_B = eEd/h = 0.967\,$THz, $T_B = 1.034\,$ps and the excursion is $50\,$nm. If each collision resets the electron to the band bottom, exponentially distributed free-flight times give

$$\overline{v} = -\frac{\Delta d}{2\hbar}\int_0^\infty \frac{\mathrm{d}t}{\tau} e^{-t/\tau}\sin\omega_B t = -\frac{\Delta d}{2\hbar}\frac{\omega_B\tau}{1+\omega_B^2\tau^2}. \quad (4.9)$$

The weak-field limit recovers Drude drift, while strong fields give negative differential velocity. This result belongs to a reset-scattering model; heating, space-charge domains and interband tunnelling can change it. Optical Bloch-oscillation and radiation measurements in semiconductor superlattices test the field-dependent frequency, rather than directly measuring this ideal stationary drift curve[17, 18].

4.3 Position, Berry connection and anomalous velocity

Evaluating $\langle W|\mathbf{r}|W\rangle$ by converting position into a momentum derivative produces an envelope-phase contribution and $\mathbf{A}_n = i\langle u_n|\nabla_k u_n\rangle$. Under $u_n \to e^{i\phi}u_n$, $\mathbf{A}_n \to \mathbf{A}_n - \nabla\phi$; the envelope changes so that physical position stays invariant. Temporarily omitting the orbital moment, the packet Lagrangian is

$$L = (\hbar\mathbf{k} - e\mathbf{A}^{\mathrm{em}})\cdot\dot{\mathbf{r}} + \hbar\mathbf{A}_n\cdot\dot{\mathbf{k}} - \epsilon_n + e\varphi, \qquad \dot{\mathbf{r}} = \frac{1}{\hbar}\nabla_k\epsilon_n - \dot{\mathbf{k}}\times\boldsymbol{\Omega}_n, \quad \boldsymbol{\Omega}_n = \nabla_k\times\mathbf{A}_n. \quad (4.10)$$

The anomalous velocity comes from the momentum dependence of eigenstates, and cannot be inferred from the dispersion alone[15]. At zero magnetic field, $\dot{\mathbf{r}} = \mathbf{v} + (e/\hbar)\mathbf{E}\times\boldsymbol{\Omega}$. Multiplying by electron charge and summing occupied states gives

$$\sigma_{xy}^{\mathrm{int}} = -\frac{e^2}{\hbar}\sum_n \int [\mathrm{d}k] f_n \Omega_{n,z}, \qquad \sigma_{xy}^{2D} = -C\frac{e^2}{h}, \quad C = \frac{1}{2\pi}\sum_{n\in\mathrm{occ}}\int_{\mathrm{BZ}}\Omega_{n,z}\,\mathrm{d}^2k. \quad (4.11)$$

Time reversal makes the curvature of paired states odd, cancelling the equilibrium linear charge Hall response. Valley-resolved curvature can nevertheless be nonzero. A single-valley integral is not the sample's total Chern number; an integer invariant requires a full lattice model and its entire Brillouin zone.

4.3.1 Worked example T5 Curvature and metric of a massive Dirac valley

Take $H_\xi = \hbar v(\xi q_x \sigma_x + q_y \sigma_y) + m\sigma_z$, with $\xi = \pm 1$ and $E = \sqrt{m^2 + \hbar^2 v^2 q^2}$. Differentiating the two-level projectors $P_s = (1 + s\hat{\mathbf{d}} \cdot \boldsymbol{\sigma})/2$ gives, for $s = \pm 1$,

$$\Omega_{s,z} = -s\xi \frac{m(\hbar v)^2}{2E^3}, \tag{4.12}$$

$$g_{ij} = \frac{1}{4}\partial_{q_i}\hat{\mathbf{d}} \cdot \partial_{q_j}\hat{\mathbf{d}} = \frac{(\hbar v)^2}{4E^2}\left[\delta_{ij} - \frac{(\hbar v)^2 q_i q_j}{E^2}\right], \tag{4.13}$$

$$\det g = \Omega_z^2/4. \tag{4.14}$$

The metric gives the quadratic loss of overlap magnitude, while curvature gives the phase accumulated around a small loop. They are the real and imaginary parts of quantum geometry, not the curvature mass of a band. For $m = 25\,\text{meV}$ and $v = 10^6\,\text{m/s}$, $|\Omega(0)| = 346.6\,\text{nm}^2$ and $g_{xx}(0) = g_{yy}(0) = 173.3\,\text{nm}^2$. At $E = 2m$, the curvature is one eighth of its edge value. Opposite valleys cancel in charge Hall response and add in valley response. A large geometric hot spot therefore does not by itself establish a quantum anomalous Hall insulator.

4.4 Orbital moments and phase-space state counting

Packet self-rotation generates an orbital magnetic moment $\mathbf{m}_n$, shifting the energy to $\widetilde{\epsilon}_n = \epsilon_n - \mathbf{m}_n \cdot \mathbf{B}$. Curvature also modifies the phase-space measure[16]:

$$D_n = 1 + \frac{e}{\hbar}\mathbf{B} \cdot \boldsymbol{\Omega}_n, \qquad n = \sum_n \int [\mathrm{d}k] D_n f(\widetilde{\epsilon}_n - \mu), \tag{4.15}$$

$$D_n \dot{\mathbf{r}} = \widetilde{\mathbf{v}}_n + \frac{e}{\hbar}\mathbf{E} \times \boldsymbol{\Omega}_n + \frac{e}{\hbar}(\widetilde{\mathbf{v}}_n \cdot \boldsymbol{\Omega}_n)\mathbf{B}, \tag{4.16}$$

$$D_n \hbar \dot{\mathbf{k}} = -e\mathbf{E} - e\widetilde{\mathbf{v}}_n \times \mathbf{B} - \frac{e^2}{\hbar}(\mathbf{E} \cdot \mathbf{B})\boldsymbol{\Omega}_n. \tag{4.17}$$

At fixed density, $\mu(B)$ must also be solved again. Adding anomalous velocity to an otherwise unchanged integral while omitting D and the moment loses terms at the same order in magnetothermoelectric response. This is an isolated-band packet expansion and cannot be carried through a singular Weyl node without a separate quantum or multiband treatment.

4.5 Exercises and solution notes

1. Find v_i and M_{ij}^{-1} for $\epsilon = -2t(\cos k_x a + \cos k_y a)$. Solution: $v_x = 2ta \sin k_x a/\hbar$, $(M^{-1})_{xx} = 2ta^2 \cos k_x a/\hbar^2$, and the mixed term vanishes. Even along one Fermi contour, curvature can change sign.

2. Quadruple the T3 density at fixed v_F. Then k_F, E_F, m_c double. If mobility is held fixed, τ also doubles; this is different from assuming a density-independent lifetime.

3. Multiply each T5 eigenvector by a random phase before finite differentiation. What happens? Solution: derivatives acquire gauge noise. Use projectors, interband matrix elements or closed overlap links instead.

Chapter 5

Boltzmann transport and thermoelectric response

5.1 The Boltzmann equation and collision integral

During a short time step, particles that do not scatter move along phase-space trajectories. The total derivative of $f(\mathbf{r},\mathbf{k},t)$ therefore equals the collision-induced change:

$$\partial_t f + \dot{\mathbf{r}}\cdot\nabla_r f + \dot{\mathbf{k}}\cdot\nabla_k f = I[f], \quad I_{\mathbf{k}} = \int [\mathrm{d}k']\{W_{\mathbf{k}'\mathbf{k}} f_{\mathbf{k}'}(1-f_{\mathbf{k}}) - W_{\mathbf{k}\mathbf{k}'} f_{\mathbf{k}}(1-f_{\mathbf{k}'})\}. \tag{5.1}$$

The first term scatters particles in, the second scatters them out, and $(1-f)$ blocks occupied final states. Elastic reciprocal single-particle scattering has $W_{kk'} = W_{k'k}$, so the quadratic terms cancel: $I_k = \int W_{kk'}(f_{k'} - f_k)$. Equilibrium occupations are equal on an energy shell, ensuring $I[f_0] = 0$. Particle conservation requires $\int I[f][\mathrm{d}k] = 0$. A naive relaxation term $-(f-f_0)/\tau$ with an arbitrarily fixed reference distribution can violate this in an inhomogeneous problem; a local chemical potential may need to enforce number conservation.

5.1.1 Worked example T6 Two graphene scattering times

For weak dilute impurities, the golden rule gives $W_{kk'} = (2\pi/\hbar) n_i |U_{kk'}|^2 \delta(\epsilon_k - \epsilon_{k'})$. Spectral width counts all scattering events, whereas current relaxation weights the lost velocity direction. On a circular Fermi surface,

$$\frac{1}{\tau_q} \propto \int_0^{2\pi} \mathrm{d}\theta\, |U(\theta)|^2 F(\theta), \qquad \frac{1}{\tau_{\mathrm{tr}}} \propto \int_0^{2\pi} \mathrm{d}\theta\, |U(\theta)|^2 F(\theta)(1-\cos\theta). \tag{5.2}$$

A conduction-band spinor in gapless graphene is $(1, e^{i\phi})/\sqrt{2}$, giving $F(\theta) = (1+\cos\theta)/2$. For a scalar, short-range, intravalley potential, the angular integrals are π and $\pi/2$, so $\tau_{\mathrm{tr}} = 2\tau_q$. This explicitly demonstrates spinor-suppressed backscattering[19]. A long-range potential favours small angles and can increase the ratio. Intervalley scattering, a mass term or magnetic impurities modify the spinor factor. The factor of two is not universal across graphene samples.

5.2 Trajectory history and the Chambers formula

In the relaxation-time approximation, $(\mathrm{d}/\mathrm{d}t + 1/\tau)\delta f = \mathcal{D}$ along the unperturbed trajectory. The solution that equilibrates in the remote past is

$$\delta f(t) = \int_{-\infty}^{t} \mathrm{d}t'\, \exp\left[-\int_{t'}^{t} \frac{\mathrm{d}s}{\tau(s)}\right] \left(-\frac{\partial f_0}{\partial \epsilon}\right) \mathbf{v}(t')\cdot\left[-e\boldsymbol{\mathcal{E}}(t') - \frac{\epsilon-\mu}{T}\nabla T(t')\right], \qquad \boldsymbol{\mathcal{E}} = \mathbf{E} + \frac{\nabla\mu}{e}. \tag{5.3}$$

The kernel is a survival probability for orbital memory. It follows from an integrating factor, rather than being an extra empirical weight. At zero field with constant τ, a DC drive reduces the history integral to τ; an AC drive gives $\tau/(1-i\omega\tau)$. In a magnetic field, $\mathbf{v}(t')$ changes around the constant-energy orbit and must remain inside the integral. This gives the Chambers form

$$\sigma_{ij} = e^2 \sum_n \int [\mathrm{d}k] \left(-\frac{\partial f_0}{\partial \epsilon}\right) v_i(0) \int_{-\infty}^{0} \mathrm{d}t\, e^{t/\tau} v_j(t). \tag{5.4}$$

A parabolic circular orbit has sinusoidal $v_x(t)$ and $v_y(t)$; the integrals recover the Drude field tensor exactly. Open or non-spherical orbits have directional memory and can produce magnetoresistance even in one band. The previous zero-magnetoresistance result depended on an isotropic parabola.

5.3 Heat current and thermoelectric response tensors

Heat current is energy flow minus chemical-work transport: $\mathbf{j}_Q = \sum_n \int [\mathrm{d}k](\epsilon_n - \mu)\mathbf{v}_n \delta f_n$. Define a spectral conductivity that includes e^2, and its moments,

$$\Sigma_{ij}(\epsilon) = e^2 \sum_n \int [\mathrm{d}k]\, \tau_n v_{n,i} v_{n,j} \delta(\epsilon - \epsilon_n), \tag{5.5}$$

$$L_{ij}^{(r)} = \int \mathrm{d}\epsilon\, \Sigma_{ij}(\epsilon)(\epsilon-\mu)^r(-\partial_\epsilon f_0), \tag{5.6}$$

$$\mathbf{j} = \boldsymbol{\sigma}\boldsymbol{\mathcal{E}} - \boldsymbol{\alpha}\nabla T, \qquad \sigma = L^{(0)}, \qquad \alpha = -\frac{L^{(1)}}{eT}, \tag{5.7}$$

$$\mathbf{j}_Q = T\widetilde{\boldsymbol{\alpha}}\boldsymbol{\mathcal{E}} - \overline{\boldsymbol{\kappa}}\nabla T, \qquad \overline{\kappa} = \frac{L^{(2)}}{e^2 T}, \qquad \widetilde{\alpha}(B) = \alpha^T(-B). \tag{5.8}$$

At zero field with time-reversal symmetry, $\widetilde{\alpha} = \alpha$. In a magnetic material, the magnetic order must also be reversed in the reciprocity relation. Under $\mathbf{j} = 0$, first solve for the electric field and then substitute into the heat current:

$$\boldsymbol{S} = \boldsymbol{\sigma}^{-1}\boldsymbol{\alpha}, \qquad \boldsymbol{\kappa} = \overline{\boldsymbol{\kappa}} - T\widetilde{\boldsymbol{\alpha}}\boldsymbol{\sigma}^{-1}\boldsymbol{\alpha}, \qquad \boldsymbol{\mathcal{E}} = \boldsymbol{S}\nabla T. \tag{5.9}$$

Matrix order matters. $\overline{\kappa}$ is a fixed-field coefficient, whereas the usual open-circuit measurement gives κ; neglecting thermoelectric counterflow overestimates heat conduction. The Sommerfeld expansion gives $L^{(1)} = (\pi^2/3)(k_B T)^2 \Sigma'(\mu)$ and the tensor Mott relation $\alpha = -(\pi^2 k_B^2 T/3e)\partial_\mu \sigma$. Wiedemann–Franz is a leading low-temperature, elastic, degenerate result. Phonon drag, inelastic collisions and sharp energy dependence can violate it.

5.3.1 Worked example T7 Thermopower as a test of graphene scattering models

Gapless graphene has $\nu(\epsilon) \propto |\epsilon|$ and a constant speed. If $\tau \propto \epsilon^r$, then on the electron side $\Sigma \propto \epsilon^{r+1}$, giving

$$S = -\frac{\pi^2 k_B^2 T}{3e}\frac{r+1}{\mu}. \qquad \mu = 0.2\,\mathrm{eV},\ T = 100\,\mathrm{K}: \quad S = -(r+1)\,12.215\,\mu\mathrm{V/K}. \tag{5.10}$$

Scattering amplitudes can be adjusted so that these models share the same conductivity at one density, but they do not generally share thermopower. The exponents $r = -1, 0, 1$ give $0, -12.215, -24.430\,\mu\mathrm{V/K}$.

The zero is a cancellation within an ideal power law and low-temperature approximation; residual density or drag can spoil it. For a three-dimensional Weyl cone, $\nu \propto \epsilon^2$, so the same constant speed changes the exponent to $r + 2$. Thermopower can therefore test dimensionality as well as scattering.

5.4 Transport in compensated spin channels

5.4.1 Worked example T8 Transverse spin current in compensated spin channels

Take two spin-conserving elliptical parabolic channels, with $\sigma^{\uparrow} = \mathrm{diag}(a, b)$ and $\sigma^{\downarrow} = \mathrm{diag}(b, a)$. Their charge sum is $(a + b)I$, while their difference is $(a - b)\,\mathrm{diag}(1, -1)$. Under a field along $[11]$, transverse channel currents oppose one another: transverse charge flow cancels but a spin flow remains. For $a = 3$, $b = 1$ in common conductivity units, drive along $\hat{e}_{\parallel} = (1, 1)/\sqrt{2}$ and project onto $\hat{e}_{\perp} = (1, -1)/\sqrt{2}$. The transverse channel difference is $2E$ and the longitudinal charge current is $4E$. No Berry curvature is required; this is not an antisymmetric charge Hall effect. It illustrates the link between exchange anisotropy, altermagnetism and transport. With spin-orbit coupling, spin is not conserved and the spin-current definition needs renewed attention.

5.5 Intrinsic and scattering mechanisms of the anomalous Hall effect

The intrinsic contribution comes from occupied-state curvature. An antisymmetric scattering probability produces skew scattering; a displacement during scattering and its associated distribution correction produce side jump. In a simple weakly scattered metal, skew conductivity often scales as τ, whereas intrinsic and side-jump terms often scale as τ^0. Multiple scattering channels, band hot spots and changing temperature make attribution from a resistivity scaling law alone unreliable. A quantitative comparison of longitudinal and transverse responses requires the same magnetization, density and temperature conditions.

5.6 Berry-curvature dipoles and nonlinear Hall response

In a time-reversal-invariant metal without inversion, $\Omega(\mathbf{k}) = -\Omega(-\mathbf{k})$ and its equilibrium integral cancels. A field generates an odd δf; multiplying it by the odd curvature coefficient can leave an even second-order current. Define the Berry-curvature dipole and integrate by parts:

$$D_{ab} = \sum_n \int [\mathrm{d}k] f_n \partial_{k_a} \Omega_{n,b} = \hbar \sum_n \int [\mathrm{d}k] v_{n,a} \Omega_{n,b} (-\partial_\epsilon f_n), \qquad j_a^{(2)} = \frac{e^3 \tau}{\hbar^2} \epsilon_{abc} E_b E_d D_{dc}. \tag{5.11}$$

This is the constant-τ, DC expression retaining only the Berry-dipole mechanism[20]. For a real AC field $E_0 \cos \omega t$, rectified and second-harmonic components must be obtained from products of real fields; a factor of $1/2$ cannot be omitted. Different complex-amplitude conventions change apparent prefactors. Crystal symmetry may still force $D = 0$; tilted massive Dirac valleys provide a model in which some cancellations are removed. Second-order thermal driving introduces energy weights, energy magnetization and thermal boundaries. Replacing E by ∇T does not produce a complete nonlinear thermal theory.

5.7 Exercises and numerical implementation

1. Integrate all three $L^{(r)}$ numerically and compare with the low-temperature Mott value. Use $\mu = 0.2\,\mathrm{eV}$ and 10–500 K. Extend the energy window at least to $\mu \pm 12 k_B T$ and check the band-bottom cutoff.
2. Recover the Drude matrix from the Chambers integral, then replace the band by a square-lattice dispersion. Monitor energy drift as an orbit-integrator error and retain a history of at least 10τ.
3. For forward Gaussian scattering $|U(\theta)|^2 \propto e^{-\theta^2/\theta_0^2}$, calculate $\tau_{\mathrm{tr}}/\tau_q$ against θ_0. In the small-angle limit it grows as θ_0^{-2}.

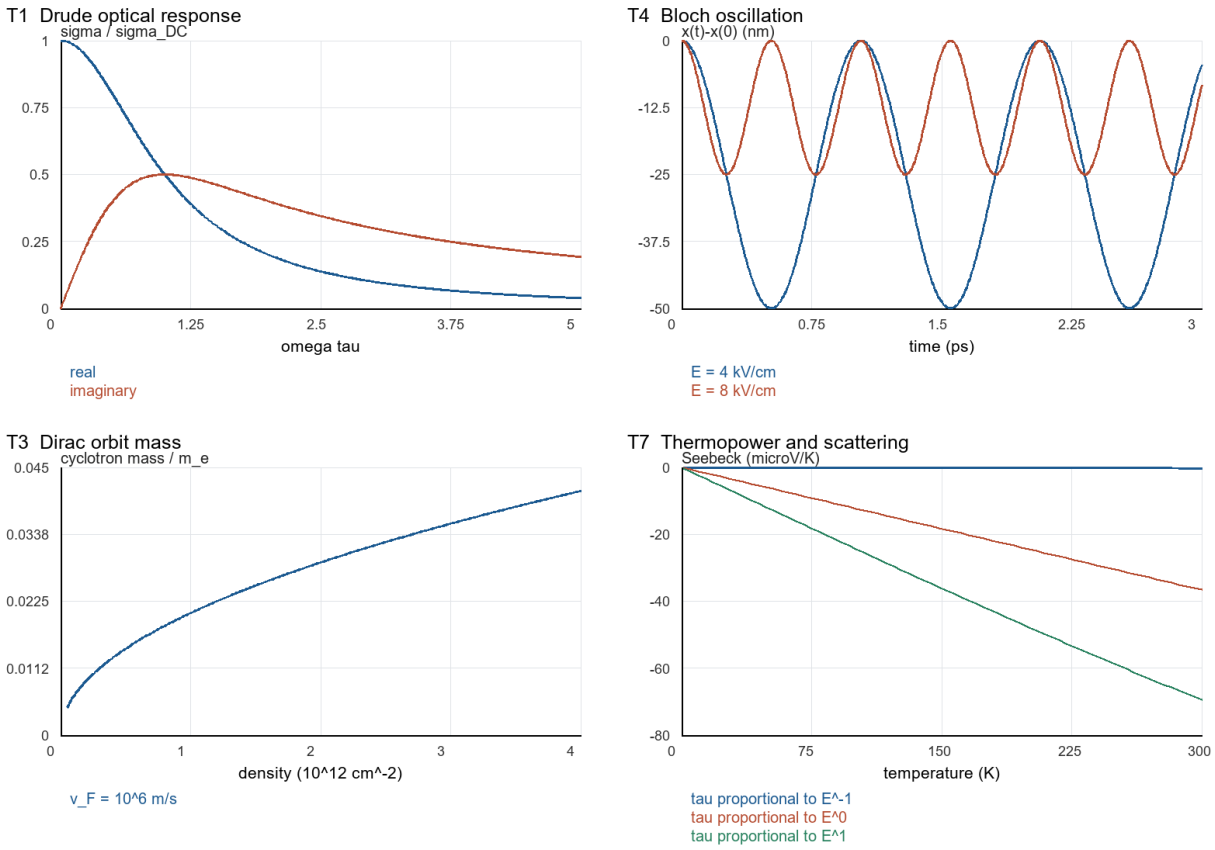

Figure 5.1: Model calculations for T1, T3, T4 and T7. Optical response separates real and imaginary parts; Bloch trajectories change the field at fixed miniband; graphene orbit mass varies with density; thermopower uses full energy-moment integration. All panels are calculations from the stated models and parameters.

5.8 Finite-field transport and thermoelectric boundaries

5.8.1 Worked example T9 Electron–hole compensation and nonsaturating magnetoresistance

Specify an electron density n, a hole density p, and positive mobilities u_e, u_h. The symbol u denotes mobility, distinct from the chemical potential μ. Solve a Drude tensor for each carrier and add conductivities, not resistivities. With $\sigma_H = \sigma_{yx} = -\sigma_{xy}$,

$$\sigma_d = e\left[\frac{nu_e}{1+u_e^2B^2} + \frac{pu_h}{1+u_h^2B^2}\right], \tag{5.12}$$

$$\sigma_H = eB\left[\frac{nu_e^2}{1+u_e^2B^2} - \frac{pu_h^2}{1+u_h^2B^2}\right], \tag{5.13}$$

$$\rho_{xx} = \frac{\sigma_d}{\sigma_d^2+\sigma_H^2} = \frac{1}{e}\frac{(nu_e+pu_h)+(nu_eu_h^2+pu_hu_e^2)B^2}{(nu_e+pu_h)^2+(p-n)^2u_e^2u_h^2B^2}, \tag{5.14}$$

$$\rho_{yx} = -\frac{\sigma_H}{\sigma_d^2+\sigma_H^2} = \frac{B}{e}\frac{pu_h^2-nu_e^2+(p-n)u_e^2u_h^2B^2}{(nu_e+pu_h)^2+(p-n)^2u_e^2u_h^2B^2}. \tag{5.15}$$

These expressions can be checked by directly inverting a 2×2 matrix. Setting $p=0$ recovers zero longitudinal magnetoresistance for one electron band. At $p=n$, the B^2 denominator term vanishes, giving

$$\rho_{xx} = \frac{1+u_eu_hB^2}{en(u_e+u_h)}, \qquad \rho_{yx} = \frac{B(u_h-u_e)}{en(u_e+u_h)}, \qquad \text{MR} = \frac{\rho_{xx}(B)-\rho_{xx}(0)}{\rho_{xx}(0)} = u_eu_hB^2. \tag{5.16}$$

For $u_e=1$ and $u_h=0.5\,\mathrm{m}^2/(\mathrm{Vs})$, fields of 2 and 5 T give $\rho_{xx}/\rho_{xx}(0)=3$ and 13.5, or magnetoresistance of 200% and 1250%. Exact density compensation does not imply zero Hall voltage when mobilities differ. With equal mobilities $u_e=u_h=u$ and $p=rn$, the normalized result simplifies further:

$$\frac{\rho_{xx}(B)}{\rho_{xx}(0)} = \frac{(1+r)^2(1+u^2B^2)}{(1+r)^2+(r-1)^2u^2B^2} \xrightarrow[B\to\infty]{r\neq 1} \frac{(1+r)^2}{(r-1)^2}. \tag{5.17}$$

For $r=0.8, u=1$, $B=5\,\mathrm{T}$ gives a normalized value 19.87 and the asymptotic saturation value is 81; $r=0$ stays at unity. At fixed mobilities, the saturation field scale decreases as $|p-n|$ grows. One longitudinal curve cannot uniquely determine four model parameters. A joint fit to the Hall response and independent density or mass constraints is needed to restrict the parameters.

5.8.2 Weak- and strong-field Hall limits in multiband systems

The weak-field expansion gives

$$R_H = \lim_{B\to 0}\frac{\rho_{yx}}{B} = \frac{pu_h^2-nu_e^2}{e(pu_h+nu_e)^2}. \tag{5.18}$$

For $p=n/4$ and $u_h=3u_e$, the numerator is $(9/4-1)nu_e^2>0$. Holes are fewer but the Hall coefficient is positive. In the very-high-field, uncompensated limit with every pocket satisfying $uB\gg 1$, $\rho_{yx}/B\to 1/[e(p-n)]$. The different weights in these two limits are one origin of nonlinear Hall curves in multiband metals.

5.8.3 Worked example T10 Nernst response and Sondheimer cancellation

For an isotropic plane, write $\sigma=\left(\begin{smallmatrix} d & -h \\ h & d\end{smallmatrix}\right)$ and $\alpha=\left(\begin{smallmatrix} a & -b \\ b & a\end{smallmatrix}\right)$. With no transverse temperature gradient and no current in either direction, direct multiplication gives

$$S_{xx} = \frac{da+hb}{d^2+h^2}, \qquad S_{yx} = \frac{db-ha}{d^2+h^2} = -\frac{\pi^2k_B^2T}{3e}\,\partial_\mu \arctan(h/d). \tag{5.19}$$

The Nernst signal measures the energy derivative of the Hall angle, not α_{yx} alone. For one parabolic electron band, $h/d = u(\epsilon)B$. Energy-independent mobility gives $S_{yx} = 0$ even though both σ_{yx} and α_{yx} can be nonzero. If $u \propto \epsilon^r$, the weak-field coefficient is $S_{yx}/B = -(\pi^2 k_B^2 T/3e)ru/\mu$. For $r = 1$, $T = 100\,\mathrm{K}$, $\mu = 0.2\,\mathrm{eV}$ and $u = 1\,\mathrm{m}^2/(\mathrm{Vs})$, it is $-12.215\,\mu\mathrm{V}/(\mathrm{K\,T})$. Reversing the voltage leads changes the reported sign, so specify the definition $E_y/\partial_x T$.

5.8.4 Thermal boundary conditions and measured thermopower

For adiabatic sides the condition is $j_{Q,y} = 0$, not $\partial_y T = 0$. Using the already electrically open-circuit κ gives $\partial_y T = -(\kappa_{yx}/\kappa_{yy})\partial_x T$, and hence

$$S_{xx}^{\mathrm{ad}} = S_{xx} - S_{xy}\frac{\kappa_{yx}}{\kappa_{yy}}, \qquad S_{yx}^{\mathrm{ad}} = S_{yx} - S_{yy}\frac{\kappa_{yx}}{\kappa_{yy}}. \tag{5.20}$$

A large transverse thermoelectric coefficient does not automatically give high conversion efficiency. Load power, thermal leakage, contacts, current paths and thermal boundaries all matter. The scalar power factor $S^2\sigma$ applies only after a one-dimensional geometry has been specified. In a magnetic field, the effective device response follows from the tensors together with the actual electrical and thermal boundaries.

5.8.5 Weyl nodes and axial population under parallel fields

For two opposite-chirality nodes, define $n_5 = n_+ - n_-$ and let τ_v explicitly relax this difference. The low-energy anomaly-pumping equation is[21]

$$\frac{\mathrm{d}n_5}{\mathrm{d}t} = \frac{e^2}{2\pi^2\hbar^2}\mathbf{E}\cdot\mathbf{B} - \frac{n_5}{\tau_v}. \qquad \mu_5 = \frac{\mu_+ - \mu_-}{2}, \quad n_5 = \chi_5\mu_5. \tag{5.21}$$

In steady state, $n_5 \propto \tau_v \mathbf{E}\cdot\mathbf{B}$. The transport current generated by node imbalance, $\mathbf{j}_{\mathrm{anom}} = [e^2/(2\pi^2\hbar^2)]\mu_5\mathbf{B}$, gives

$$\Delta\sigma_{\parallel} = \frac{e^4\tau_v B^2}{4\pi^4\hbar^4\chi_5}, \qquad \chi_5 = \frac{\mu^2}{\pi^2\hbar^3 v^3} \quad \text{(two isotropic nodes at zero temperature).} \tag{5.22}$$

Here μ_5 is a driven nonequilibrium imbalance; the expression does not imply a persistent equilibrium lattice current. τ_v, τ_{tr} and τ_q describe different processes. The weak-field semiclassical form also assumes separate node pockets, well-defined quasiparticles and fields below the quantum limit. A negative longitudinal magnetoresistance alone does not exclude current jetting, ordinary bands, weak localization or magnetic scattering, and therefore cannot establish a chiral anomaly.

5.8.6 Exercises and solution notes

1. In T9, compute both the direct matrix inverse and the closed expressions over 0–10 T. They should agree to floating-point accuracy throughout the sweep, not merely at zero field.
2. Keep $nu_e + pu_h$ fixed and construct two parameter sets with the same zero-field resistivity but different Hall slopes. This demonstrates the non-uniqueness of a one-curve fit.
3. Integrate the finite-temperature moments for T10 and locate a 5% departure from the Mott approximation. The answer depends on the specified band bottom and scattering function; it is not a universal temperature threshold.

Chapter 6

Quantum oscillations and band measurements in the quantum limit

6.1 Orbital deflection, Landau quantization and the quantum limit

Orbital deflection requires $\omega_c \tau_{\mathrm{tr}} \gtrsim 1$. Resolved oscillations require Landau-level spacing to survive thermal and spectral broadening. The quantum limit requires only the lowest few Landau branches to be occupied. These conditions involve mobility, τ_q and particle number respectively, and generally occur at different fields. Strong magnetoresistance does not establish Landau quantization; many visible oscillations do not establish the quantum limit.

6.2 Landau levels and their degeneracy for a parabolic band

For $B > 0$, use $\mathbf{A} = (0, Bx, 0)$. The electron Hamiltonian is

$$H = \frac{p_x^2 + (p_y + eBx)^2}{2m}, \qquad \psi = e^{ik_y y}\phi(x - X), \tag{6.1}$$

$$X = -\ell_B^2 k_y, \quad \ell_B = \sqrt{\frac{\hbar}{eB}}, \qquad E_N = \hbar\omega_c(N + 1/2). \tag{6.2}$$

Adjacent k_y values are separated by $2\pi/L_y$, and oscillator centres must fit within width L_x. Each independent spin-valley flavour therefore has $N_\phi = L_x L_y eB/h$ states per Landau level. In three dimensions, motion along the field remains free: $E_{N,k_z} = \hbar\omega_c(N+1/2) + \hbar^2 k_z^2/(2m_z)$. Levels become one-dimensional branches. Include each spin or valley degeneracy exactly once.

6.3 Onsager quantization and Fermi-surface cross sections

For a well-defined orbit at high index, action quantization gives

$$A(\epsilon, k_\parallel) = \frac{2\pi eB}{\hbar}(N + \gamma), \qquad \gamma = \frac{1}{2} - \frac{\Phi_B}{2\pi}, \tag{6.3}$$

$$F = \frac{\hbar}{2\pi e} A(E_F), \qquad \Delta(1/B) = 1/F. \tag{6.4}$$

Berry, orbital-moment, Zeeman and three-dimensional stationary-phase corrections must be evaluated for the model being used. A three-dimensional signal integrates over $k_\parallel$. Rapidly varying phases cancel except near stationary sections with $\partial A/\partial k_\parallel = 0$. One measured frequency therefore gives an extremal area, not the entire three-dimensional Fermi surface.

6.3.1 Worked example T11 Dispersion inferred from frequency and mass

The T3 graphene parameters give $A = \pi k_F^2 = 9.870 \times 10^{16}\,\mathrm{m}^{-2}$. Substituting into $F = \hbar A/(2\pi e)$ gives $F = 10.339\,\mathrm{T}$. First obtain $k_F^2 = \pi n$, then multiply by one more factor of π to obtain the area; do not introduce the spin-valley degeneracy again in the frequency. The corresponding mass is $m_c = 0.02052 m_e$. A measured $m_c \propto \sqrt{n}$ across gate voltages supports a linear dispersion rather than a fixed-curvature parabola. More generally, F determines area while $m_c(E)$ gives $\partial A/\partial E = 2\pi m_c/\hbar^2$. For a nearly circular orbit, $k = \sqrt{A/\pi}$ and

$$\frac{\mathrm{d}E}{\mathrm{d}k} = \frac{\hbar^2 k}{m_c(k)}, \qquad E(k) - E(k_0) = \int_{k_0}^{k} \frac{\hbar^2 k'}{m_c(k')}\,\mathrm{d}k'. \tag{6.5}$$

The integral also needs an energy reference. For a noncircular orbit the area derivative remains valid, but $\sqrt{A/\pi}$ is only a circular-equivalent wave vector, not the true radius in each direction.

6.4 Deriving Lifshitz–Kosevich thermal damping

A zero-temperature harmonic has the form $\cos[2\pi p F(E)/B + \phi]$. Finite temperature convolves it with $-f'(E)$. Linearize $F(E) = F(\mu) + (m_c/e\hbar)(E - \mu)$, set $x = (E - \mu)/(k_B T)$, and integrate $[4\cosh^2(x/2)]^{-1}\cos(ax)$ to obtain

$$R_T = \frac{X_p}{\sinh X_p}, \qquad X_p = \frac{2\pi^2 p k_B T m_c}{e\hbar B} = 14.694\,p\frac{m_c}{m_e}\frac{T[\mathrm{K}]}{B[\mathrm{T}]}. \tag{6.6}$$

This allows an independent mass measurement from temperature-dependent amplitudes. For T3 at $B = 2\,\mathrm{T}$ and $T = 4\,\mathrm{K}$, $X_1 = 0.603$ and $R_T \simeq 0.942$. At $20\,\mathrm{K}$, $X_1 = 3.015$ and $R_T \simeq 0.296$. Fits to FFT amplitudes over a broad field window depend on the window function and effective field. Data at different temperatures require consistent background processing. Overlapping frequencies can invalidate a one-mass fit.

The density-dependent cyclotron mass of graphene connects thermal-damping measurements to a Dirac dispersion (Fig. 6.1).

Cyclotron mass is inferred from the temperature dependence of the amplitude of a fixed orbit. With a fixed field window, fit inset (c) using $R_T = X/\sinh X$ and $X = 2\pi^2 k_B T m_c/(e\hbar B)$. A larger mass produces stronger thermal damping. Then compare masses extracted at different gate voltages with the carrier density. For a fourfold-degenerate isotropic Dirac band, $k_F = \sqrt{\pi|n|}$ and $m_c = \hbar k_F/v_F$. The square-root trend therefore tests a linear dispersion against a parabolic model with density-independent mass.

Massless in this context refers to the vanishing Dirac rest-mass parameter; it does not imply vanishing cyclotron mass at finite Fermi energy. Background subtraction, the field window and temperature-dependent scattering enter the extraction. Near charge neutrality, charge inhomogeneity, broadening and the small number of occupied Landau levels limit a single LK fit. The endpoint of the smooth theoretical line at $n = 0$ is not an independent measurement of zero mass.

6.5 Dingle damping and spin zeros

For Lorentz-broadened Landau levels with $\Gamma = \hbar/(2\tau_q)$, convolution with the spectral function gives

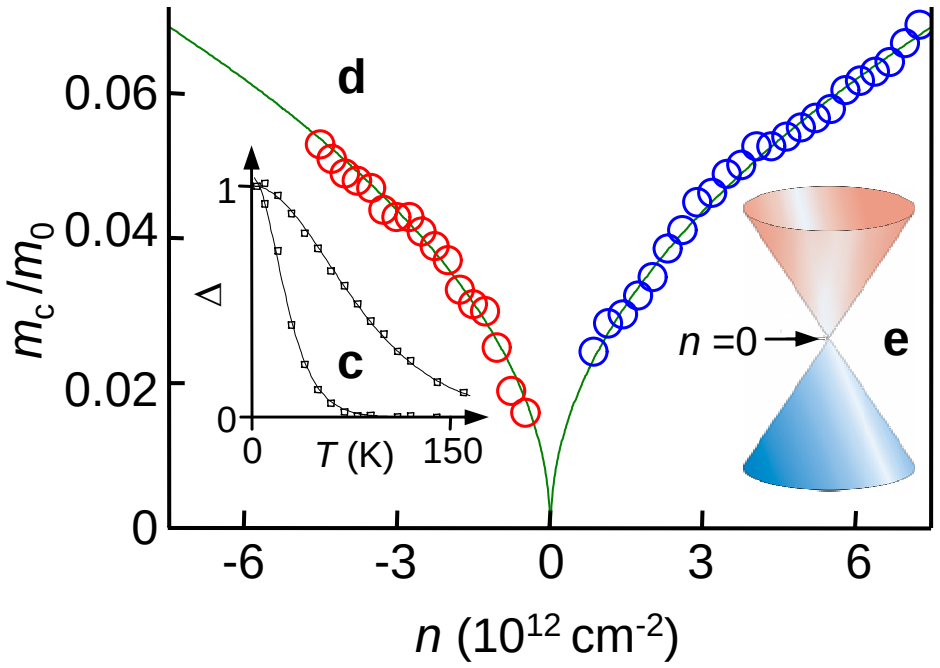

Figure 6.1: Graphene cyclotron masses and their thermal extraction, Fig. 3(c)–(e) of Novoselov et al. Circles in (d) are experimental hole and electron masses, with the authors' theoretical fit shown as a solid line. Inset (c) shows oscillation amplitudes and thermal-damping fits; (e) is a band schematic inferred from experiment and theory. Here m_0 is the free-electron mass.[56]

$$R_D = \exp\left[-\frac{\pi p}{\omega_c \tau_q}\right] = \exp\left[-\frac{2\pi^2 p k_B T_D m_c}{e\hbar B}\right], \quad T_D = \frac{\hbar}{2\pi k_B \tau_q}. \qquad R_s = \cos\left(\frac{\pi p g^* m_c}{2m_e}\right). \tag{6.7}$$

The spin factor sums two components with a relative Zeeman phase. For a tilted two-dimensional orbit, orbital quantization uses $B_\perp$ while Zeeman splitting often uses the total field, adding an angular factor. A sign reversal of R_s shifts the oscillation phase by π without any change in Berry phase. In the short-range T6 model, $\tau_q = 0.05833\,\mathrm{ps}$. At $B = 2\,\mathrm{T}$, graphene T3 has $\omega_c\tau_q = 1$ and $R_D = e^{-\pi} = 0.0432$, much smaller than its thermal damping factor. High mobility and strong oscillations are not synonymous.

6.6 Fermi-surface geometry and angular quantum oscillations

6.6.1 Worked example T12 Distinguishing a two-dimensional cylinder from an ellipsoid

An ideal two-dimensional sheet or infinite cylinder gives $F(\theta) = F(0)/|\cos\theta|$. For a rotational ellipsoid $(k_x^2 + k_y^2)/a^2 + k_z^2/c^2 = 1$, the central cross-sectional area gives

$$\frac{F(\theta)}{F(0)} = \frac{c}{\sqrt{a^2\sin^2\theta + c^2\cos^2\theta}} = \left[\cos^2\theta + \frac{a^2}{c^2}\sin^2\theta\right]^{-1/2}. \tag{6.8}$$

For $c/a = 3$, the ratio at $60°$ is $\sqrt{3} = 1.732$, versus 2 for the two-dimensional model. At $90°$ the ellipsoid reaches a finite value 3, while the ideal sheet expression diverges. Finite thickness, warping, magnetic breakdown and limited fields constrain actual observations. An approximate $1/\cos\theta$ dependence over a narrow angular interval does not uniquely establish a surface state.

6.7 Landau-fan phases and topological inference

The ideal fixed-μ model gives $N = F/B - \gamma$, but measured extrema may belong to ρ_{xx} rather than level crossings. Linearizing $\rho_{xx} = \sigma_d/(\sigma_d^2 + \sigma_H^2)$ gives

$$\delta\rho_{xx} = \frac{\sigma_H^2 - \sigma_d^2}{(\sigma_d^2 + \sigma_H^2)^2}\delta\sigma_d - \frac{2\sigma_d\sigma_H}{(\sigma_d^2 + \sigma_H^2)^2}\delta\sigma_H. \tag{6.9}$$

The first coefficient can change sign with the Hall angle, and the second need not be small. Relabelling maxima as half-integers moves the intercept by $1/2$ without changing any measured point. An oscillating $\mu(B)$ at fixed density, three-dimensional stationary phase, Zeeman splitting, spin zeros, orbital moments and unresolved frequencies also affect the phase. Report the measured tensor component, index rule, fit window and competing explanations.

6.8 The graphene zero Landau level and Hall sequence

With $\boldsymbol{\pi} = \mathbf{p} + e\mathbf{A}$ and $a = \ell_B(\pi_x - i\pi_y)/(\sqrt{2}\hbar)$, $[a, a^\dagger] = 1$. A single-valley Dirac Hamiltonian is

$$H = \frac{\sqrt{2}\hbar v_F}{\ell_B}\begin{pmatrix} 0 & a \\ a^\dagger & 0 \end{pmatrix}, \qquad E_N = \mathrm{sgn}(N)v_F\sqrt{2e\hbar B|N|}, \quad N \in \mathbb{Z}. \tag{6.10}$$

Squaring the Hamiltonian gives oscillator number operators, while one sublattice component supports an unpaired zero mode. Without resolved spin-valley splitting, each level has degeneracy $4eB/h$. At neutrality the zero level is half filled. Adding electrons first fills its remaining half and then whole higher levels, giving $\nu = 2, 6, 10, \ldots$. The physical charge Hall conductance is still an integer multiple of e^2/h, not an independently measurable half channel.

6.8.1 Worked example T13 Fixed density changes the quantum-limit criterion

At the T3 density, orbital bending starts near $1/u = 1\,\mathrm{T}$. Equating $E_1(B)$ to the zero-field E_F gives $10.34\,\mathrm{T}$. But accommodating all added electrons in the zero level at fixed density requires $n < 2eB/h$, giving $20.68\,\mathrm{T}$. Only the unfilled half of the zero level is available relative to neutrality. Temperature, broadening, a mass term and spin-valley symmetry breaking modify this ideal count.

6.9 Hall plateaux, localization and contacts

A clean spectrum supplies level positions and degeneracies but does not create finite-width Hall plateaux. Localized states in broadened levels can store particles without supporting dissipative transport across the sample, allowing density to change within a mobility gap while the Hall index remains fixed. In the edge picture, chiral channels propagate in one direction on each side; ideal voltage probes on the same edge read equal potentials. For electrons, $\sigma_{yx} = \nu e^2/h$ and $\sigma_{xx} \to 0$ imply $\rho_{yx} = -h/(\nu e^2)$ and $\rho_{xx} \to 0$. The $\nu = 2, 6$ plateau magnitudes are 12.906 and $4.302\,\mathrm{k\Omega}$. A Drude Hall line passing through these values is not a plateau mechanism.

Hall plateaux and longitudinal-resistance minima together reveal the transport signature of Landau quantization in graphene (Fig. 6.2).

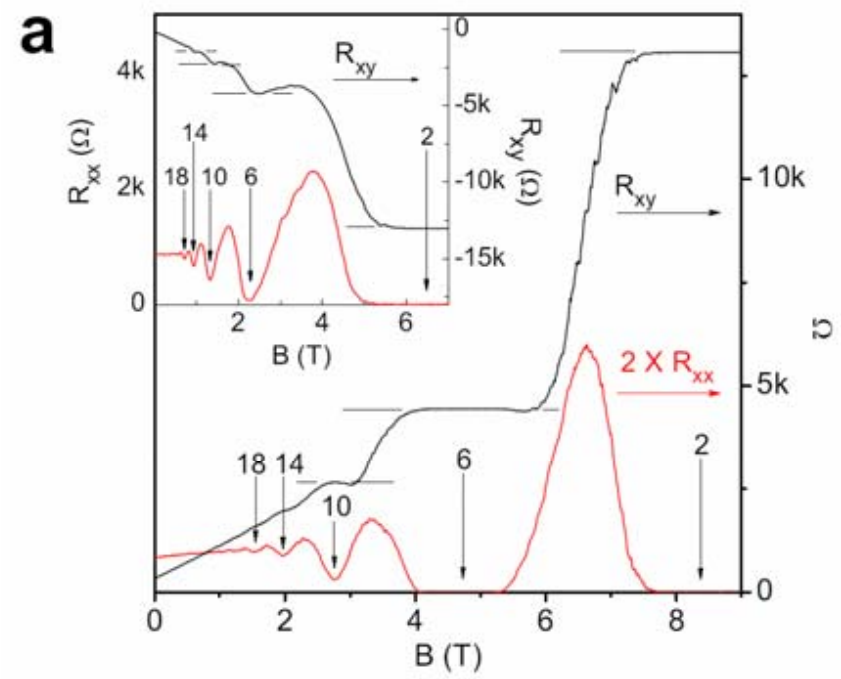

Figure 6.2: Quantum Hall transport in graphene, Fig. 2a of Zhang et al. Black traces show R_{xy}; the red main-panel trace is $2R_{xx}$, while the inset uses its labelled R_{xx} axis. The main panel is electron doped ($V_g = 15\,\mathrm{V}$, $T = 30\,\mathrm{mK}$), and the inset is hole doped ($V_g = -4\,\mathrm{V}$, $T = 1.6\,\mathrm{K}$). Arrows identify filling factors and grey reference lines indicate $h/(\nu e^2)$. Resistance signs follow the source contact convention.[58]

Follow a Hall plateau and a longitudinal-resistance minimum together. With unresolved spin and valley splitting, monolayer graphene has the sequence $\nu = \pm 2, \pm 6, \pm 10, \ldots$. Plateaux at $R_{xy} = h/(\nu e^2)$ and the accompanying low R_{xx} cannot be described by a smooth Drude line. Carrier type changes between the main panel and the inset, reversing the Hall signal. The displayed signs nevertheless retain the authors' lead and field conventions; they must be transformed before comparison with a differently defined σ_{xy}.

Conversion from measured resistances to two-dimensional resistivity and then conductivity requires geometry and tensor inversion. Away from a plateau, where R_{xx} is finite, Hall conductivity cannot generally be replaced by $1/R_{xy}$. Use $n = \nu eB/h$ to compare densities inferred from several plateaux and check them against the gate calibration. The figure establishes experimental plateaux and their sequence. Landau-level calculations explain the spectrum, while finite plateau widths additionally involve localization and boundary transport.

6.10 Thermoelectric response in the Weyl quantum limit

6.10.1 Worked example T14 Thermoelectric scale in the Weyl quantum limit

The lowest Landau branch of one Weyl node disperses linearly in one direction along the field and has areal degeneracy $e|B|/h$. A pair of opposite nodes with common speed v has the quantum-limit density of states

$$\nu_B = \frac{e|B|}{2\pi^2\hbar^2 v}, \qquad \mu = \frac{n}{\nu_B}, \qquad s = \frac{\pi^2}{3} k_B^2 T \nu_B. \qquad |\alpha_{xy}| = \frac{s}{|B|} = \frac{e k_B^2 T}{6\hbar^2 v}. \tag{6.11}$$

Here n is the net density relative to neutrality and s is entropy density. Strong-field drift transports entropy transversely, giving $|\alpha_{xy}| = s/|B|$. With Hall-dominated response, open electrical leads and the appropriate thermal boundaries, $|S_{xx}| \simeq s/(e|n|) = \pi^2 k_B^2 T/(3e|\mu|)$. At fixed n, $\mu \propto 1/B$, so the ideal-model thermopower increases with field[22]. For $v = 10^5\,\mathrm{m/s}$, $n = 10^{22}\,\mathrm{m^{-3}}$ and $B = 10\,\mathrm{T}$, $\mu \simeq 0.855\,\mathrm{meV}$. At $T = 1\,\mathrm{K}$, $|S| \simeq 28.6\,\mu\mathrm{V/K}$. The low-temperature estimate is plausible because $k_B T \ll \mu$. At higher temperature, calculate number and entropy directly and check occupation of higher Landau branches. For a multipocket material such as TaP, reconstruct $\sigma = \rho^{-1}$ and $\alpha = \sigma S$ from measured tensors. A large Seebeck coefficient alone does not establish a single-node quantum limit. Other pockets, phonon heat flow and magnetic thermal boundaries can all modify the result[23].

The large magnetothermoelectric response of TaP provides an application of quantum-limit transport in a multipocket material (Fig. 6.3).

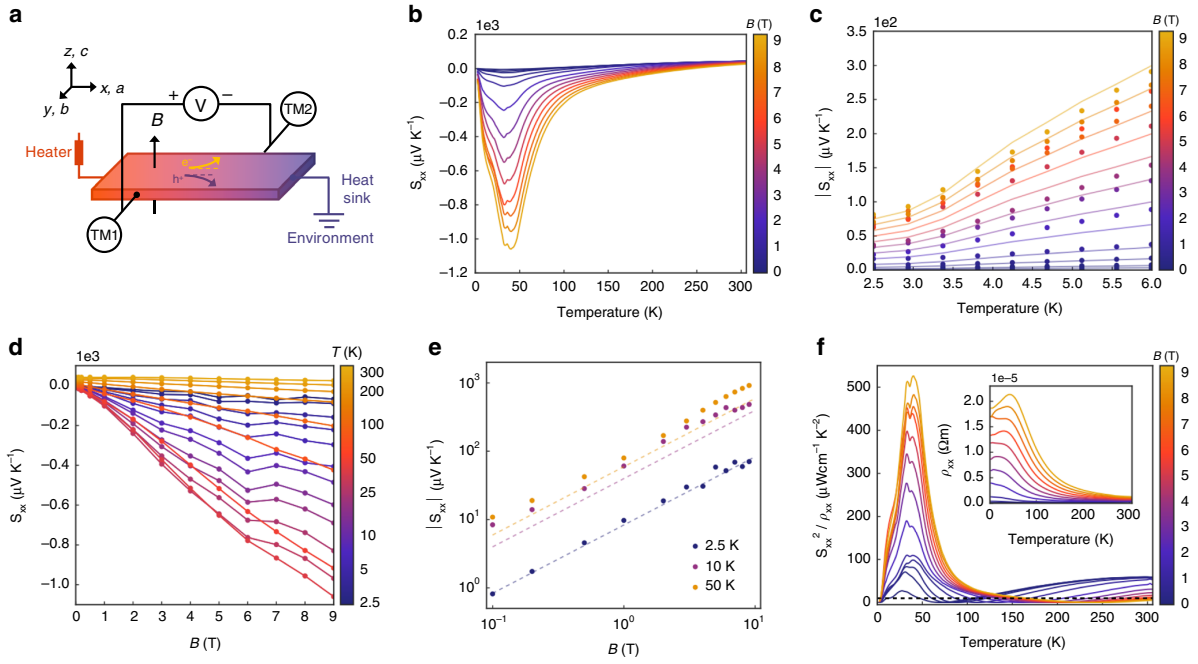

Figure 6.3: Magnetothermoelectric transport in TaP, Fig. 2 of Han et al. (CC BY 4.0). (a) Measurement geometry. (b,c) Temperature dependence of the longitudinal Seebeck coefficient and its magnitude. (d,e) Field dependence; dashed curves in (e) are the authors' fits with separate parameters. (f) Longitudinal power factor S_{xx}^2/ρ_{xx}, with resistivity in the inset. The plotted S_{xx} is negative; the large thermopower refers to its magnitude.[23]

The experiment reports $|S_{xx}| \simeq 1070\,\mu\mathrm{V/K}$ at 9 T and 40 K. To relate this large voltage to entropy transport in the quantum limit, first reconstruct $\alpha = \rho^{-1} S$ from electrical and thermoelectric tensors measured with the same field orientation and thermal boundary conditions. Both longitudinal and transverse tensor components contribute to the measured S_{xx}. A large magnetothermopower alone therefore neither excludes an ordinary compensated multiband response nor establishes a quantum-limit plateau of the thermoelectric Hall coefficient.

Next determine the Landau-level occupancy of each pocket from oscillation frequencies and cyclotron masses. Different Weyl pockets in TaP do not all reach their zeroth-level regime at the same field. When comparing low-temperature $|\alpha_{xy}|/T$ with its inverse-velocity scaling, distinguish an independently known band velocity from a thermoelectrically fitted parameter. Finally, power factor S_{xx}^2/ρ_{xx} is not a device

figure of merit: thermal conductivity, contacts and boundary conditions remain necessary for evaluating performance.

6.11 Exercises and solution notes

1. Fourier-transform a synthetic $\cos(2\pi F/B)$ using grids uniform in B and in $1/B$. Solution: the physical frequency is defined in $1/B$; an FFT directly on a uniform-B grid does not recover a fixed Onsager frequency.

2. Generate three temperature amplitudes from Eq. (6.6) and infer the mass. Add a nearby frequency and examine when a one-mass fit becomes unstable. Label generated traces as model data.

3. In the magnetic CrSb example M16, convert two frequencies into areas and compare the mass ratio with $\sqrt{F_1/F_2}$. Agreement tests a similar-orbit assumption; it does not directly measure exchange splitting at every momentum.

Chapter 7

Quantum response and transport through finite devices

7.1 Quantum coherence and interband response

Boltzmann theory follows approximately independent band occupations. It suits diffusive quasiparticles when interference does not control the result. Interband optical absorption needs off-diagonal density-matrix elements; a coherent short device needs contacts and transmission; weak localization needs interference of path amplitudes; topological boundary transport needs boundary conditions. These effects involve different quantum correlations and cannot be represented simply by shortening τ. The sensitivity of a measurement to occupation, coherence, spectrum or contacts determines the appropriate theoretical framework.

7.2 Density-matrix linear response and the Kubo formula

Let $H(t) = H_0 - F(t)B$. The interaction-picture density matrix obeys $i\hbar\dot{\rho}_I = [H'_I, \rho_I]$. Keeping one power of the perturbation and substituting into $\delta\langle A\rangle = \mathrm{Tr}(\delta\rho A)$ gives a causal commutator response. For an electromagnetic vector potential, paramagnetic current and the diamagnetic term must both be retained. Define the retarded current correlation per volume,

$$\chi^R_{ij}(t) = -\frac{i}{\hbar V}\theta(t)\langle[J^p_i(t), J^p_j(0)]\rangle, \qquad \sigma_{ij}(\omega) = \frac{i}{\omega + i0^+}[D_{ij} + \chi^R_{ij}(\omega)]. \tag{7.1}$$

For a continuum parabola, $D_{ij} = ne^2\delta_{ij}/m$; on a lattice, obtain it from Peierls coupling or $\partial_{k_i}\partial_{k_j}H$. In a normal state, a static uniform pure-gauge vector potential must not generate a physical equilibrium current. Cancellation between the correlation and diamagnetic terms checks gauge consistency[24]. Superfluid stiffness and the order of limits require separate treatment in a superconductor. Expanding the independent-electron commutator in eigenstates gives a Lehmann representation. The dissipative interband part at positive frequency is

$$\mathrm{Re}\,\sigma_{xx}(\omega) = \frac{\pi e^2}{\omega V}\sum_{n,m}(f_n - f_m)|\langle n|v_x|m\rangle|^2\delta(\epsilon_m - \epsilon_n - \hbar\omega). \tag{7.2}$$

In a periodic system, the sum per volume becomes a Brillouin-zone integral and a band sum. Occupation differences select allowed transitions, velocity matrix elements give selection rules, and the delta function enforces energy conservation. Numerical broadening η is only a replacement for the delta function unless a self-energy model gives it a physical interpretation; it is not automatically a transport scattering rate.

7.2.1 Worked example T15 Universal graphene interband conductivity

For $H = \hbar v(k_x\sigma_x + k_y\sigma_y)$, $v_x = v\sigma_x$, and the interband matrix-element magnitude is $v^2 \sin^2\phi$. At $T = 0$ with $\hbar\omega > 2|\mu|$, the allowed occupied-to-empty transitions satisfy $2\hbar vk = \hbar\omega$. The angular integral is π, the radial integral is $\omega/(4\hbar v^2)$, and spin-valley degeneracy contributes 4. Substitution gives

$$\mathrm{Re}\,\sigma_{2D}^{\mathrm{inter}}(\omega) = \frac{e^2}{4\hbar}\Theta(\hbar\omega - 2|\mu|). \qquad \mathcal{A} \simeq \pi\alpha_{\mathrm{fs}} \simeq 2.29\% \tag{7.3}$$

The second expression is the weak-absorption, normal-incidence limit for a suspended sheet. A substrate changes the optical boundary conditions. Cancellation of v reflects the combination of matrix element and transition-state density, not a universal total conductivity for every Dirac material. Mass, layer number, degeneracy and interactions can alter the result. At T3's $\mu = 116.67$ meV, Pauli blocking ends at 233.34 meV, or about 56.42 THz. Doping also produces a low-frequency Drude weight[25].

7.3 Connecting intrinsic DC Hall response to band geometry

The antisymmetric interband Kubo response contains $(f_n - f_m)\,\mathrm{Im}(v^x_{nm}v^y_{mn})/(\epsilon_n - \epsilon_m)^2$. Differentiating the nondegenerate eigenvalue equation gives

$$\langle u_m|\partial_{k_i}u_n\rangle = \frac{\langle u_m|\partial_{k_i}H|u_n\rangle}{\epsilon_n - \epsilon_m}, \quad m \neq n, \qquad \Omega_{n,z} = -2\,\mathrm{Im}\sum_{m\neq n}\frac{\langle n|\partial_{k_x}H|m\rangle\langle m|\partial_{k_y}H|n\rangle}{(\epsilon_n - \epsilon_m)^2}. \tag{7.4}$$

Substitution recovers $\sigma_{xy} = -(e^2/\hbar)\sum_n \int f_n\Omega_{n,z}[\mathrm{d}k]$. Wave-packet and Kubo results thus agree in their shared adiabatic, linear, clean intrinsic limit. Near a degenerate occupied subspace, the single-band denominator expression is unstable; use a non-Abelian projector or an invariant of the complete occupied subspace.

7.4 Spin and orbital Hall response and observables

Replacing one current vertex by $J_i^{s_a} = \{v_i, s_a\}/2$ defines a conventional spin-current response. When $[H, s_a] \neq 0$, the continuity equation contains a spin torque, and the bulk current is not a unique directly measured conserved flux. Edge spin accumulation also depends on diffusion, torques, boundaries and detection. Orbital current $J_i^{L_a} = \{v_i, L_a\}/2$ raises similar issues, including the choice of local orbital basis. A quantum spin Hall insulator is a band-topological phase; it is not equivalent to a large nonquantized spin Hall coefficient in an arbitrary metal.

Spin accumulation at opposite channel edges can be detected through a local magneto-optical signal (Fig. 7.1).

The ordinate is an optical Kerr rotation, probing local out-of-plane spin polarization rather than a transverse charge Hall voltage. A driven channel develops opposite spin accumulations at its two edges. The in-plane field B_{ext} rotates these spins and reduces their optically detected component. A single-relaxation-time approximation gives the Hanle form $A(B) = A(0)/[1 + (g\mu_B B\tau_s/\hbar)^2]$, with half-width $|B_{1/2}| = \hbar/(|g|\mu_B\tau_s)$. The width constrains a spin lifetime, subject to the appropriate diffusion and boundary model.

The sign reversal between edges is the crucial spatial evidence. The peak height cannot be identified directly with a bulk spin Hall conductivity without calibration. Connecting a calculated bulk current to this

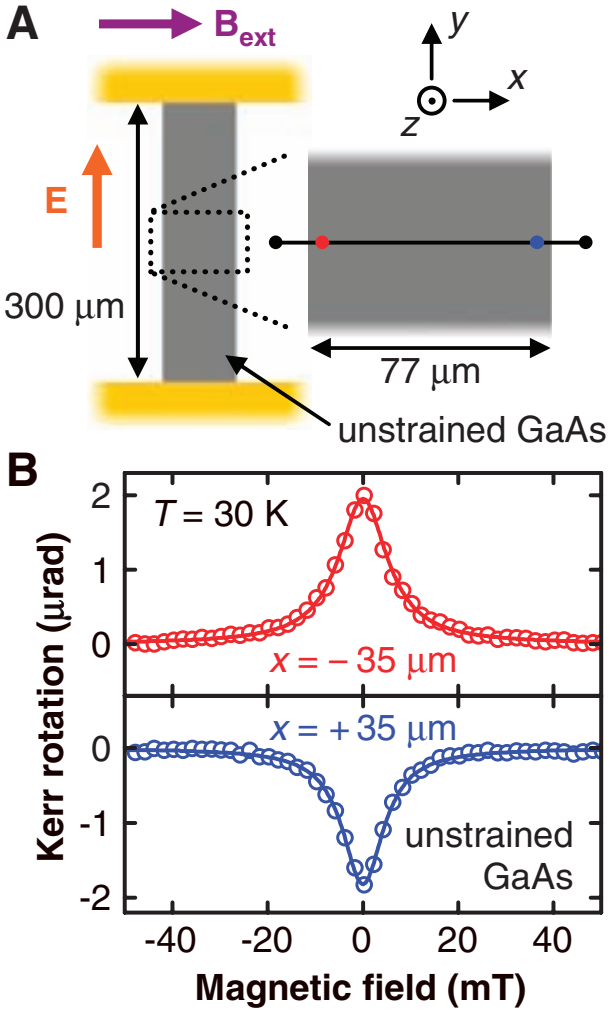

Figure 7.1: Magneto-optical detection of spin Hall accumulation in GaAs, Fig. 1A,B of Kato et al. (A) Unstrained GaAs channel and measurement geometry. (B) Kerr rotation versus in-plane magnetic field at $x = \pm 35\,\mu$m, for $T = 30\,$K and an electric-field amplitude of $10\,\mathrm{mV}/\mu$m. Circles are measurements and solid curves are Lorentzian fits. The two channel edges have opposite signs.[59]

measurement requires spin diffusion, boundary accumulation and optical conversion. The in-plane field used to detect precession has a different role from the perpendicular Lorentz field producing an ordinary charge Hall voltage. Both spin and orbital Hall calculations therefore need a stated angular-momentum current operator and a detector model in addition to a bulk response curve.

7.5 Incident-state flux and the Landauer formula

One one-dimensional propagating branch has density of states $L(\mathrm{d}k/\mathrm{d}E)/(2\pi)$ and crosses a section at rate v/L. Their product is exactly $1/h$. The occupation difference between two reservoirs therefore gives

$$I = \frac{e}{h}\int \mathrm{d}E\, \mathcal{T}(E)[f_L(E) - f_R(E)], \tag{7.5}$$

$$G = \frac{e^2}{h}\int \mathrm{d}E\, \mathcal{T}(E)(-\partial_E f), \qquad G(T=0) = \frac{e^2}{h}\sum_a T_a(E_F). \tag{7.6}$$

If the channel sum already includes spin, do not multiply it by two again. Write $2e^2/h$ only when two degenerate spins have been left out of the channel count. A perfectly transmitting device still has finite two-terminal contact resistance; it is not ordinary length-dependent Joule resistance generated in the channel interior. In a multiterminal measurement, each voltage probe is a reservoir with zero net current and its potential must be solved with the other terminals[26].

7.5.1 Worked example T16 A resonant level and asymmetric contacts

A level ϵ_0 couples to left and right reservoirs. In the wide-band approximation, $\Sigma_\alpha^r = -i\Gamma_\alpha/2$, giving

$$G^r(E) = \frac{1}{E - \epsilon_0 + i(\Gamma_L + \Gamma_R)/2}, \qquad \mathcal{T}(E) = \frac{\Gamma_L\Gamma_R}{(E-\epsilon_0)^2 + (\Gamma_L+\Gamma_R)^2/4}. \tag{7.7}$$

For $\Gamma_L = \Gamma_R = 10\,\mathrm{meV}$, resonance gives $\mathcal{T} = 1$; at $E_F - \epsilon_0 = 30\,\mathrm{meV}$, $\mathcal{T} = 0.1$. With spin degeneracy, the conductances are 77.48 and $7.748\,\mu\mathrm{S}$. Changing the contacts to $\Gamma_L = 5$, $\Gamma_R = 15\,\mathrm{meV}$ preserves total width but lowers peak transmission to $4\Gamma_L\Gamma_R/(\Gamma_L+\Gamma_R)^2 = 0.75$. The same spectral width does not uniquely determine conductance; contact symmetry is another input.

7.6 A Green-function algorithm for a finite tight-binding device

Separate the central device from semi-infinite leads and calculate each surface Green function g_α^r. The device self-energy is $\Sigma_\alpha^r = V_{C\alpha} g_\alpha^r V_{\alpha C}$. Then

$$G^r = [(E + i0^+)I - H_C - \Sigma_L^r - \Sigma_R^r]^{-1}, \quad \Gamma_\alpha = i(\Sigma_\alpha^r - \Sigma_\alpha^a), \quad \mathcal{T} = \mathrm{Tr}[\Gamma_L G^r \Gamma_R G^a]. \tag{7.8}$$

A homogeneous nearest-neighbour one-dimensional chain with identical device and lead hoppings has $T = 1$ per channel inside the band. Outside the band there are no propagating channels, so $T = 0$. This analytic limit tests the consistency of the lead self-energies and transmission calculation. An overly large numerical η simulates additional absorption; reduce it until results stabilize. An absorbing self-energy without a matching particle source can violate current conservation and is not automatically a physical dephasing model.

7.6.1 Worked example T17 Pseudodiffusive noise of neutral graphene

Consider a wide, short, neutral Dirac strip connected to ideal heavily doped leads. For specified boundaries giving transverse momenta $q_n = (n+1/2)\pi/W$, $n = 0, 1, 2, \ldots$, the strip modes at neutrality are evanescent. Matching gives $T_n = \mathrm{sech}^2(q_n L)$. In the limit $W \gg L$, replace the sum by an integral:

$$G \simeq \frac{4e^2}{\pi h}\frac{W}{L}, \qquad F_{\mathrm{noise}} = \frac{\sum_n T_n(1-T_n)}{\sum_n T_n} \to \frac{\int_0^\infty (\mathrm{sech}^2 x - \mathrm{sech}^4 x)\mathrm{d}x}{\int_0^\infty \mathrm{sech}^2 x\,\mathrm{d}x} = \frac{1}{3}. \tag{7.9}$$

The integrals $\int_0^\infty \mathrm{sech}^2 x\,\mathrm{d}x = 1$ and $\int_0^\infty \mathrm{sech}^4 x\,\mathrm{d}x = 2/3$ give the one-third noise ratio. It matches a diffusive metal even though this model contains no bulk disorder, hence the term pseudodiffusive[27]. For $W/L = 10$, the wide-strip limit gives $G \simeq 493.2\,\mu\mathrm{S}$. Edge termination, contact doping and aspect ratio change finite-size results. Neutrality-point minimum conductivity is not an unconditional constant across devices.

7.7 Coherent corrections and weak-localization scales

A scattered path interferes with its time-reversed counterpart on returning to its origin, potentially enhancing return probability and reducing diffusive conductance. Magnetic flux dephases the paired paths and produces a low-field magnetoconductance cusp. Spin-orbit coupling and Berry phases can change the interference sign. In two dimensions, $L_\phi = \sqrt{D\tau_\phi}$ and $B_\phi = \hbar/(4eD\tau_\phi)$. For $D = 0.02\,\mathrm{m}^2/\mathrm{s}$ and $\tau_\phi = 1\,\mathrm{ns}$, $L_\phi = 4.47\,\mu\mathrm{m}$ and $B_\phi = 8.23\,\mu\mathrm{T}$. Graphene additionally needs intervalley and intravalley scattering scales; a generic one-component metal fit need not apply. The perturbative correction assumes a diffusive reference state with $k_F\ell \gg 1$ and the appropriate dimensional regime. Strong localization, substantial interactions or superconducting fluctuations may lie outside it. τ_ϕ is neither the Dingle lifetime nor the Drude lifetime.

7.8 Analytic limits and numerical convergence

Hermiticity and state counting provide the first consistency conditions for a numerical response calculation. Parabolic Drude transport, an integer lattice Chern number and unit transmission in a matched chain provide analytic benchmarks. Different observables must also remain consistent with the same parameter set. Convert electronvolts explicitly when lengths and electromagnetic quantities use SI. With dimensionless momentum $q = ka$, velocity is $(a/\hbar)\partial_q H$, and curvature must be multiplied by a^2 to obtain physical momentum-space units. Convergence involves momentum grids, energy grids, broadening, device size and boundaries, not just a visually smooth curve.

7.9 Exercises and solution notes

1. Calculate $G(T)$ for T16 at $k_BT \ll \Gamma$ and $k_BT \gg \Gamma$. Thermally average transmission with the Fermi window; do not replace Γ by $\Gamma + k_BT$.
2. Add a single-site potential V_0 to a matched chain and verify $T = 1/[1 + (V_0/(2t\sin k))^2]$. Near a band edge, the same potential reflects more strongly as velocity vanishes.
3. Compare the finite-mode T17 sum with its integral for $W/L = 1, 2, 5, 10$. Record boundary conditions and spin-valley counting so that a duplicated degeneracy factor does not quadruple conductance.

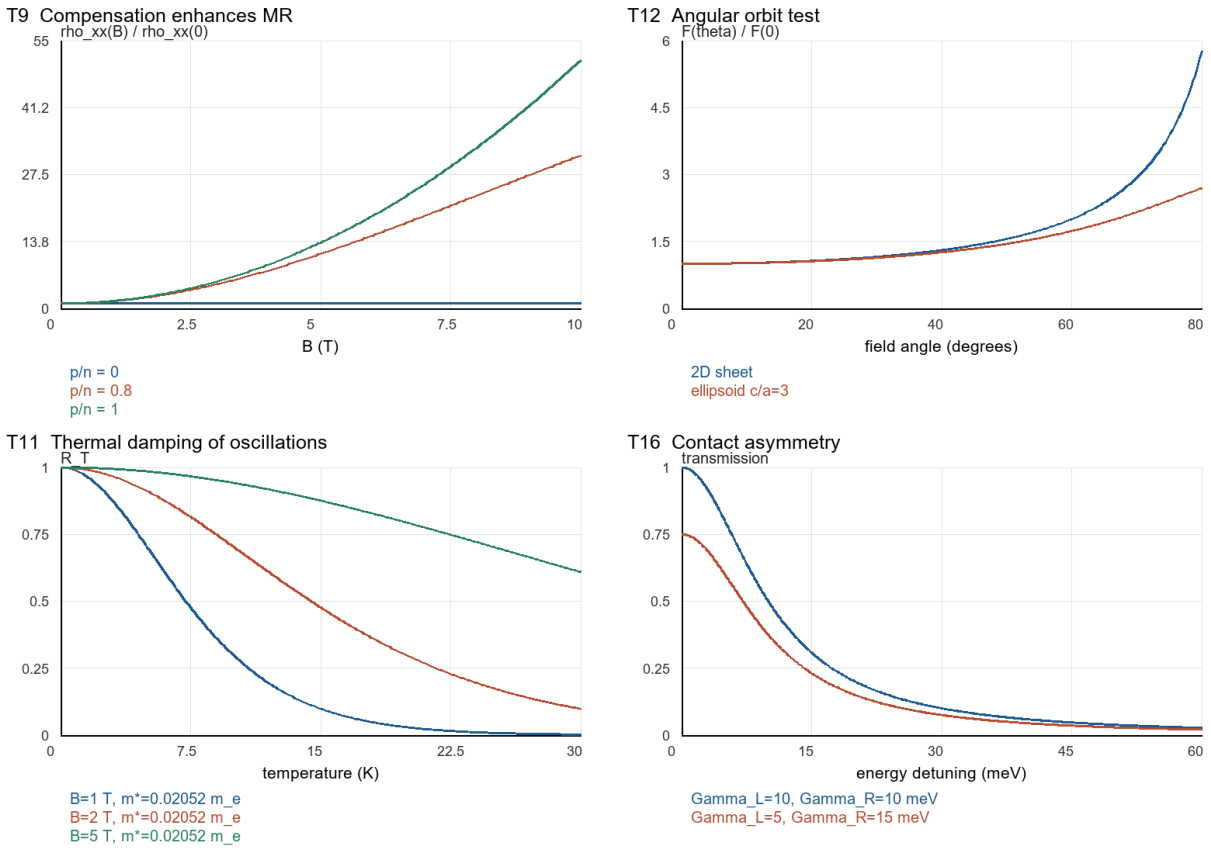

Figure 7.2: Model checks for T9, T12, T11 and T16. Two-carrier mobilities are $u_e = 1, u_h = 0.5\,\mathrm{m}^2/(\mathrm{Vs})$; angular maps compare a sheet with a $c/a = 3$ ellipsoid; thermal damping uses the T3 orbit mass; resonant-level curves keep the total contact width fixed. All curves are calculated.

Part IV

Magnetism

Chapter 8

Foundations of Magnetism and Mean-Field Theory

8.1 Atomic moments and metallic susceptibility

8.1.1 Susceptibility, magnetic order and conventions

Magnetism involves two connected levels of description. Electronic orbital and spin degrees of freedom determine microscopic moments, while statistics and interactions determine their field response and collective order. Susceptibility characterizes an induced response; magnetic ordering involves spontaneous symmetry breaking in zero field. The number of unpaired electrons is a useful clue to a local moment, but a quantitative description also requires energy levels, matrix elements, thermal populations and exchange interactions. Atomic response, exchange models, mean-field theory and spin waves provide a route between local-moment and itinerant-electron magnetism.

We use SI units, $e > 0$, electron charge $-e$, and $\mu_B = e\hbar/(2m_e)$. The operators $\mathbf{L}, \mathbf{S}, \mathbf{J}$ are dimensionless: their physical angular momenta contain an additional $\hbar$. For the material free-energy density f, write $M_\alpha = -\partial f/\partial B_\alpha$ and $\chi_{\alpha\beta} = \mu_0 \partial M_\alpha/\partial B_\beta$ in the weak-magnetization regime. This agrees with $\partial M/\partial H$ when $B \simeq \mu_0 H$. A ferromagnet additionally requires a treatment of the demagnetizing field and sample geometry. Volume susceptibility is dimensionless; molar susceptibility is measured in $\mathrm{m}^3/\mathrm{mol}$. Gaussian and SI units use different field and susceptibility conventions. Equations and experimental values must be converted consistently before comparison.

8.1.2 Minimal coupling and atomic magnetic response

For $\mathbf{B} = B\hat{z}$, choose $\mathbf{A} = \mathbf{B} \times \mathbf{r}/2$. Expanding $(\mathbf{p} + e\mathbf{A})^2/(2m_e)$ gives an orbital Zeeman term from the cross term and a diamagnetic term from A^2. The simplification uses $\nabla \cdot \mathbf{A} = 0$. Including spin gives

$$\delta H = \mu_B B(L_z + g_s S_z) + \frac{e^2 B^2}{8m_e} \sum_i (x_i^2 + y_i^2), \qquad g_s \simeq 2.0023, \tag{8.1}$$

$$\delta E_n = \langle n|\delta H|n\rangle + \sum_{r \neq n} \frac{|\langle r|\mu_B B(L_z + g_s S_z)|n\rangle|^2}{E_n - E_r} + O(B^3). \tag{8.2}$$

Three distinct mechanisms appear. First, splitting a degenerate ground multiplet changes thermal populations and produces Curie paramagnetism. Second, even a nondegenerate ground state acquires admixtures of excited states through off-diagonal matrix elements, producing Van Vleck paramagnetism. Third, the positive A^2 term raises the energy and produces Larmor diamagnetism. A time-reversal-invariant nondegenerate ground state has zero linear expectation value, but this does not imply zero susceptibility.

A closed shell has $L = S = J = 0$. For an isotropic atom, $\langle x_i^2 + y_i^2\rangle = 2\langle r_i^2\rangle/3$, giving

$$\chi_{\mathrm{L}} = -\frac{\mu_0 n_{\mathrm{ion}} e^2}{6 m_e} \sum_i \langle r_i^2 \rangle, \qquad \chi_{\mathrm{VV}} = 2\mu_0 n_{\mathrm{ion}} \mu_B^2 \sum_{r \neq 0} \frac{|\langle r|L_z + g_s S_z|0\rangle|^2}{E_r - E_0}. \tag{8.3}$$

Example M1 Van Vleck response of a nonmagnetic ground state

Consider a ground state and one excited state separated by $\Delta = 20\,\mathrm{meV}$, with $|\langle 1|\mu_z|0\rangle| = \mu_B$ and ion density $n = 10^{28}\,\mathrm{m}^{-3}$. Second-order perturbation theory gives an energy shift $-\mu_B^2 B^2/\Delta$, hence $\chi_{\mathrm{VV}} = 2\mu_0 n \mu_B^2/\Delta \simeq 6.75 \times 10^{-4}$. The response is approximately temperature independent when $k_B T \ll \Delta$. Doubling the excitation energy halves the susceptibility. This differs from the $1/T$ response of thermally oriented permanent moments.

The statement $J = 0$ alone therefore does not establish that only diamagnetism remains. The relevant question is whether the magnetic-moment operator connects the ground state to other multiplets. Crystal fields change both level separations and matrix elements, so free-ion results are a starting point rather than a complete theory of a solid.

8.1.3 Hund rules and effective moments

For a nearly isolated ion, Pauli exclusion and the first two Hund rules select the largest allowed S and the corresponding largest L. Spin-orbit coupling then splits this manifold into J multiplets. A less-than-half-filled shell usually selects $J = |L-S|$; a more-than-half-filled shell selects $J = L+S$. Coulomb interactions establish L, S first, and weaker SOC subsequently selects J. If SOC is set strictly to zero, selecting just one J multiplet is not justified. LS coupling is appropriate for some light-element ions, whereas strong crystal fields, strong SOC or mixed valence can require a different description.

Within one J multiplet, the projected moment is $\boldsymbol{\mu} = -g_J \mu_B \mathbf{J}$. Using $\mathbf{J} = \mathbf{L} + \mathbf{S}$ and $\mathbf{S} \cdot \mathbf{J} = [J(J+1) + S(S+1) - L(L+1)]/2$ gives

$$g_J = 1 + \frac{J(J+1) + S(S+1) - L(L+1)}{2J(J+1)}, \quad \mu_{\mathrm{eff}} = g_J \sqrt{J(J+1)}\,\mu_B, \quad \mu_{\mathrm{sat}} = g_J J \mu_B. \tag{8.4}$$

The effective moment is extracted from a high-temperature Curie constant; the saturation moment comes from low-temperature, high-field magnetization. Their inequality is not a contradiction. In many $3d$ ions, the crystal field quenches orbital angular momentum and a spin-only model with $g \simeq 2$ is a useful first approximation. More localized $4f$ electrons often retain a useful J-multiplet description.

Example M2 High-spin iron versus cerium

High-spin Fe^{3+} has a $3d^5$ configuration: five orbitals each hold one parallel spin. Thus $S = 5/2, L = 0, J = 5/2$, and the term is ${}^6S_{5/2}$. Consequently $g_J = 2$, $\mu_{\mathrm{eff}} = \sqrt{35}\mu_B = 5.916\mu_B$, whereas the saturation moment is $5\mu_B$. For Ce^{3+} with $4f^1$, $L = 3, S = 1/2, J = 5/2$ and $g_J = 6/7$. The effective moment is $2.535\mu_B$ and the saturation moment is $2.143\mu_B$. These free-ion estimates must not replace the low-temperature effective g tensor of a crystal-field ground doublet.

8.1.4 Deriving the Curie law from the partition function

Choose a magnetic-moment quantum number such that $E_m = -g_J\mu_B B m$. Summing a finite geometric series gives the partition function. With $y = \beta g_J \mu_B J B$, differentiation of $\ln Z$ yields the full magnetization curve.

$$Z = \sum_{m=-J}^{J} e^{\beta g_J \mu_B B m} = \frac{\sinh[(2J+1)y/(2J)]}{\sinh[y/(2J)]}, \tag{8.5}$$

$$M = n_{\text{ion}} g_J \mu_B J B_J(y), \tag{8.6}$$

$$B_J(y) = \frac{2J+1}{2J}\coth\!\left(\frac{2J+1}{2J}y\right) - \frac{1}{2J}\coth\!\left(\frac{y}{2J}\right), \tag{8.7}$$

$$B_J(y) = \frac{J+1}{3J}y + O(y^3), \qquad \chi = \frac{\mu_0 n_{\text{ion}}(g_J\mu_B)^2 J(J+1)}{3k_B T} = \frac{C}{T}. \tag{8.8}$$

For $J = 1/2$, $B_{1/2}(y) = \tanh y$. Linear response requires $g_J\mu_B JB \ll k_B T$; at lower temperature or higher field the complete function is needed. One mole of high-spin Fe^{3+} gives $C_{\text{mol}} = 5.500 \times 10^{-5}\,\text{m}^3\text{K/mol}$ and therefore $\chi_{\text{mol}} = 1.833 \times 10^{-7}\,\text{m}^3/\text{mol}$ at 300 K. Deviations from $1/T$ call for separate checks of exchange, thermal occupation of crystal-field states and temperature-independent backgrounds, rather than an arbitrary adjustment of g.

8.1.5 Pauli paramagnetism and Landau diamagnetism

Almost every local moment can reorient, but only electrons close to the Fermi surface can redistribute their occupations in a degenerate electron gas. Let $D(E)$ be the density of states per volume including both spins, and let μ be the chemical potential. Expanding the Zeeman shifts $\mp\mu_B B$ gives

$$n_\uparrow - n_\downarrow = \mu_B B \int D(E)[-f'(E)]\,\mathrm{d}E, \tag{8.9}$$

$$\chi_P(T) = \mu_0 \mu_B^2 \int D(E)[-f'(E)]\,\mathrm{d}E, \tag{8.10}$$

$$\chi_P(0) = \mu_0 \mu_B^2 D(E_F), \qquad D(E_F) = \frac{m^* k_F}{\pi^2 \hbar^2} = \frac{3n}{2E_F}. \tag{8.11}$$

For a smooth DOS, a Sommerfeld expansion is possible, but fixed particle number also requires the temperature shift of μ. A three-dimensional parabolic band gives $\chi_P(T) = \chi_P(0)[1 - \pi^2(k_B T/E_F)^2/12 + \cdots]$. Metallic spin susceptibility therefore often varies little around room temperature. Near a van Hove singularity the smooth-DOS assumption can fail.

The orbital response follows from Landau quantization. For a three-dimensional parabolic band without SOC, omit Zeeman splitting initially and write $E_{\ell k_z} = \hbar\omega_c(\ell + 1/2) + \hbar^2 k_z^2/(2m^*)$. The degeneracy per area per spin is $eB/(2\pi\hbar)$. Both spins must be included in the grand potential, without counting them again through an additional DOS factor:

$$\frac{\Omega}{V} = -2k_B T \frac{eB}{2\pi\hbar} \sum_{\ell=0}^{\infty} \int \frac{\mathrm{d}k_z}{2\pi} \ln\!\left[1 + e^{-\beta(E_{\ell k_z} - \mu)}\right]. \tag{8.12}$$

Insert $F(x) = \int \mathrm{d}k_z/(2\pi) \ln[1 + e^{-\beta(\hbar\omega_c x + \hbar^2 k_z^2/2m^* - \mu)}]$ into the midpoint Euler–Maclaurin formula $\sum_{\ell \geq 0} F(\ell + 1/2) = \int_0^\infty F(x)\mathrm{d}x + F'(0)/24 + \cdots$. The integral produces the zero-field background.

Since $F'(0) < 0$, the overall negative prefactor gives a positive B^2 correction and therefore a negative orbital susceptibility. The smooth part is

$$\chi_{\text{Landau}} = -\frac{\mu_0 e^2 k_F}{12\pi^2 m^*} = -\frac{1}{3}\left(\frac{m_e}{m^*}\right)^2 \chi_P \quad (g = 2). \tag{8.13}$$

This ratio is not universal for lattice bands. The effective mass controls orbital motion, while the Zeeman moment involves the effective g factor; multiband systems also have interband orbital terms. At low temperature and high field, the discrete sum produces de Haas–van Alphen oscillations, which are not captured by the smooth expansion.

Example M3 A free-electron estimate for copper

Take $n = 8.5 \times 10^{28}\,\text{m}^{-3}$, $E_F = 7.04936\,\text{eV}$ and $m^* = m_e$. Then $\chi_P = 1.2201 \times 10^{-5}$ and $\chi_{\text{Landau}} = -4.0670 \times 10^{-6}$, summing to 8.1340×10^{-6}. This is the response of a free valence-electron model. Comparing it with actual copper also requires core diamagnetism and realistic band contributions. Treating the estimate as the complete experimental susceptibility would exceed the model's scope.

8.2 Exchange interactions, mean fields and spin waves

8.2.1 From two-electron exchange to the Heisenberg model

The dipolar scale is $E_{\text{dip}} \sim \mu_0 \mu_B^2/(4\pi r^3)$. At $r = 0.3\,\text{nm}$ it is only about $2\,\mu\text{eV}$, corresponding to roughly $0.02\,\text{K}$. Dipolar interactions can matter for anisotropy, domains and long-wavelength dynamics, but cannot generally explain ordering temperatures of tens to thousands of kelvin. Larger magnetic energy scales originate from Coulomb interactions together with fermionic antisymmetry.

For electrons occupying two localized orbitals, the complete wavefunction must be antisymmetric. A spin singlet has a symmetric spatial wavefunction, whereas a spin triplet has an antisymmetric spatial wavefunction. Their different spatial correlations produce different Coulomb energies. Mapping the splitting onto $H = J_{\text{AF}}\mathbf{S}_1 \cdot \mathbf{S}_2$ gives $E_s = -3J_{\text{AF}}/4$ and $E_t = J_{\text{AF}}/4$. For the collective spin model, use the convention in which positive exchange favors ferromagnetic alignment:

$$H = -\sum_{\langle ij \rangle} J_{ij}\mathbf{S}_i \cdot \mathbf{S}_j - g\mu_B B \sum_i S_i^z, \qquad J_{ij} > 0 \text{ for ferromagnetic coupling.} \tag{8.14}$$

Each bond is counted once. A sum over all ordered pairs ij requires a factor $1/2$. Comparing the sign of J between papers without checking their Hamiltonian can interchange ferromagnetism and antiferromagnetism. Direct exchange, ligand-mediated superexchange and conduction-electron-mediated indirect exchange are different mechanisms. The Hubbard dimer below exposes the virtual-hopping origin of superexchange.

Example M4 Exact spectrum and superexchange of a Hubbard dimer

Consider two sites and two electrons with hopping t and on-site double-occupancy cost $U > 0$. A triplet cannot hop into a doubly occupied single orbital while conserving spin, and its energy is set to zero. The singlet couples to a symmetric doublon state through

$$H_{S=0} = \begin{pmatrix} 0 & -2t \\ -2t & U \end{pmatrix}, \quad E_s = \frac{U - \sqrt{U^2 + 16t^2}}{2}, \quad J_{\mathrm{AF}} = E_t - E_s \simeq \frac{4t^2}{U}. \tag{8.15}$$

For $t = 0.10\,\mathrm{eV}$ and $U = 2.0\,\mathrm{eV}$, the exact splitting is $19.804\,\mathrm{meV}$; second-order perturbation theory gives $20.000\,\mathrm{meV}$, an error of about 0.99%. Doubling t increases the leading exchange fourfold, but also increases t/U and the truncation error. The half-filled, strongly interacting single-band model favors antiferromagnetism. This does not imply that all materials do: multiorbital Hund coupling and bond geometry can change the result.

8.2.2 Deriving Weiss mean field and testing stability

Set $s = \langle S_i^z \rangle$ on equivalent sites. Decouple $S_i^z S_j^z \simeq s S_i^z + s S_j^z - s^2$ and take transverse averages to vanish. With nearest-neighbor coordination z, the effective energy field is $h = g\mu_B B + zJs$. The constant must be retained because it controls the free-energy extremum:

$$H_{\mathrm{MF}} = -h \sum_i S_i^z + \frac{NzJ}{2} s^2, \tag{8.16}$$

$$f_{\mathrm{MF}}(s) = \frac{zJ}{2} s^2 - k_B T \ln \sum_{m=-S}^{S} e^{\beta h m}, \tag{8.17}$$

$$s = S B_S(\beta S h), \qquad k_B T_C^{\mathrm{MF}} = \frac{zJS(S+1)}{3}. \tag{8.18}$$

Differentiating the free energy gives $\partial f / \partial s = zJ[s - \langle S^z \rangle_h]$, so stationarity is equivalent to self-consistency. However, a stationary point need not be stable: compare free energies and inspect the second derivative. At $B = 0$, $s = 0$ always solves the equation, but below T_C it becomes an unstable maximum. Spontaneous symmetry breaking requires taking the thermodynamic limit before removing a small field that selects a direction.

Linearization above T_C gives $\chi = C/(T - \Theta)$, with $\Theta = T_C^{\mathrm{MF}}$ for the nearest-neighbor ferromagnet. Competing exchanges invalidate the identification of Θ and the transition temperature. The former depends on $\sum_j J_{ij}$, whereas the ordering wavevector is selected by the largest eigenvalue of the exchange matrix or by the maximum of $J(\mathbf{q})$.

Example M5 Spontaneous magnetization and critical behavior

For $S = 1/2$, define $m = s/S$ and $t_r = T/T_C$. The zero-field equation is $m = \tanh(m/t_r)$. Bisection for the positive root gives

T/T_C	0.20	0.50	0.80	0.90	0.99	1.10
m	0.999909	0.957504	0.710412	0.525430	0.172511	0

Expanding $\tanh x = x - x^3/3 + \cdots$ gives $m^2 \simeq 3t_r^2(1 - t_r)$ and the mean-field exponent $\beta = 1/2$. Spatial correlations near a transition cause many three-dimensional systems to depart from this exponent; the mean-field curve describes an approximation that neglects those fluctuations. For $J = 1\,\mathrm{meV}$, $z = 6$ and $S = 1/2$, $T_C^{\mathrm{MF}} = 17.41\,\mathrm{K}$. Changing coordination at fixed J changes this temperature directly.

8.2.3 A two-sublattice antiferromagnet

Now use $H = J_{\mathrm{AF}} \sum_{\langle ij \rangle} \mathbf{S}_i \cdot \mathbf{S}_j$ with $J_{\mathrm{AF}} > 0$. For sublattice averages s_A, s_B,

$$s_A = S B_S[\beta S(g\mu_B B - z J_{\mathrm{AF}} s_B)], \tag{8.19}$$

$$s_B = S B_S[\beta S(g\mu_B B - z J_{\mathrm{AF}} s_A)], \tag{8.20}$$

$$k_B T_N^{\mathrm{MF}} = z J_{\mathrm{AF}} S(S+1)/3, \qquad \Theta = -T_N^{\mathrm{MF}}. \tag{8.21}$$

At zero field, $s_A = -s_B$: uniform magnetization vanishes while the staggered order parameter $\ell = (s_A - s_B)/2$ remains finite. A uniform field couples to $s_A + s_B$, giving $\chi = C/(T + T_N)$ above the transition. A staggered field couples to $s_A - s_B$, and its susceptibility diverges at T_N. Zero net magnetization therefore does not imply absence of order. Magnetic Bragg peaks in neutron scattering reveal the ordering wavevector even when a bulk moment measurement misses the order.

8.2.4 Ferromagnetic spin waves

For the ferromagnetic Heisenberg convention, the fully polarized state $|F\rangle$ is an exact ground state. A normalized one-flip state is $|j\rangle = (2S)^{-1/2} S_j^- |F\rangle$. Its plane-wave combination is $|\mathbf{q}\rangle = N^{-1/2} \sum_j e^{i\mathbf{q}\cdot\mathbf{R}_j} |j\rangle$. Exchange both costs local energy and propagates the spin flip to neighboring sites. Acting with the Hamiltonian gives

$$\varepsilon_{\mathbf{q}} = g\mu_B B + S[J(0) - J(\mathbf{q})], \qquad J(\mathbf{q}) = \sum_{\boldsymbol{\delta}} J_{\boldsymbol{\delta}} e^{i\mathbf{q}\cdot\boldsymbol{\delta}}, \tag{8.22}$$

$$\varepsilon_{\mathbf{q}}^{\mathrm{cubic}} = g\mu_B B + 2JS[3 - \cos(q_x a) - \cos(q_y a) - \cos(q_z a)] \tag{8.23}$$

$$\simeq g\mu_B B + JSa^2 q^2. \tag{8.24}$$

The magnon energy is $\varepsilon = \hbar\omega$. An energy in meV must not be read directly as a frequency in GHz. At low temperature in a three-dimensional zero-field ferromagnet, each dilute magnon reduces total S^z by one. Writing the stiffness as $\mathcal{D} = JSa^2$, the Bose integral gives

$$\frac{M(0) - M(T)}{g\mu_B} = \int \frac{\mathrm{d}^3 q}{(2\pi)^3} \frac{1}{e^{\mathcal{D}q^2/(k_B T)} - 1} = \frac{\zeta(3/2)}{8\pi^{3/2}} \left(\frac{k_B T}{\mathcal{D}} \right)^{3/2}. \tag{8.25}$$

This is Bloch's $T^{3/2}$ law. It assumes dilute, weakly interacting magnons, small wavevectors and no important gap, and must not be extrapolated into the critical region. An easy-axis gap Δ_a makes the response thermally activated at sufficiently low temperature.

Example M6 Inferring exchange from a dispersion

For a nearest-neighbor ferromagnetic chain, $\varepsilon_q = 2JS(1 - \cos qa)$. With $S = 1/2$ and $J = 10\,\mathrm{meV}$, the zone-boundary energy is $20\,\mathrm{meV}$. At $qa = 0.2$ the exact energy is $0.1993\,\mathrm{meV}$, while $JS(qa)^2$ gives $0.2000\,\mathrm{meV}$. A measured small-wavevector curvature determines only JSa^2. Separating J from S requires independent information such as a moment measurement.

8.2.5 Antiferromagnetic spin waves and the limits of mean field

For a bipartite antiferromagnet, rotate the B-sublattice spin axes by π before a Holstein–Primakoff expansion. The quadratic Hamiltonian contains $a_{\mathbf{q}}b_{-\mathbf{q}} + a_{\mathbf{q}}^{\dagger}b_{-\mathbf{q}}^{\dagger}$: the classical Néel product state is not an exact quantum ground state. A Bogoliubov transformation gives

$$\varepsilon_{\mathbf{q}} = zJ_{\mathrm{AF}}S\sqrt{1-\gamma_{\mathbf{q}}^2}, \qquad \gamma_{\mathbf{q}} = \frac{1}{z}\sum_{\boldsymbol{\delta}} e^{i\mathbf{q}\cdot\boldsymbol{\delta}}. \tag{8.26}$$

For the square lattice, $z = 4$ and $\gamma = (\cos q_x a + \cos q_y a)/2$, giving $\varepsilon_{\mathbf{q}} \simeq 2\sqrt{2}J_{\mathrm{AF}}Sa|\mathbf{q}|$. This is linear rather than quadratic. Quantum zero-point fluctuations reduce the staggered moment, and the exact one-dimensional $S = 1/2$ chain cannot be described by classical Néel order.

With short-range interactions, strictly one or two dimensions, and continuous spin-rotation symmetry, the Mermin–Wagner theorem excludes spontaneous breaking of that continuous symmetry at finite temperature[28]. The infrared divergence of two-dimensional spin-wave fluctuations reveals what mean field misses. A finite mean-field T_N is an approximate instability scale, not the actual ordering temperature of this ideal model. Interlayer coupling, anisotropy, long-range interactions or finite size alter the assumptions. The theorem does not say that every two-dimensional material is nonmagnetic.

8.3 Magnetic mean-field theory of the Hubbard model

8.3.1 Hartree–Fock decoupling and self-consistency

The single-band Hubbard model retains hopping and on-site repulsion. It connects weak-coupling instabilities of itinerant electrons to strong-coupling local-spin exchange, although Hartree–Fock cannot accurately describe all correlation effects in both regimes.

$$H = -\sum_{ij\sigma} t_{ij}c_{i\sigma}^{\dagger}c_{j\sigma} + U\sum_i n_{i\uparrow}n_{i\downarrow} - \mu\sum_i n_i. \tag{8.27}$$

First choose a collinear spin axis and define $\rho_i = \langle n_i\rangle$ and $m_i = \langle n_{i\uparrow} - n_{i\downarrow}\rangle/2$. Then $\langle n_{i\sigma}\rangle = \rho_i/2 + \sigma m_i$ for $\sigma = \pm 1$. Use $AB = \langle A\rangle B + A\langle B\rangle - \langle A\rangle\langle B\rangle + \delta A\delta B$ and neglect the correlated fluctuation term:

$$Un_{i\uparrow}n_{i\downarrow} \simeq U\sum_{\sigma}(\rho_i/2 - \sigma m_i)n_{i\sigma} - U(\rho_i^2/4 - m_i^2), \tag{8.28}$$

$$(h_\sigma)_{ij} = -t_{ij} + \delta_{ij}[U\rho_i/2 - \sigma U m_i - \mu], \tag{8.29}$$

$$\rho_i^{\mathrm{out}} = \sum_{a\sigma} |u_{a\sigma}(i)|^2 f(E_{a\sigma}), \tag{8.30}$$

$$m_i^{\mathrm{out}} = \frac{1}{2}\sum_{a\sigma} \sigma|u_{a\sigma}(i)|^2 f(E_{a\sigma}). \tag{8.31}$$

The exchange field is Um_i, not $2Um_i$; the latter is the separation between the two spin-diagonal energies. If instead the order parameter is defined as $\widetilde{m} = \langle n_\uparrow - n_\downarrow\rangle$, the field is $U\widetilde{m}/2$. Many apparent discrepancies are simply inconsistent conventions.

Noncollinear states also require the Fock terms involving $\langle c_{i\uparrow}^{\dagger}c_{i\downarrow}\rangle$. Defining $\mathbf{m}_i = \langle c_i^{\dagger}\boldsymbol{\sigma}c_i\rangle/2$, the single-particle potential is $U\rho_i\mathbf{1}/2 - U\mathbf{m}_i\cdot\boldsymbol{\sigma}$, with constant $-U(\rho_i^2/4 - |\mathbf{m}_i|^2)$. Searching only collinear states restricts the variational space and cannot rule out spiral or noncollinear ground states.

8.3.2 The Stoner criterion and density-of-states conventions

For a uniform ferromagnet, set $m_i = m$, $\rho_i = n$ and absorb the Hartree shift into the chemical potential. The spectrum is $\xi_{\mathbf{k}\sigma} = \varepsilon_{\mathbf{k}} - \mu_0 - \sigma U m$. Linearizing in small m, with $D_1(E_F)$ the single-spin DOS per site, gives

$$2m = 2UmD_1(E_F) + O(m^3), \qquad UD_1(E_F) > 1. \tag{8.32}$$

Using a two-spin DOS $D_2 = 2D_1$ changes the criterion to $UD_2/2 > 1$. This only tests a $q = 0$ instability. At half filling the square lattice is nested and may instead order at $\mathbf{Q} = (\pi, \pi)$. A large DOS alone does not establish ferromagnetism. A full linear-response calculation compares the zeros of $1 - U\chi_0(\mathbf{q})$ at different wavevectors.

8.3.3 Analytical reduction for the half-filled square lattice

Take nearest-neighbor hopping $t > 0$, $\varepsilon_{\mathbf{k}} = -2t(\cos k_x + \cos k_y)$ and lattice constant one. At half filling $\rho_i = 1$, particle-hole symmetry fixes $\mu = U/2$. Choose $m_i = m(-1)^{i_x+i_y}$. In the folded-zone basis $(c_{\mathbf{k}\sigma}, c_{\mathbf{k}+\mathbf{Q},\sigma})$,

$$h_{\mathbf{k}\sigma} = \begin{pmatrix} \varepsilon_{\mathbf{k}} & -\sigma\Delta \\ -\sigma\Delta & -\varepsilon_{\mathbf{k}} \end{pmatrix}, \qquad \Delta = Um, \tag{8.33}$$

$$E_{\mathbf{k},\pm} = \pm E_{\mathbf{k}}, \qquad E_{\mathbf{k}} = \sqrt{\varepsilon_{\mathbf{k}}^2 + \Delta^2}, \tag{8.34}$$

$$m = \frac{1}{2N} \sum_{\mathbf{k}\in \mathrm{BZ}} \frac{\Delta}{E_{\mathbf{k}}} \tanh\left(\frac{E_{\mathbf{k}}}{2k_B T}\right), \tag{8.35}$$

$$1 = \frac{U}{2N} \sum_{\mathbf{k}\in \mathrm{BZ}} \frac{\tanh(E_{\mathbf{k}}/2k_B T)}{E_{\mathbf{k}}} \quad (m \neq 0). \tag{8.36}$$

The last two expressions use N momenta in the full Brillouin zone. Using the reduced zone requires a corresponding change of the prefactor. The moment obeys $m \leq 1/2$ and the spectral gap is 2Δ. Both spins have identical energies but different A/B sublattice weights. This Néel antiferromagnet is therefore not a spin-split altermagnet.

Example M7 Self-consistent moments and energies on the half-filled square lattice

Use a 400×400 midpoint grid, $k_x, k_y = 2\pi(j + 1/2)/N_k - \pi$, at $T = 0$ and $t = 1$. Start from $m^{(0)} = 0.2$. Evaluate the right-hand side above to obtain m_{out}, then mix $m^{(r+1)} = (1 - \eta)m^{(r)} + \eta m_{\text{out}}$ with $\eta = 0.5$. Require the unmixed residual $|m_{\text{out}} - m^{(r)}| < 10^{-12}$. The results are

U/t	m	$2\Delta/t$	$E_{\text{AF}}/(Nt)$	$(E_{\text{AF}} - E_{\text{PM}})/(Nt)$
1	0.059755	0.119511	-1.371752	-0.000630
2	0.188042	0.752168	-1.138860	-0.017738
4	0.345327	2.762616	-0.797029	-0.175907
8	0.446375	7.141996	-0.465878	-0.844756

Energies refer to the original Hubbard Hamiltonian without the $-\mu N$ term. The energy per site and its paramagnetic reference are

$$\frac{E_{\mathrm{AF}}}{N} = \frac{U}{4} + \frac{\Delta^2}{U} - \frac{1}{N}\sum_{\mathbf{k}} E_{\mathbf{k}}, \qquad \frac{E_{\mathrm{PM}}}{N} = \frac{U}{4} - \frac{1}{N}\sum_{\mathbf{k}} |\varepsilon_{\mathbf{k}}|. \tag{8.37}$$

Summing occupied eigenvalues without the double-counting correction produces incorrect energy comparisons. At $U/t = 4$, repeating the calculation with 100, 200 and 400 points per direction leaves the quoted six moment decimals unchanged. The sharp paramagnetic Fermi surface produces a more visible mesh error, so the energy differences shown use the 400 grid. The smaller weak-coupling gap at $U/t = 1$ requires a separate convergence check. Convergence at intermediate coupling does not establish convergence everywhere. Energy comparisons, independent initial guesses and unmixed residuals provide complementary tests of the numerical solution.

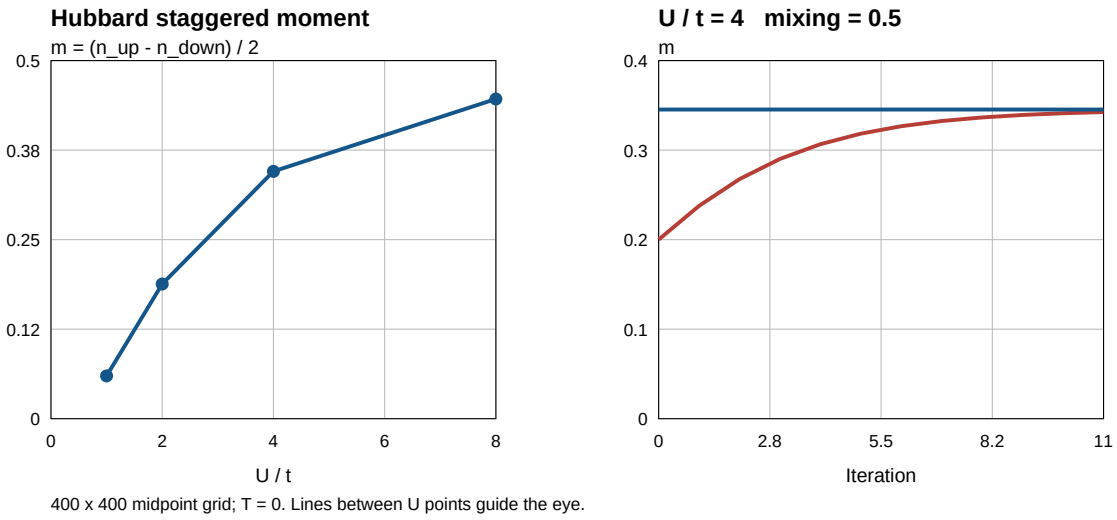

Figure 8.1: Calculated Hubbard mean-field moments and iteration trajectory. Lines between interaction values guide the eye.

8.3.4 Self-consistency on a general lattice

Away from a symmetry-fixed filling, μ must be determined. Re-solve the number equation after every update of the magnetic potential rather than keeping an old chemical potential and inadvertently changing carrier density. A reliable procedure is:

1. Specify sites, boundaries, hopping and particle number. Initialize paramagnetic, ferromagnetic, antiferromagnetic and appropriate random small-moment states separately.
2. Construct and diagonalize the Hermitian one-particle matrix for the current $\rho_i, \mathbf{m}_i$.
3. Adjust μ by bisection until $\sum_a f(E_a - \mu) = N_e$, then reconstruct the local density matrix.
4. Mix successive iterates and monitor unmixed residuals, number error and energy. Reduce mixing if oscillations occur; near a transition, use a more robust root solver if necessary.
5. Compare converged solutions at the same N_e, T using $F = \Omega + \mu N_e$ with the correct double-counting constant.
6. Refine the momentum mesh or system size and reduce thermal broadening to test moments and energy ordering.

Starting exactly from $m = 0$ in a symmetry-preserving algorithm leaves $m = 0$ forever. This demonstrates preserved symmetry, not stability of the paramagnet. Conversely, convergence to a nonzero moment from an antiferromagnetic seed establishes a stationary point in the chosen variational space, not an exact many-body ground state.

8.3.5 Slater magnetism and the strong-coupling limit

At $U/t \ll 1$, nesting motivates a Slater picture in which the gap is associated with ordered magnetism. At $U/t \gg 1$, charge fluctuations are suppressed and the low-energy spin scale is $4t^2/U$. Hartree–Fock produces a nearly saturated local moment and a large single-particle gap but does not correctly describe a Mott insulator without magnetic long-range order, Hubbard-band spectral weights or strong quantum fluctuations. A mean-field insulator is not automatically a complete theory of Mott physics.

Next-nearest-neighbor hopping t' disrupts perfect nesting, while changing the filling alters the competition between ferromagnetic, Néel and stripe states. Their comparison requires a variational space that accommodates each spatial period: a two-sublattice ansatz cannot produce longer-period magnetic structures. Finite-temperature results in two dimensions remain subject to the Mermin–Wagner limitation described above.

8.4 Mean-field applications to magnetic semiconductors and quantum wells

8.4.1 Coupled free energy of local moments and carriers

Local moments in a dilute magnetic semiconductor can develop collective order through their coupling to carriers. The theory of hole-mediated ferromagnetism developed by Dietl, Ohno and Matsukura balances the valence-band response against the entropy of the local moments[29]. Wang and colleagues connected exchange fields to inverted subbands in magnetically doped InAs/GaSb quantum wells and predicted a quantum anomalous Hall phase in a suitable parameter regime[30]. Both problems have the same self-consistent structure: moment polarization changes the bands, while band occupation changes the molecular field acting on the moments. A single-parabolic-band approximation exposes the basic scaling, whereas multiband models determine material-dependent matrix elements, anisotropy and topological conditions.

Let $n_M = N_0 x_{\mathrm{eff}}$ be the density of magnetic ions and $q = \langle S_z \rangle$ their average spin. Use contact exchange $H_{pd} = -J_{pd} \sum_I \mathbf{S}_I \cdot \mathbf{s}(\mathbf{R}_I)$, where J_{pd} has units of energy times volume and $\mathbf{s}$ is carrier spin per volume. Uniform mean field gives the carriers an energy field $h = J_{pd} n_M q$. If $f_c(h) = f_c(0) - \chi_s h^2/2 + \cdots$, the moments experience $h_M = J_{pd}\langle s_z \rangle$. Therefore

$$q = S B_S\!\left(\frac{S J_{pd} \langle s_z \rangle}{k_B T} \right), \qquad \langle s_z \rangle = \chi_s J_{pd} n_M q + O(q^3), \tag{8.38}$$

$$1 = \frac{S(S+1)}{3 k_B T_C}\, n_M J_{pd}^2 \chi_s(T_C). \tag{8.39}$$

Here χ_s is a spin response to an energy field, with units $(\text{energy} \times \text{volume})^{-1}$; it is not a dimensionless SI magnetic susceptibility. The sign of contact exchange determines whether carrier and ion spins align or antialign, but the linearized transition temperature contains J_{pd}^2. For a simple spin-$1/2$ parabolic band, the splitting is h and $\chi_s = D(E_F)/4$, with both spins included in the DOS.

8.4.2 The Dietl model of hole-mediated ferromagnetism

The Dietl model uses a 6×6 Kohn–Luttinger valence-band matrix to include heavy holes, light holes, the split-off band, SOC and strain, and evaluates $F_c(M)$ at fixed hole density. The entropy cost of polarizing local moments is minimized together with the carrier free energy. Its transition-temperature form is

$$T_C = \frac{x_{\text{eff}} N_0 S(S+1) \beta_{pd}^2 A_F \rho_s(T_C)}{12 k_B} - T_{\text{AF}}. \tag{8.40}$$

The symbol β_{pd} denotes the p–d exchange integral and must not be confused with inverse temperature. The factor A_F represents carrier-interaction enhancement, ρ_s is a spin DOS containing multiband matrix elements, and T_{AF} parametrizes competing antiferromagnetic interactions. Only in the strongly degenerate, SOC-free, single-parabolic-band limit does $\rho_s = D(E_F)$. In general, the total charge DOS cannot replace the multiband spin response.

Example M8 How hole density changes the mean-field temperature

Take $a = 0.5653\,\text{nm}$ and zinc-blende cation density $N_0 = 4/a^3$, together with $x_{\text{eff}} = 0.05$, $S = 5/2$, $N_0\beta_{pd} = -1.2\,\text{eV}$, $A_F = 1.2$ and $T_{\text{AF}} = 0$. Replace the real valence bands by one spin-degenerate parabolic band with $m^* = 0.5 m_e$ and $p = 3.5 \times 10^{20}\,\text{cm}^{-3} = 0.35\,\text{nm}^{-3}$. The calculation proceeds as follows:

$$N_0 = 22.1423\,\text{nm}^{-3}, \qquad k_F = (3\pi^2 p)^{1/3} = 2.18020\,\text{nm}^{-1}, \tag{8.41}$$

$$E_F = \frac{\hbar^2 k_F^2}{2m^*} = 0.362198\,\text{eV}, \qquad D(E_F) = \frac{m^* k_F}{\pi^2 \hbar^2} = 1.44948\,\text{eV}^{-1}\text{nm}^{-3}, \tag{8.42}$$

$$\beta_{pd} = -0.0541949\,\text{eV}\,\text{nm}^3, \qquad T_C^{\text{par}} = 47.86\,\text{K}. \tag{8.43}$$

This temperature is an order-of-magnitude estimate in the single-parabolic-band approximation. Multiband spin-orbit coupling and changes in material parameters can modify it. With all other parameters fixed, $D(E_F) \propto p^{1/3}$, so an eightfold increase in hole density only doubles T_C. Doubling the effective magnetic-ion density doubles the mean-field temperature directly. These scalings challenge the assumption that increasing doping raises the transition temperature without limit. Doping can also alter compensation, disorder, the active moment fraction and carrier localization, which lie outside this derivation.

8.4.3 Implementing a multiband calculation at fixed particle number

For each trial q, form $H_{\mathbf{k}}(q) = H_{\mathbf{k}}^{(0)} + H_{\text{ex}}(q)$ and diagonalize it to obtain $E_{n\mathbf{k}}(q)$. In an electron representation, the thermodynamic potential and number are

$$\Omega_c(q,\mu) = -k_B T \sum_{n\mathbf{k}} \ln[1 + e^{-\beta(E_{n\mathbf{k}}(q)-\mu)}], \tag{8.44}$$

$$N_c = \sum_{n\mathbf{k}} f(E_{n\mathbf{k}}(q) - \mu), \qquad F_c(q, N_c) = \Omega_c + \mu N_c, \tag{8.45}$$

$$q = S B_S\left[-\frac{S}{N_M k_B T} \left(\frac{\partial F_c}{\partial q} \right)_{N_c} \right]. \tag{8.46}$$

Here F_c and N_M refer to the same computational volume. A density formulation must divide both consistently. A hole representation is equally valid if energy reference and missing-electron number are defined consistently. Terms from the implicit $\mu(q)$ cancel by the number equation when differentiating F_c at fixed number. Numerically, use the Hellmann–Feynman sum $\sum f\langle n\mathbf{k}|\partial_q H|n\mathbf{k}\rangle$, or centered finite differences with a step-size convergence test.

Determining T_C does not require scanning every finite-magnetization curve. Evaluate the carrier free-energy curvature near $q = 0$, or calculate the zero-field static spin response. At finite temperature T_C must itself be solved iteratively because the Fermi factors and response depend on temperature. Replacing free energy by energy is justified only when the carriers are strongly degenerate and entropy corrections are negligible.

8.4.4 Interband magnetic response in InAs/GaSb quantum wells

In the basis $(|E1+\rangle, |H1+\rangle, |E1-\rangle, |H1-\rangle)$, initially neglect BIA, SIA and anisotropy. The four-band Hamiltonian is

$$H_0(\mathbf{k}) = (C - Dk^2)\mathbf{1} + (M_0 - Bk^2)\tau_z + Ak_x\sigma_z\tau_x - Ak_y\tau_y, \tag{8.47}$$

$$H_{\text{ex}} = \text{diag}(G_E, G_H, -G_E, -G_H) = g_0\sigma_z + g_z\sigma_z\tau_z, \tag{8.48}$$

$$g_0 = (G_E + G_H)/2, \qquad g_z = (G_E - G_H)/2. \tag{8.49}$$

The matrices σ distinguish time-reversed blocks and τ distinguishes electron-like and hole-like subbands. The term g_0 shifts the centers of the blocks, whereas g_z changes their Dirac masses. These distinct effects cannot be replaced by a single unspecified Zeeman splitting. The spin operator projected into the subband space contains subband-dependent exchange constants and wavefunction weights and therefore generally differs from bare $\sigma_z/2$.

For a Hermitian effective operator O, using perturbation $H' = -hO$, the static uniform response separates into

$$\chi_O^{\text{intra}} = \frac{1}{V}\sum_{n\mathbf{k}}[-f'(E_{n\mathbf{k}})]|O_{nn}(\mathbf{k})|^2, \tag{8.50}$$

$$\chi_O^{\text{inter}} = \frac{1}{V}\sum_{n\neq m,\mathbf{k}}\frac{f(E_{n\mathbf{k}}) - f(E_{m\mathbf{k}})}{E_{m\mathbf{k}} - E_{n\mathbf{k}}}|O_{nm}(\mathbf{k})|^2. \tag{8.51}$$

At degeneracy, numerator and denominator must be evaluated by a continuous limiting procedure rather than discarding a numerical $0/0$. The intraband term is selected by the thermal window around the Fermi surface. It vanishes at zero temperature with the chemical potential in a gap, but the interband term need not vanish. Insulating behavior therefore does not exclude an electronic contribution to the magnetic molecular field.

Example M9 Van Vleck response from a two-level matrix

Take $H = d_x\tau_x + d_z\tau_z$, with the lower band filled, upper band empty and $E_\pm = \pm d$, where $d^2 = d_x^2 + d_z^2$. For magnetic operator $O = \tau_z$, projection along $\mathbf{d}$ gives $|O_{-+}|^2 = 1 - d_z^2/d^2 = d_x^2/d^2$. Including both ordered transitions gives $\chi_{O,\mathbf{k}} = d_x^2/d^3$ for one momentum. If $d_x = 3\,\text{meV}$ and $d_z = 4\,\text{meV}$, then $d = 5\,\text{meV}$, the

squared matrix element is 0.36, and the response is $0.072\,\mathrm{meV}^{-1}$. For $O = \mathbf{1}$, the interband matrix element vanishes exactly. A small gap alone does not guarantee a large response.

In InAs/GaSb, hybridization and band inversion modify both DOS and matrix elements. The calculations of Wang and colleagues show that a small hybridization gap can enhance the magnetic instability in the parameter regime studied. Their $T_C \sim 30\,\mathrm{K}$ and approximately $10\,\mathrm{meV}$ gap are theoretical predictions of that model[30].

8.4.5 Mass inversion and the global insulating condition

The two block spectra are

$$E_{s,\pm}(k) = C - Dk^2 + sg_0 \pm \sqrt{A^2k^2 + (M_0 - Bk^2 + sg_z)^2}, \qquad s = \pm 1. \tag{8.52}$$

For the same B regularization, opposite signs of $M_0 + g_z$ and $M_0 - g_z$ can prevent the two block topological contributions from cancelling. However, the indirect gap between occupied and empty states must also be checked. At each k, sort the four energies as $E_1 \le E_2 \le E_3 \le E_4$ and define $E_g^{\mathrm{ind}} = \min_k E_3 - \max_k E_2$. Only if this is positive and the chemical potential lies inside it can the occupied-band Chern number describe a quantized insulating Hall plateau.

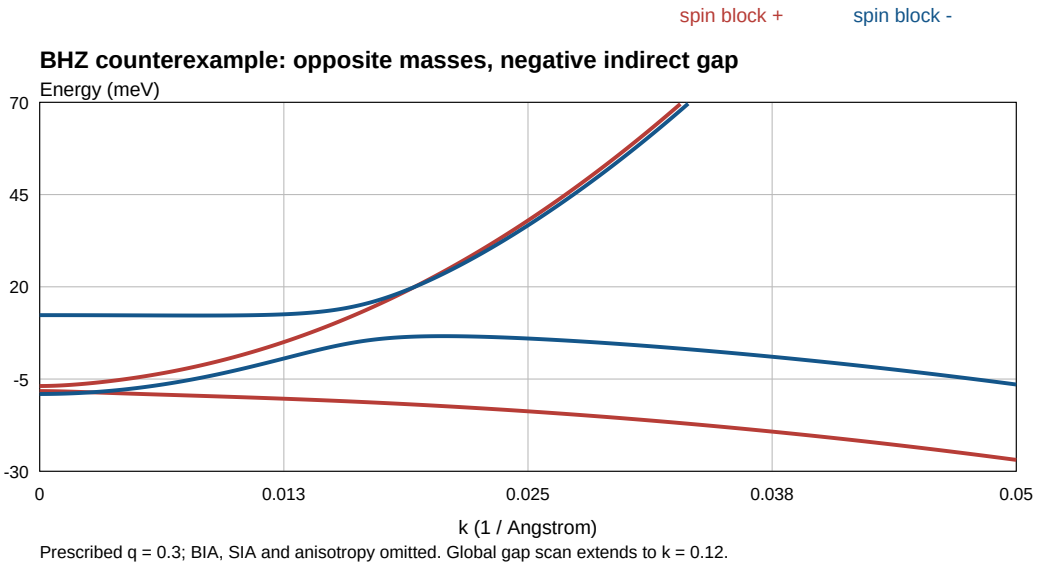

Figure 8.2: Four-band spectrum for M10. Opposite masses do not eliminate indirect band overlap.

Example M10 Mass inversion with indirect band overlap

Using the InAs/GaSb parameters of Wang and colleagues[30], take $A = 0.3\,\mathrm{eV\,\AA}$, $B = -38.5\,\mathrm{eV\,\AA}^2$, $D = -31.5\,\mathrm{eV\,\AA}^2$, $C = -2.97\,\mathrm{meV}$ and $M_0 = -5\,\mathrm{meV}$. Omit BIA, SIA, anisotropy and disorder. Since Dk^2 is an energy, the units of D are $\mathrm{eV\,\AA}^2$. With $F_1 = 0.52$, $F_4 = 0.48$, $x_{\mathrm{eff}} = 0.035$, $N_0\alpha = 0.5\,\mathrm{eV}$ and $N_0\beta_{pd} = -0.98\,\mathrm{eV}$, use the simplified exchange

$$G_E = x_{\mathrm{eff}} q [N_0\alpha F_1 + N_0\beta_{pd} F_4/3], \tag{8.53}$$

$$G_H = x_{\mathrm{eff}} q N_0\beta_{pd}. \tag{8.54}$$

For a prescribed trial average spin $q = 0.3$, this gives $G_E = 1.0836\,\text{meV}$ and $G_H = -10.2900\,\text{meV}$, with masses $+0.6868$ and $-10.6868\,\text{meV}$. Sorting the spectrum on 24001 points over $0 \le k \le 0.12\,\text{Å}^{-1}$ gives a minimum direct gap of $1.3736\,\text{meV}$ but an indirect gap of $-13.5129\,\text{meV}$. The masses have opposite signs, yet the bands overlap in energy. Mass inversion alone is therefore insufficient for a QAH insulating state. Here q is an externally specified parameter, not a solution of the magnetic self-consistency condition. The calculation is restricted to the four-band model and cannot determine the material phase diagram of an eight-band Kane heterostructure.

As a control, retain A, B, M_0 but impose the particle-hole-symmetric limit $C = D = 0$, $G_E = 10\,\text{meV}$ and $G_H = -10\,\text{meV}$. Then $g_0 = 0$, the masses are $+5$ and $-15\,\text{meV}$, and the continuum model has a positive global gap of approximately $10\,\text{meV}$. This demonstrates the value of controlling block-center shifts separately from mass shifts. Realizability requires the actual subband wavefunctions, doping distribution and self-consistent magnetization.

8.4.6 The eight-band Kane model and heterostructure self-consistency

The eight-band Kane problem determines heterostructure envelope functions. Discretize the growth direction, replace k_z by $-i\partial_z$, use layer-dependent material parameters with consistent interface operator ordering, and obtain subbands such as $E1, H1$ and their wavefunctions. Projection then supplies four-band parameters and exchange matrix elements. Test the spatial mesh, box size, subband truncation and boundary conditions. The weights F_1, F_4 must be recalculated when well thickness changes.

A quantitative material calculation also requires BIA/SIA, anisotropy, level broadening, the chemical-potential constraint and the layer-dependent magnetic doping profile. Broadening modifies the response near a small gap, so the free-energy curvature and transition temperature must use one consistently specified parameter set. The four-band approximation separates the roles of mass inversion, block-center shifts and interband response. Quantitative predictions for a particular sample additionally require their connection to the heterostructure envelope functions and self-consistent magnetization.

Chapter 9

Magnetic-Order Symmetry and Altermagnetism

9.1 Magnetic compensation and alternating splitting

A collinear magnet can have zero net moment and nevertheless possess spin-split bands at generic momentum. Altermagnetism focuses on this possibility allowed jointly by nonrelativistic exchange and crystal symmetry. We mainly use the usual narrower definition: compensated collinear order with sign-changing momentum-dependent spin splitting that survives when SOC is removed. This is not the same set as all zero-moment, time-reversal-breaking magnets. Classification boundaries differ across the literature, so definitions must be stated before comparing conclusions.

The original 2022 spin-symmetry work systematically described alternating splitting and symmetry-protected nodes[31]. Classification requires determining whether the magnetic structure is compensated, whether the nonrelativistic Hamiltonian protects spin degeneracy at generic $\mathbf{k}$, and which spatial operations relate opposite-spin bands when it does not. Answering these questions requires independent spin-space and real-space operations.

9.2 Magnetic space groups and spin space groups

In a conventional magnetic space group (MSG), spatial rotations act on both the crystal and the axial-vector magnetic moments, possibly combined with time reversal. With SOC, spin orientation relative to crystal axes is physically meaningful and this description is essential. Without SOC, exchange Hamiltonians admit independent global spin rotations. An operation preserving a chosen magnetic structure can be written $[U\|\{R|\mathbf{t}\}]$, with U acting in spin space and $\{R|\mathbf{t}\}$ in real space. A moment field must satisfy

$$\mathbf{m}(R\mathbf{r}+\mathbf{t}) = U\mathbf{m}(\mathbf{r}). \tag{9.1}$$

This is a geometric equation that can be tested directly. Proper spin-space rotations are represented by quantum spin-rotation operators. Improper operations, including spin inversion, require combination with time reversal; electronic bands also require spin-$1/2$ double-valued representations and antiunitary operations. The geometric symmetry of a vector field is not automatically a complete representation theory of its electrons.

For collinear order along z, arbitrary rotations about z leave the structure unchanged and form a continuous spin-only subgroup. Coplanar noncollinear and noncoplanar structures have different spin-only parts. Classification therefore usually separates this subgroup before studying combined spatial and spin operations. A spin group is not obtained by simply attaching an up/down label to the 230 ordinary space groups.

Independent 2024 studies established systematic enumerations and representation theory[32, 33]. Numerical group counts depend on the magnetic-supercell bound, collinearity assumptions and equivalence relations. No single finite count should be presented as the number of all possible spin space groups. For

example, the enumeration of Jiang and colleagues explicitly bounds the magnetic cell to at most twelve crystallographic cells.

9.3 Symmetry conditions for degeneracy at the same momentum

Kramers degeneracy requires an antiunitary operation $\mathcal{A}$ that preserves the momentum and satisfies $\mathcal{A}^2 = -1$. In the usual spin-$1/2$ setting where inversion commutes with time reversal, $P\mathcal{T}$ preserves $\mathbf{k}$ and squares to -1, protecting a doublet at every momentum. Time reversal alone generally maps $\mathbf{k}$ to $-\mathbf{k}$, giving a same-momentum degeneracy directly only at time-reversal-invariant momenta.

Likewise, $\mathcal{T}\tau$ does not automatically give a Kramers pair at every momentum: it changes momentum and its square contains a translation phase. A non-SOC collinear antiferromagnet can instead possess a unitary spin-group operation combining a spin flip with a sublattice translation, directly relating the two spin spectra at the same $\mathbf{k}$. The conclusion may still be degeneracy everywhere, but the action on momentum must be part of the proof.

If opposite-spin sublattices are connected by a crystal rotation R, the usual constraint is

$$E_\uparrow(\mathbf{k}) = E_\downarrow(R\mathbf{k}), \qquad \delta(R\mathbf{k}) = -\delta(\mathbf{k}), \qquad \delta(\mathbf{k}) = \frac{E_\uparrow(\mathbf{k}) - E_\downarrow(\mathbf{k})}{2}. \tag{9.2}$$

Generic $\mathbf{k}$ and $R\mathbf{k}$ differ, so the constraint does not force degeneracy at the same point. On invariant lines satisfying $R\mathbf{k} = \mathbf{k} + \mathbf{G}$, it can instead enforce $\delta = 0$. This is a practical route from symmetry to spin-splitting nodes. Screw axes and glide planes introduce translation phases that also affect representations and degeneracies, so point-group analysis alone is insufficient there.

9.4 Alternating spin splitting and spin transport

9.4.1 Example M11 Momentum structure of d-wave spin splitting

Consider the phenomenological one-effective-orbital band Hamiltonian

$$H(\mathbf{k}) = -2t(\cos k_x + \cos k_y)\mathbf{1} + J_a(\cos k_x - \cos k_y)\sigma_z, \tag{9.3}$$

$$E_\sigma(\mathbf{k}) = \varepsilon_0(\mathbf{k}) + \sigma\delta(\mathbf{k}), \qquad \delta(\mathbf{k}) = J_a(\cos k_x - \cos k_y). \tag{9.4}$$

This reduced model diagnoses band symmetry; it does not independently specify the complete microscopic orbital and magnetic-sublattice structure. The operation C_{4z} maps (k_x, k_y) to $(-k_y, k_x)$ and reverses δ. A simultaneous spin rotation by π about x reverses σ_z, so the combined operation preserves the Hamiltonian. Inversion gives $\delta(-\mathbf{k}) = \delta(\mathbf{k})$. Both spins meet along $k_x = \pm k_y$, where $\delta = 0$.

For $t = 1\,\text{eV}$ and $J_a = 0.10\,\text{eV}$, $X = (\pi, 0)$ has $\delta = -0.20\,\text{eV}$ and $E_\uparrow - E_\downarrow = -0.40\,\text{eV}$. At $Y = (0, \pi)$ the splitting is $+0.40\,\text{eV}$; it vanishes at Γ, M and on the diagonals. Changing variables by $\mathbf{k} \to C_4\mathbf{k}$ in a sum over the symmetric Brillouin zone gives

$$N_\uparrow = \sum_{\mathbf{k}} f[E_\uparrow(\mathbf{k})] = \sum_{\mathbf{k}} f[E_\downarrow(C_4\mathbf{k})] = N_\downarrow. \tag{9.5}$$

Zero net spin therefore does not require equal spin energies at every momentum. Adding a uniform $b\sigma_z$ breaks the C_4 pairing and generally permits a net moment. Making the crystal inequivalent along x and y also requires a new check of the compensation symmetry.

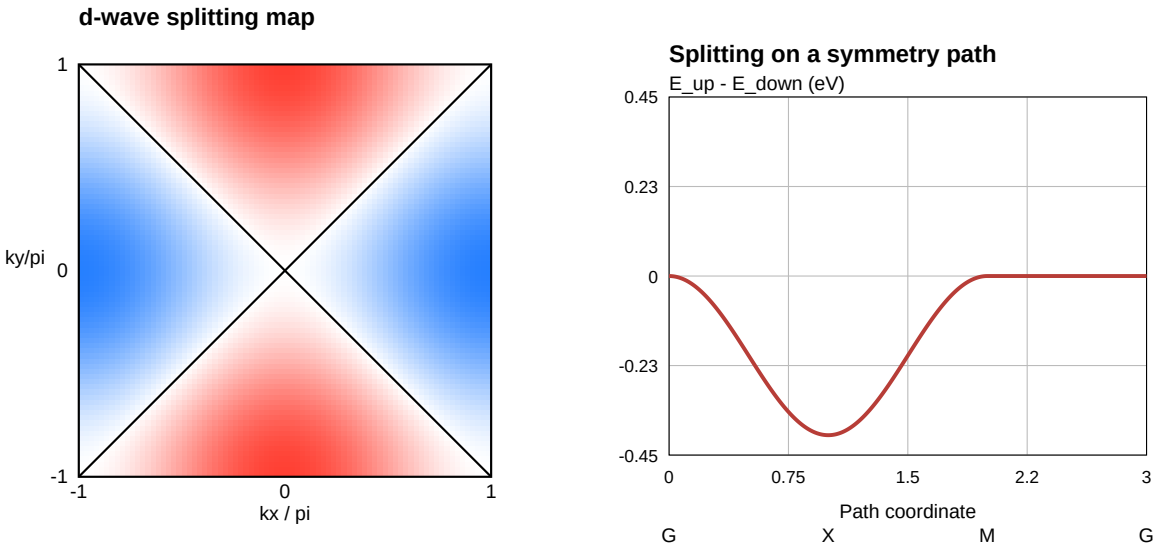

Figure 9.1: Alternating splitting in M11. Red and blue indicate opposite signs; black diagonals are nodes. G denotes Gamma.

9.4.2 Example M12 Spin-polarized current with zero net moment

Near Γ, take $\varepsilon_0 = \alpha(k_x^2 + k_y^2)$ and $\delta = \beta_a(k_x^2 - k_y^2)$ with $|\beta_a| < \alpha$. The two spin channels have elliptical Fermi surfaces with interchanged long and short axes. Their inverse masses are

$$\frac{1}{m_{x\sigma}} = \frac{2(\alpha + \sigma\beta_a)}{\hbar^2}, \qquad \frac{1}{m_{y\sigma}} = \frac{2(\alpha - \sigma\beta_a)}{\hbar^2}. \tag{9.6}$$

If the two channels each have density $n/2$ and the same relaxation time, $\sigma_{xx}^{\sigma} = (n/2)e^2\tau/m_{x\sigma}$. The spin polarization of a current along x is

$$P_x = \frac{\sigma_{xx}^{\uparrow} - \sigma_{xx}^{\downarrow}}{\sigma_{xx}^{\uparrow} + \sigma_{xx}^{\downarrow}} = \frac{\beta_a}{\alpha}, \qquad P_y = -P_x. \tag{9.7}$$

For $\beta_a/\alpha = 0.2$, the result is $P_x = 20\%$ and $P_y = -20\%$, despite zero equilibrium net moment. The effect comes from velocity weighting rather than DOS alone and connects directly to the Fermi-surface integrals of transport theory. For diagonal current directions, rotate the conductivity tensors rather than reuse P_x. Real scattering times, interface transmission and SOC-induced spin mixing can change the value. The quoted polarization is a model result within the equal-relaxation-time approximation, rather than a measured device efficiency.

The spin eigenvectors of this real diagonal Hamiltonian are independent of momentum, so its Berry curvature vanishes. It can support spin-polarized longitudinal transport while having no intrinsic anomalous Hall conductivity. Alternating spin splitting does not automatically imply an AHE; SOC, moment orientation and residual magnetic point-group constraints must also be checked.

9.5 Spin-group classification and spin-orbit coupling

9.5.1 Group operations and sublattice cosets

For a crystal and magnetic structure, first find spatial operations preserving the atomic positions. For each operation, test whether one common spin rotation U maps every moment to the moment at its target position. One must not choose a different rotation for each atom. Next test closure of the combined operations and identify the spin-only subgroup, magnetic translations and spin point group. An electronic-band calculation additionally needs the little group and its double-valued representations at the selected momentum.

For a two-colour collinear structure, spatial operations preserving each spin sublattice form a subgroup H, while sublattice-exchanging operations may form a coset AH. For index two, the simplified nontrivial structure is $[E\|H] + [C_2\|A][E\|H]$, where C_2 reverses the ordered spin axis. If A changes only a phase at generic momentum, a same-momentum spin degeneracy can be protected. If A is a nontrivial crystal rotation, it may instead relate opposite spins at rotated momenta. The combined actions on momentum and spin determine the constraints on band degeneracies and splittings.

9.5.2 Example M13 Effects of spin-orbit coupling on degeneracies

First verify $[C_{2x}\|C_{4z}]$ in the non-SOC model. After adding $H_{\mathrm{SOC}} = \lambda \mathbf{L} \cdot \mathbf{S}$, rotating spin independently of the orbitals is generally no longer a symmetry. Surviving operations must preserve the crystal, magnetic structure and SOC term simultaneously. Nodes protected only by the larger spin group may gap and some spin quantum numbers may cease to be conserved, while degeneracies protected by the actual MSG survive. It is incorrect to claim that SOC gaps every node. Determine which matrix terms are allowed by the residual group, then follow the gap and response as functions of small λ.

The 2026 oriented-spin-space-group framework incorporates a fixed moment orientation, connects SSG and MSG descriptions, and distinguishes non-SOC symmetry-enforced compensation from magnetization allowed after SOC is included[38]. Both magnetic geometry and its orientation relative to the crystal must therefore be recorded: different orientations of the same spin arrangement can admit different transport tensors.

9.6 Material evidence and low-dimensional magnetic order

Identifying an altermagnetic material requires combined information about magnetic structure, band splitting and momentum dependence. Spin-integrated photoemission constrains the band structure, spin-resolved photoemission adds spin information, and bulk quantum oscillations constrain extremal Fermi-surface orbits. Symmetry determines which orders are allowed; experiment establishes which order a particular sample realizes.

Photoemission work on MnTe in 2024 provided evidence for degeneracy lifting associated with altermagnetism[34]. A 2024 CrSb study compared spin-integrated ARPES with band calculations; it did not directly resolve spin. A 2025 study added spin-resolved measurements and three-dimensional momentum mapping[35, 36]. These measurements place complementary constraints on band structure and spin assignment; a splitting magnitude alone cannot replace that combined evidence.

The magnetic order of RuO_2 remains contested. A 2025 NQR study found no corresponding static moments or magnetic fluctuations in the powder samples it examined[37]. It is therefore inappropriate to

describe every RuO_2 sample as an established altermagnet. Stoichiometry, film strain, surfaces and defects must be specified alongside the measurement; symmetry allowing an order does not establish that a sample realizes it.

A 2026 surface-spin-group study predicts that symmetry reduction at surfaces of bulk antiferromagnets can allow altermagnetic splitting, with calculations for candidate materials[39]. This offers a route for separating bulk and surface signals, not experimental confirmation of every predicted surface. Work on two-dimensional spin layer groups also establishes constraints distinct from simplified three-dimensional classifications[40]; applying a bulk group table directly to a monolayer can miss allowed structures.

9.7 Symmetry breaking and magnetic stability

The nodes and compensated moment in M11 are constrained by combined rotational symmetry. A uniform field, a C_4-breaking anisotropy and SOC modify those constraints in different ways. Determining the surviving group for each perturbation establishes whether nodes may gap, whether Brillouin-zone integrals must remain zero and which transport-tensor components are allowed. Fermi-surface and band calculations then determine the size of the permitted effects at specified parameters. Symmetry permission and a nonzero numerical value are distinct conclusions.

Magnetic stability additionally requires an energy criterion. Combining Hubbard self-consistency with a multiorbital lattice permits comparison of a candidate altermagnetic state's free energy with competing orders at the same particle number and temperature. Alternating band splitting does not guarantee that its underlying magnetic structure minimizes the free energy. If superconductivity is included, momentum-dependent splitting changes the available pairing phase space. A magnetic splitting and a superconducting gap can both transform with d-wave symmetry while remaining distinct order parameters with different microscopic mechanisms.

9.7.1 Example M14 Alternating splitting in a two-sublattice model

To connect the phenomenological splitting to Hubbard mean field, consider a collinear two-sublattice Hamiltonian. The matrices τ act on A/B sublattices and σ on spin; m is a staggered exchange field in energy units. Take

$$H(\mathbf{k}) = \epsilon_0(\mathbf{k})\mathbf{1} + t_x(\mathbf{k})\tau_x + t_z(\mathbf{k})\tau_z + m\tau_z\sigma_z, \tag{9.8}$$

$$E_{\sigma,\pm} = \epsilon_0 \pm \sqrt{t_x^2 + (t_z + \sigma m)^2}. \tag{9.9}$$

If $t_z = 0$, both spins have the same energies, as in the ordinary bipartite Néel model. If $t_z = \delta t(\cos k_x - \cos k_y)$ while t_x, ϵ_0 are invariant under interchange of k_x, k_y, rotation exchanges the two spin spectra. For $|m| \ll \sqrt{t_x^2 + t_z^2}$, expansion gives

$$E_{\uparrow,\pm} - E_{\downarrow,\pm} \simeq \pm \frac{2mt_z(\mathbf{k})}{\sqrt{t_x(\mathbf{k})^2 + t_z(\mathbf{k})^2}}. \tag{9.10}$$

At one momentum, choose $t_x = 0.50\,\text{eV}$, $t_z = 0.20\,\text{eV}$ and $m = 0.10\,\text{eV}$. The exact upper-band splitting is $\sqrt{0.25 + 0.09} - \sqrt{0.25 + 0.01} = 73.193\,\text{meV}$; the first-order estimate is $74.278\,\text{meV}$. Rotation reverses t_z and therefore reverses the splitting. At a node with $t_z = 0$, the spin energies remain equal for any m. A staggered field alone is thus insufficient: the sublattice-dependent momentum structure is essential.

For self-consistency, replace m by the local interaction field Um_A, impose $m_B = -m_A$ as a trial pattern and test its stability. Space-group and orbital information constrain the allowed functions t_x, t_z. This matrix is a motivated model example, not a universal microscopic Hamiltonian for every material.

9.8 Spin textures and the topological Hall response

Noncollinear magnetic order can form real-space spin textures with nonzero topological charge. Their electronic response arises from a mechanism distinct from momentum-dependent splitting in a collinear altermagnet. For a slowly varying unit magnetization direction $\mathbf{n}(\mathbf{r})$, a carrier spin that follows the local exchange field adiabatically acquires a real-space Berry phase after projection to one spin branch[41]. Define

$$Q = \frac{1}{4\pi}\int \mathbf{n}\cdot(\partial_x\mathbf{n}\times\partial_y\mathbf{n})\,\mathrm{d}x\mathrm{d}y, \qquad |B_{\mathrm{em}}| \text{ scale} = \frac{\hbar}{2e}\left|\mathbf{n}\cdot(\partial_x\mathbf{n}\times\partial_y\mathbf{n})\right|. \tag{9.11}$$

The emergent fields have opposite signs for the two adiabatic spin branches. The sign also depends on the Berry-connection and carrier-charge convention, so it should not be specified without identifying the projected branch. A texture carries emergent flux of magnitude $(h/e)|Q|$.

9.8.1 Example M15 Topological charge and emergent field of an axisymmetric texture

Parametrize $\mathbf{n} = (\sin\theta\cos\phi, \sin\theta\sin\phi, \cos\theta)$ with $\theta = \theta(r)$ and $\phi = w\varphi + \gamma$. Then

$$Q = \frac{w}{2}[\cos\theta(0) - \cos\theta(\infty)]. \tag{9.12}$$

For a down-pointing core and up-pointing background, $\theta(0) = \pi$ and $\theta(\infty) = 0$, so $Q = -w$, independent of helicity γ. If each $Q = -1$ texture occupies mean area $A = \pi(50\,\mathrm{nm})^2$, the average emergent-field magnitude is $(h/e)/A = 0.527\,\mathrm{T}$. This is a geometric flux estimate, not the applied magnetic field.

In an adiabatic single-band model with a small Hall angle and appropriate scattering assumptions, one may estimate $|\rho_{yx}^{\mathrm{top}}| \sim |PR_0\overline{B}_{\mathrm{em}}|$, where P is transport spin polarization. Multiband compensation, nonadiabaticity, texture scattering and ordinary AHE can modify the result. An extra hump in a Hall curve alone does not uniquely establish skyrmions; imaging, scattering or independent texture-density evidence is needed. A texture-induced topological Hall response depends on real-space Berry phase and carrier motion; the quantized Hall response of Chern bands instead requires the appropriate insulating occupation and gap.

9.9 Bulk quantum oscillations of altermagnetic CrSb

9.9.1 Example M16 Extremal orbit areas and effective masses

The published 2026 study by Long et al. used angle-dependent bulk quantum oscillations to investigate the three-dimensional g-wave altermagnetic order of CrSb[42]. At one orientation, $\theta = 84.8°$, $\phi = 21.4°$, the reported frequencies are $F_1 = 3.41\,\mathrm{kT}$ and $F_2 = 3.82\,\mathrm{kT}$, with LK masses $m_1^* = 1.73(5)m_e$ and $m_2^* = 1.84(5)m_e$. Numbers in parentheses give the uncertainty in the last quoted digits.

Figure 9.2 connects the frequency branches to their thermal damping. The FFT spectra constrain extremal areas, while the temperature dependence of the amplitudes constrains cyclotron masses. Their combination tests the relation between the orbits.

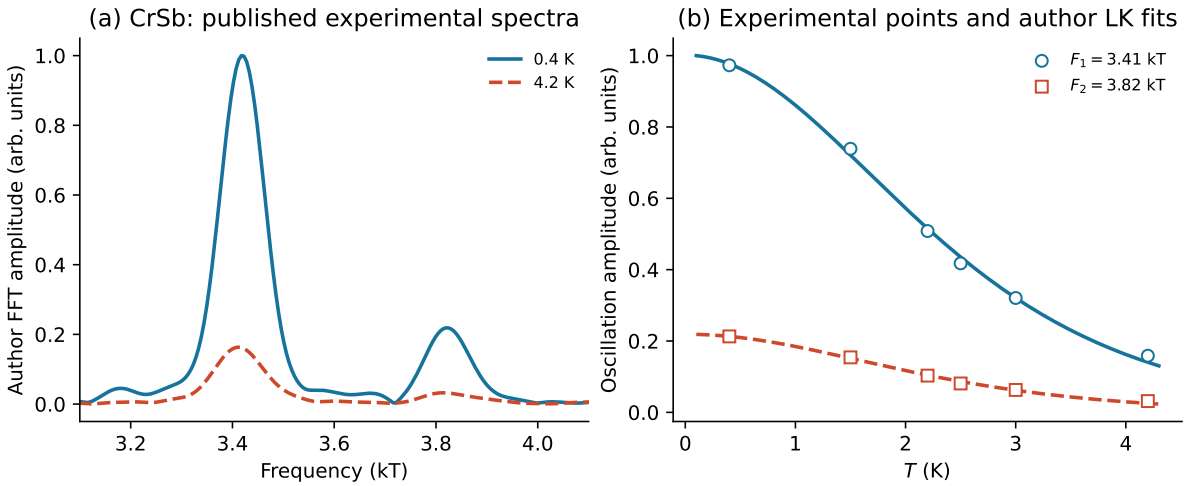

Figure 9.2: Quantum oscillations in CrSb for $\theta = 84.8°$ and $\varphi = 21.4°$. (a) FFT spectra of background-subtracted signals at 0.4 and $4.2\,\mathrm{K}$. (b) Temperature-dependent amplitudes of two branches: symbols are experimental data and curves are the authors' LK fits. Replotted from Fig. 4(b,c) and the public data of Long et al.; dataset licensed CC BY 4.0.[42, 57]

First apply the Onsager relation, $A_i = 2\pi e F_i/\hbar$. With $1\,\mathrm{kT} = 10^3\,\mathrm{T}$ and $1\,\text{Å}^{-2} = 10^{20}\,\mathrm{m}^{-2}$, the areas are $A_1 = 0.32551\,\text{Å}^{-2}$ and $A_2 = 0.36465\,\text{Å}^{-2}$. These are extremal orbit cross sections perpendicular to the field, not complete three-dimensional Fermi volumes.

Next test a restricted hypothesis. If the orbits are geometrically similar spin-split descendants with approximately equal velocity profiles and mass renormalizations, then $\partial A/\partial E$ scales with linear orbit size. Thus $m_1^*/m_2^* \simeq \sqrt{A_1/A_2} = \sqrt{F_1/F_2}$. The measured-mass ratio is 0.9402 ± 0.0373, propagating independent standard uncertainties of $0.05 m_e$; the frequency prediction is 0.9448. Their agreement supplies an orbit-consistency check beyond simply observing two peaks.

Two frequencies alone can also arise from ordinary multiband structure or distinct extremal orbits. An altermagnetic interpretation therefore requires the angular dependence, crystal symmetry, magnetic order and band calculations together. An area difference is not a pointwise energy difference: $F_2 - F_1$ cannot directly yield the largest exchange splitting without reconstructing the dispersion. The areas and mass ratio above are inferred from this set of published measurements.

Part V

Superconductivity

Chapter 10

Superconductivity: foundations and applications

A theory of superconductivity must account for the single-particle gap, macroscopic phase coherence, and Meissner screening. The two-electron Cooper problem reveals the pairing instability of a Fermi surface, BCS mean field describes a macroscopically paired state, and phase stiffness determines whether pairing correlations produce macroscopic superconductivity. Microscopic gap and number equations determine the pairing amplitude and chemical potential; London and Ginzburg–Landau theories describe screening, critical fields, currents, and phase interference. These descriptions have different regimes of validity, and their parameters must be connected separately to experimental measurements.

10.1 Experimental characteristics of superconductivity

10.1.1 Zero resistance and the Meissner effect

Zero resistance means that a steady current does not produce the usual dissipative voltage. It does not, by itself, imply magnetic-field expulsion. If a normal conductor becomes an ideal conductor in an existing magnetic field, Faraday's law and infinite conductivity only prevent subsequent changes in the magnetic flux. Within the appropriate field and temperature range, a superconductor instead approaches an equilibrium state with screening currents and a field that decays into its interior. The distinction between these preparation histories is central to the Meissner effect.

Finite dimensions, demagnetization fields, vortices, and penetration depth limit the literal statement that the internal field vanishes. A type-II superconductor forms a mixed state between its lower and upper critical fields: a condensate persists while flux penetrates through vortices. Experimental identification therefore combines transport, magnetic response, and bulk thermodynamics; a resistance drop alone is not a complete test.

10.1.2 Single-particle and pair-breaking gaps

For an isotropic pairing amplitude Δ, creating a Bogoliubov quasiparticle at the Fermi surface costs $|\Delta|$. Bulk absorption that preserves even fermion parity often requires two quasiparticles and has a threshold $2|\Delta|$. An ideal normal-metal–insulator–superconductor junction has the zero-temperature quasiparticle threshold $e|V| = \Delta$; a junction between identical superconductors has threshold 2Δ. Coherent Josephson pair tunnelling is a different process and can carry current at zero voltage.

The normal-state low-temperature heat capacity can be written $C_n = \gamma T + \beta_{\text{ph}} T^3$. In a fully gapped superconductor, the electronic contribution is controlled by $\exp[-\Delta/(k_B T)]$ at sufficiently low temperature, with a nonconstant prefactor. Nodes, residual normal regions, and impurity states change this law. Electronic heat carriers are suppressed in a fully gapped state, but the total thermal conductivity need not be small. Phonons, nodal quasiparticles, and vortices can contribute substantially to thermal transport.

10.2 The Cooper problem and its binding energy

Place two electrons of zero total momentum above a zero-temperature Fermi sea and choose a spin singlet:

$$|\Psi\rangle = \sum_{k>k_F} g_{\mathbf{k}} c^\dagger_{\mathbf{k}\uparrow} c^\dagger_{-\mathbf{k}\downarrow} |\mathrm{FS}\rangle, \qquad g_{-\mathbf{k}} = g_{\mathbf{k}}. \tag{10.1}$$

Take a constant attractive matrix element $-g/\mathcal{V}$ in an *energy* shell of width ω_D above the Fermi surface, where $g > 0$ and $\mathcal{V}$ is the volume. The symbol ω_D denotes an energy cutoff. If the phonon angular frequency is denoted by Ω_D, then $\omega_D = \hbar\Omega_D$. Writing $E = 2E_F - E_b$, the Schrödinger equation becomes

$$(2\xi_{\mathbf{k}} + E_b) g_{\mathbf{k}} = \frac{g}{\mathcal{V}} \sum_{\mathbf{k}'} g_{\mathbf{k}'}, \qquad 1 = g\nu_0 \int_0^{\omega_D} \frac{d\xi}{2\xi + E_b}. \tag{10.2}$$

Here ν_0 is always the normal-state density of states *per spin and per volume* at the Fermi energy. With $\lambda = g\nu_0$,

$$\frac{1}{\lambda} = \frac{1}{2} \ln \frac{2\omega_D + E_b}{E_b}, \qquad E_b = \frac{2\omega_D}{e^{2/\lambda} - 1} \simeq 2\omega_D e^{-2/\lambda}. \tag{10.3}$$

Arbitrarily weak attraction produces a bound solution because the finite density of states near the Fermi surface generates a logarithm. This differs from a short-range attractive potential in three-dimensional vacuum, where the density of states vanishes at the band bottom and a threshold attraction may be needed. The two problems do not support the same unconditional statement about weak attraction.

10.2.1 Example SC1 The Cooper binding energy is not the BCS gap

For $\lambda = 0.30$ and $\omega_D = 20\,\mathrm{meV}$, the two-particle binding energy is $E_b = 0.05097\,\mathrm{meV}$. The macroscopic BCS solution derived below gives $\Delta_0 = \omega_D/\sinh(1/\lambda) = 1.4288\,\mathrm{meV}$, about 28 times larger. In the BCS state many time-reversed states above and below the Fermi surface rearrange together. Both its integration range and its self-consistent wavefunction differ from the frozen-sea Cooper problem. Substituting E_b for Δ_0 in the BCS gap ratio is therefore incorrect.

10.3 Effective attractive interactions

Ionic displacement couples to electronic density. Integrating out a harmonic oscillator produces a frequency-dependent effective interaction. In a simplified mode its phonon contribution has the form

$$V_{\mathrm{ph}}(\mathbf{q}, i\omega_m) = -\frac{2|g_{\mathbf{q}}|^2 \hbar\Omega_{\mathbf{q}}}{(\hbar\omega_m)^2 + (\hbar\Omega_{\mathbf{q}})^2}. \tag{10.4}$$

The negative sign allows attraction, but Coulomb repulsion remains. The constant-shell BCS interaction compresses retardation, the phonon spectrum, and the renormalized repulsion into an effective parameter. It is a useful weak-coupling baseline. A fitted λ alone does not identify a material's microscopic pairing mechanism.

Unconventional pairing does not necessarily invalidate the structure of a BCS self-consistency equation. Instead, the interaction kernel may depend strongly on momentum, orbital indices, or frequency, and its leading eigenfunction need not be a constant of one sign. Strong coupling, self-energy effects, and dynamical screening require extensions beyond the static mean-field treatment used here.

10.4 From a variational state to the mean-field Hamiltonian

10.4.1 The reduced model and anomalous average

Define $P_{\mathbf{k}} = c_{-\mathbf{k}\downarrow} c_{\mathbf{k}\uparrow}$ and

$$K = H - \mu N = \sum_{\mathbf{k}\sigma} \xi_{\mathbf{k}} n_{\mathbf{k}\sigma} - \frac{g}{\mathcal{V}} \sum_{\mathbf{k}\mathbf{k}'} P_{\mathbf{k}}^\dagger P_{\mathbf{k}'}, \quad \Delta = \frac{g}{\mathcal{V}} \sum_{\mathbf{k}} \langle P_{\mathbf{k}} \rangle. \tag{10.5}$$

Expand $P = \langle P \rangle + \delta P$ and neglect $\delta P^\dagger \delta P$. This gives

$$K_{\mathrm{MF}} = \sum_{\mathbf{k}\sigma} \xi_{\mathbf{k}} n_{\mathbf{k}\sigma} - \sum_{\mathbf{k}} (\Delta P_{\mathbf{k}}^\dagger + \Delta^* P_{\mathbf{k}}) + \mathcal{V} \frac{|\Delta|^2}{g}. \tag{10.6}$$

The last term removes double counting of the interaction energy. Although it does not change eigenvectors at fixed Δ, it is essential when comparing self-consistent solutions or calculating condensation energy. Our off-diagonal pairing convention is $-\Delta$. An overall sign change of Δ is a phase convention and does not change the spectrum.

10.4.2 The BCS wavefunction and number fluctuations

Choose

$$|\mathrm{BCS}\rangle = \prod_{\mathbf{k}} (u_{\mathbf{k}} + v_{\mathbf{k}} P_{\mathbf{k}}^\dagger)|0\rangle, \qquad |u_{\mathbf{k}}|^2 + |v_{\mathbf{k}}|^2 = 1. \tag{10.7}$$

Each factor coherently combines an empty state with a doubly occupied pair state. This is not a collection of independent tightly bound real-space molecules: in weak coupling, pairs overlap over distances much greater than the interparticle spacing. The mean particle number and variance are

$$\langle N \rangle = 2 \sum_{\mathbf{k}} |v_{\mathbf{k}}|^2, \qquad (\delta N)^2 = 4 \sum_{\mathbf{k}} |u_{\mathbf{k}} v_{\mathbf{k}}|^2. \tag{10.8}$$

Relative fluctuations become small in a macroscopic system, while the grand-canonical state conveniently describes a coherent phase. Number constraints and charging energy cannot be neglected for an isolated small island.

10.5 Bogoliubov transformation and quasiparticle spectra

Take real positive Δ and the Nambu spinor $\Psi_{\mathbf{k}} = (c_{\mathbf{k}\uparrow}, c_{-\mathbf{k}\downarrow}^\dagger)^T$. Its matrix is

$$\mathcal{H}_{\mathbf{k}} = \begin{pmatrix} \xi_{\mathbf{k}} & -\Delta \\ -\Delta & -\xi_{\mathbf{k}} \end{pmatrix}, \qquad \det(\mathcal{H} - E) = E^2 - \xi_{\mathbf{k}}^2 - \Delta^2. \tag{10.9}$$

The positive excitation energy is $E_{\mathbf{k}} = \sqrt{\xi_{\mathbf{k}}^2 + \Delta^2}$. A positive-energy eigenvector is $(u, -v)^T$, where

$$u^2 = \frac{1}{2}(1 + \xi/E), \qquad v^2 = \frac{1}{2}(1 - \xi/E), \qquad uv = \frac{\Delta}{2E}. \tag{10.10}$$

The transformation $c_{\mathbf{k}\uparrow} = u\gamma_{\mathbf{k}\uparrow} + v\gamma_{-\mathbf{k}\downarrow}^\dagger$ and $c_{-\mathbf{k}\downarrow}^\dagger = -v\gamma_{\mathbf{k}\uparrow} + u\gamma_{-\mathbf{k}\downarrow}^\dagger$ preserves fermionic anticommutators. Substitution cancels the anomalous terms because their coefficient is $2\xi uv - \Delta(u^2 - v^2) = 0$.

A quasiparticle is a coherent electron–hole mixture whose charge expectation depends on ξ/E. Far from the Fermi surface it resembles an electron or a hole; at $\xi = 0$ the weights are equal. Nambu space enlarges the representation, not the number of physical degrees of freedom. Constant terms and redundant counting must therefore be treated consistently in thermodynamic calculations.

10.5.1 Example SC2 Spectrum and coherence factors

Let $\Delta = 1\,\text{meV}$. At $\xi = 0$, $E = 1\,\text{meV}$ and $u^2 = v^2 = 1/2$. At $\xi = 2\,\text{meV}$, $E = \sqrt{5}\,\text{meV}$, $u^2 = 0.947214$, and $v^2 = 0.052786$. Reversing ξ exchanges the weights but preserves the excitation energy. Positive- and negative-bias spectral weights thus carry wavefunction information. Eigenvalues alone do not fully characterize a localized subgap state.

10.6 Finite-temperature gap and number equations

At thermal equilibrium $\langle \gamma^\dagger \gamma \rangle = f(E)$, so

$$\langle P_{\mathbf{k}} \rangle = u_{\mathbf{k}} v_{\mathbf{k}} [1 - 2f(E_{\mathbf{k}})] = \frac{\Delta}{2E_{\mathbf{k}}} \tanh \frac{E_{\mathbf{k}}}{2k_B T}. \tag{10.11}$$

For a nonzero pairing solution, eliminating Δ gives

$$1 = \frac{g}{\mathcal{V}} \sum_{\mathbf{k}}^{\text{shell}} \frac{1}{2E_{\mathbf{k}}} \tanh \frac{E_{\mathbf{k}}}{2k_B T}, \tag{10.12}$$

$$n = \frac{1}{\mathcal{V}} \sum_{\mathbf{k}} \left[1 - \frac{\xi_{\mathbf{k}}}{E_{\mathbf{k}}} \tanh \frac{E_{\mathbf{k}}}{2k_B T} \right]. \tag{10.13}$$

The density equation includes both spins. For an approximately constant density of states, a broad band, and weak pairing, one can often hold $\mu \simeq E_F$. At low density, near a band singularity, or for stronger pairing, solve simultaneously for μ and Δ. Dividing by Δ discards the normal solution, which must be retained separately when identifying a phase transition.

For constant density of states, integrating over both signs of ξ cancels the factor of two in the denominator:

$$\frac{1}{\lambda} = \int_0^{\omega_D} \frac{d\xi}{\sqrt{\xi^2 + \Delta^2}} \tanh \frac{\sqrt{\xi^2 + \Delta^2}}{2k_B T}. \tag{10.14}$$

With a single-spin density of states, no additional factor $1/2$ belongs on the right. The factor is fixed jointly by spin counting and the positive- and negative-energy integration ranges.

10.7 Zero temperature and the transition temperature

At zero temperature the integral becomes $\operatorname{arsinh}(\omega_D/\Delta_0)$, hence

$$\Delta_0 = \frac{\omega_D}{\sinh(1/\lambda)} \simeq 2\omega_D e^{-1/\lambda}. \tag{10.15}$$

At a continuous transition, set $\Delta \to 0$:

$$\frac{1}{\lambda} = \int_0^{\omega_D} \frac{d\xi}{\xi} \tanh \frac{\xi}{2k_B T_c}, \qquad k_B T_c \simeq \frac{2e^\gamma}{\pi} \omega_D e^{-1/\lambda}. \tag{10.16}$$

The weak-coupling ratio is $2\Delta_0/(k_B T_c) = 2\pi/e^\gamma \simeq 3.528$. Its assumptions include an isotropic single gap, weak coupling, and a wide cutoff window. It is not a definition satisfied by every superconductor. Expanding the integral near T_c gives

$$\Delta^2(T) \simeq \frac{8\pi^2}{7\zeta(3)} (k_B T_c)^2 (1 - T/T_c), \qquad \Delta(T) \simeq 3.06 k_B T_c \sqrt{1 - T/T_c}. \tag{10.17}$$

10.7.1 Example SC3 Self-consistent temperature dependence of the gap

Use units $\omega_D = k_B = 1$ and $\lambda = 0.30$. Integrate on $\xi \in [0, 1]$ with 12001 trapezoidal points. First bracket and bisect the critical-temperature equation; then bisect Eq. (10.14) in Δ at each $T < T_c$. The results are $T_c = 0.04044953$ and $\Delta_0 = 0.07143890$.

T/T_c	0	0.2	0.5	0.8	0.9	0.99
Δ/Δ_0	1	0.999878	0.957004	0.711337	0.526620	0.173064

The finite-cutoff ratio is 3.53225, slightly different from the strict weak-coupling limit. With $\omega_D = 20\,\text{meV}$, $k_B T_c = 0.80899\,\text{meV}$ and $T_c \simeq 9.388\,\text{K}$. At $\Delta = \xi = 0$, implement the removable limit $\tanh(E/2T)/E \to 1/(2T)$ rather than assigning zero.

Three useful checks are grid convergence, recovery of the exact zero-temperature gap, and absence of a positive root for $T \geq T_c$. Fixed-point iteration can be slow near criticality; a bracketed scalar root is more robust. The interpolation $\Delta(T)/\Delta_0 \approx \tanh[1.74\sqrt{T_c/T - 1}]$ is convenient for sketches, but the table was obtained from the integral equation, not from that interpolation.

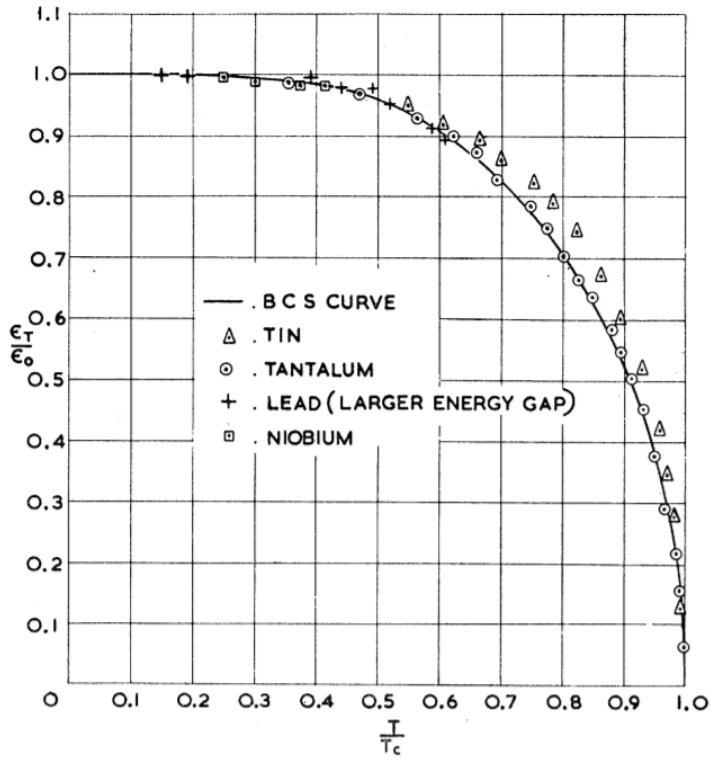

Figure 10.1: Normalized superconducting gaps $\Delta(T)/\Delta(0)$ versus T/T_c inferred from tunnelling measurements; the plotted ordinate is labelled ϵ_T/ϵ_0. Triangles, circles, crosses and squares denote the experimental results for Sn, Ta, Pb (the larger gap) and Nb, respectively; the solid line is the BCS temperature-dependence curve. Source: P. Townsend and J. Sutton, Physical Review **128**, 591 (1962).[60]

Figure 10.1 connects this theory to experiment. Each axis is normalized by the material's own T_c and zero-temperature gap. The comparison tests the shape of the temperature dependence, not equality of absolute gaps. The nearly constant low-temperature gap and its rapid closing near T_c agree qualitatively with the finite-temperature self-consistency equation; sufficiently close to the transition one can test $\Delta(T) \propto \sqrt{1 - T/T_c}$. Extracting a gap from a tunnelling current requires a junction model including the two electrodes' densities of states and thermal occupations. The Pb label explicitly selects its larger gap.

Deviations should therefore not all be dismissed as measurement noise, and agreement after normalization does not establish the weak-coupling ratio $2\Delta(0)/(k_B T_c) = 3.53$ in every material.

10.8 Free energy and thermodynamic checks

With the present conventions, the grand potential is

$$\Omega = \mathcal{V}\frac{|\Delta|^2}{g} + \sum_{\mathbf{k}}(\xi_{\mathbf{k}} - E_{\mathbf{k}}) - 2k_B T \sum_{\mathbf{k}} \ln(1 + e^{-E_{\mathbf{k}}/k_B T}). \tag{10.18}$$

Its stationarity condition reproduces the gap equation. Compare $F = \Omega + \mu N$ between states at the same density, and Ω between states at the same chemical potential. This distinction also applies to magnetic Hartree–Fock calculations.

The zero-temperature condensation energy density follows by integration:

$$f_s - f_n = \nu_0 \omega_D \left[\omega_D - \sqrt{\omega_D^2 + \Delta_0^2}\right] \simeq -\tfrac{1}{2}\nu_0 \Delta_0^2. \tag{10.19}$$

It determines the thermodynamic critical field through $B_c^2/(2\mu_0) = f_n - f_s$, where $B_c = \mu_0 H_c$. Mixing this SI expression with the Gaussian expression $H_c^2/(8\pi)$ leads to inconsistent numerical values.

The electronic entropy and heat capacity are

$$S = -2k_B \sum_{\mathbf{k}} \{f \ln f + (1-f)\ln(1-f)\}, \qquad C = T\frac{dS}{dT}. \tag{10.20}$$

The derivative includes the temperature dependence of Δ. Differentiating only the Fermi function at fixed gap misses the heat-capacity discontinuity. The isotropic weak-coupling result is $\Delta C/(\gamma T_c) = 12/[7\zeta(3)] \simeq 1.426$. For a numerical check, use one-sided derivatives near T_c; a wide finite difference crossing the transition smooths the discontinuity artificially.

Figure 10.2 connects this theory to experiment. The field provides a normal-state comparison over the same temperature range. Fit $C_n = \gamma T + \beta T^3$ to separate electronic and lattice terms, then compare the two branches at the same temperature. Weak-coupling isotropic BCS theory predicts $\Delta C/(\gamma T_c) \simeq 1.43$: the normalization is the electronic coefficient, not the total normal-state heat capacity including phonons. Heat capacity supplies bulk thermodynamic evidence complementary to zero resistance and tunnelling gaps. Phillips also reported low-temperature departures from a simple exponential extrapolation. The discontinuity should therefore not be interpreted as perfect agreement with one exponential law across the entire temperature range; low-energy conclusions require controlled backgrounds and a stated fitting interval.

10.8.1 Example SC4 From a gap to condensation energy and critical field

Take the illustrative single-spin density of states $\nu_0 = 10^{47}\,\mathrm{J^{-1}m^{-3}}$ and $\Delta_0 = 1\,\mathrm{meV}$. The condensation energy is approximately $1.2835 \times 10^3\,\mathrm{J\,m^{-3}}$, yielding $B_c \simeq 0.0568\,\mathrm{T}$. Inserting a two-spin density of states into the single-spin formula doubles the energy and multiplies the field by $\sqrt{2}$. This is a sensitive counting check that dimensional analysis alone cannot provide.

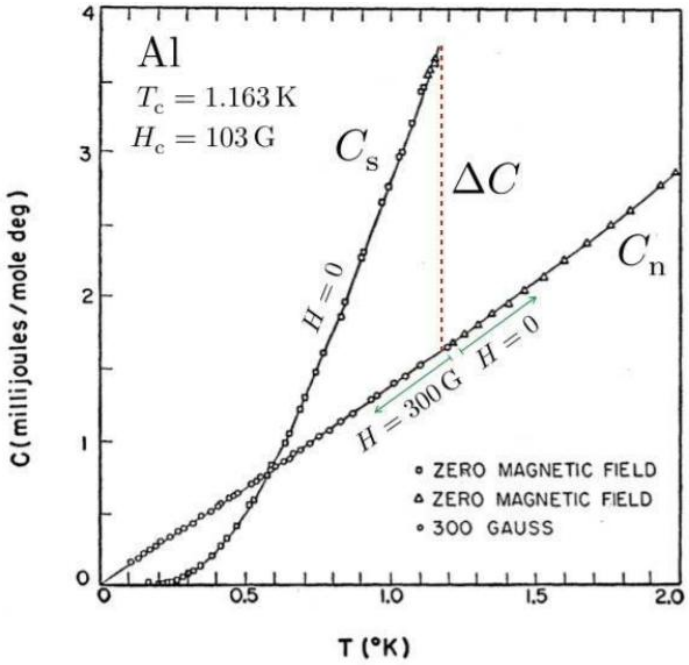

Figure 10.2: Molar heat capacity of aluminum versus temperature. Symbols are measurements in zero magnetic field and at 300 G, the latter suppressing superconductivity. Curves identify the superconducting branch C_s, the normal branch C_n, and the discontinuity ΔC near $T_c = 1.163$ K. The stated zero-temperature critical field is about 103 G. Source: N. E. Phillips, Physical Review **114**, 676 (1959).[62]

10.9 Density of states and tunnelling coherence peaks

Changing variables from ξ to $E = \sqrt{\xi^2 + \Delta^2}$ gives

$$\frac{\nu_s(E)}{\nu_n(0)} = \mathrm{Re}\,\frac{|E|}{\sqrt{E^2 - \Delta^2}}. \tag{10.21}$$

Use the same spin counting in numerator and denominator. The ideal coherence peak has a square-root singularity at $|E| = \Delta$. Temperature, lifetime, inhomogeneity, and instrumental resolution broaden it. In the weak-tunnelling limit of a normal-metal–superconductor junction,

$$\frac{dI}{dV} \propto \int dE\, \nu_s(E) \left[-\frac{\partial f(E - eV)}{\partial E} \right]. \tag{10.22}$$

Only at sufficiently low temperature and approximately constant normal-electrode density of states does dI/dV closely trace $\nu_s(eV)$. Tunnelling matrix elements also select parts of momentum space. A V-shaped spectrum alone does not uniquely identify a pairing representation.

10.10 The attractive Hubbard model on a lattice band

10.10.1 Model and Hartree shift

Consider the square-lattice Hamiltonian

$$H = -t \sum_{\langle ij \rangle \sigma} (c^\dagger_{i\sigma} c_{j\sigma} + \mathrm{h.c.}) - U \sum_i n_{i\uparrow} n_{i\downarrow} - \mu \sum_i n_i, \qquad U > 0. \tag{10.23}$$

For a uniform nonmagnetic solution, $\Delta = U\langle c_{i\downarrow}c_{i\uparrow}\rangle$ and the Hartree term produces $\widetilde{\mu} = \mu + Un/2$. With $\varepsilon_{\mathbf{k}} = -2t(\cos k_x + \cos k_y)$, write $\xi_{\mathbf{k}} = \varepsilon_{\mathbf{k}} - \widetilde{\mu}$. The whole lattice band participates when no phonon cutoff is imposed:

$$1 = \frac{U}{N_k}\sum_{\mathbf{k}} \frac{\tanh(E_{\mathbf{k}}/2T)}{2E_{\mathbf{k}}}, \quad n = \frac{1}{N_k}\sum_{\mathbf{k}}\left[1 - \frac{\xi_{\mathbf{k}}}{E_{\mathbf{k}}}\tanh\frac{E_{\mathbf{k}}}{2T}\right]. \tag{10.24}$$

Here $k_B = 1$. The constant-density-of-states integral is a low-energy approximation to these band equations. A van Hove singularity can invalidate that approximation.

10.10.2 Example SC5 Fixing density while solving for the gap

Take $t = 1$, $U = 3$, $n = 0.8$, and $T = 0.05$. Use a midpoint grid on $[-\pi, \pi)^2$. An outer bisection adjusts $\widetilde{\mu}$ to the target density, while an inner bisection finds the nonzero gap. The result is

$$\widetilde{\mu} = -0.55525120, \qquad \Delta = 0.80112295, \qquad \mu = \widetilde{\mu} - Un/2 = -1.75525120. \tag{10.25}$$

Grids of 100, 200, and 300 points in each direction agree to the eight decimal places shown; the computed density is 0.80000000. Do not confuse effective and bare chemical potentials. Although the shifted quantity enters the quasiparticle matrix, the distinction matters in the full free energy. This calculation restricts the solution to uniform pairing and does not prove global stability against every competing order. In a strictly two-dimensional short-range model, finite-temperature phase fluctuations and the Berezinskii–Kosterlitz–Thouless transition lie beyond this mean-field pairing scale.

10.11 Inhomogeneous Bogoliubov–de Gennes calculations

Boundaries, disorder, and vortices produce spatially varying Δ_i and n_i. For a simplified spin-degenerate block without magnetic fields,

$$\sum_j \begin{pmatrix} h_{ij} & -\Delta_i\delta_{ij} \\ -\Delta_i^*\delta_{ij} & -h_{ij}^* \end{pmatrix} \begin{pmatrix} u_{jn} \\ w_{jn} \end{pmatrix} = E_n \begin{pmatrix} u_{in} \\ w_{in} \end{pmatrix}. \tag{10.26}$$

With our $-\Delta$ off-diagonal convention, the positive-energy eigenvectors obey the self-consistency relations

$$\Delta_i = -U_i \sum_{E_n>0} u_{in}w_{in}^* \tanh\frac{E_n}{2T}, \quad n_i = 2\sum_{E_n>0}\left[|u_{in}|^2 f(E_n) + |w_{in}|^2(1 - f(E_n))\right]. \tag{10.27}$$

If the off-diagonal convention is changed to $+\Delta$, adjust the anomalous-average convention as well. Mixing one equation from each convention introduces a spurious sign error.

The computational cycle is: initialize Δ_i, n_i, μ; construct and diagonalize the matrix; calculate updated averages; mix, for example with $\Delta_i \leftarrow (1-\eta)\Delta_i + \eta\Delta_i^{\text{new}}$; adjust μ if density is fixed; and repeat until residuals are small. Start from several initial configurations to detect metastability. Vortex phase winding, magnetic flux, and hopping Peierls phases must be mutually consistent. If a large adjacent superconductor imposes the pair potential, Δ_i may be treated as an input; the calculation then determines an effective BdG spectrum rather than a self-consistent order parameter.

10.11.1 Limits of the nonmagnetic-disorder argument

For isotropic s-wave pairing, preserved time reversal, weak changes in the normal density of states, and no strong localization, pairing between time-reversed disordered eigenstates explains the weak sensitivity of T_c

to nonmagnetic scattering. Magnetic impurities disrupt this relation. A sign-changing gap can also be suppressed by nonmagnetic scattering that connects regions of opposite sign. The statement that nonmagnetic impurities never affect superconductivity is too broad.

10.12 Microscopic-superconductivity exercises and solution notes

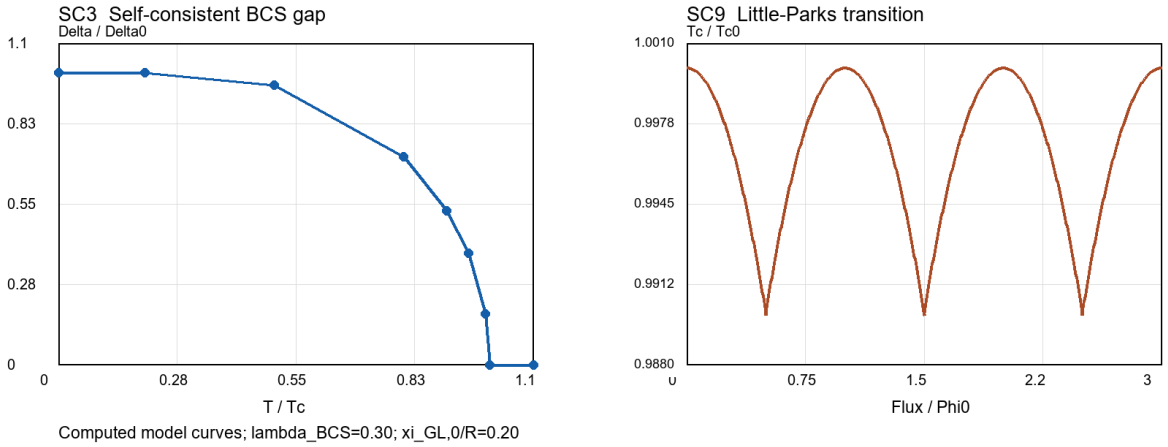

Figure 10.3: Left: the self-consistent integration results of SC3, with a guide to the eye. Right: the Little–Parks model developed in SC9. Thermal gap suppression and the winding-induced transition-temperature oscillation describe different self-consistency and phase effects. Both plots are model calculations at the stated parameters.

1. Reduce the SC1 coupling to $\lambda = 0.15$ and compare E_b with Δ_0. The exponents are $-2/\lambda$ and $-1/\lambda$; retain the distinct integration intervals before taking weak-coupling limits.
2. Use the SC3 solver at $\lambda = 0.2$ to show that $2\Delta_0/T_c$ approaches 3.528. Refine the grid to distinguish integration error from finite-cutoff corrections.
3. Repeat SC5 at fixed bare μ instead of fixed n and plot $n(T)$. Explain why this is a different thermodynamic constraint.
4. In a real-space BdG calculation, set $U_i = 0$ on several middle sites. Does the anomalous expectation value immediately vanish there? No: zero local attraction and zero proximity-induced pair correlation are different statements.

BCS microscopic theory provides a unified self-consistent description of interaction-induced pairing, quasiparticle spectra, and thermodynamic properties[43].

10.13 Superconducting electrodynamics and Ginzburg–Landau theory

The electromagnetic response of a superconductor depends on the amplitude and phase of its order parameter and their coupling to electromagnetic fields. London theory describes screening at approximately fixed amplitude, whereas Ginzburg–Landau theory permits spatial variations of both amplitude and phase, yielding

critical fields, depairing currents, and flux interference. In SI units, we use $e > 0$, pair charge $q = -2e$, effective pair-field mass m_*, and pair-density normalization $|\psi|^2$. In a lattice, m_* and the stiffness are effective parameters, not necessarily twice the vacuum electron mass.

10.13.1 London equations and the half-space solution

For a local response with uniform superfluid density,

$$\frac{\partial \mathbf{j}_s}{\partial t} = \frac{n_s e^2}{m}\mathbf{E}, \qquad \nabla \times \mathbf{j}_s = -\frac{n_s e^2}{m}\mathbf{B}, \qquad \lambda_L^2 = \frac{m}{\mu_0 n_s e^2}. \tag{10.28}$$

Here n_s counts superfluid *electrons*; the pair density is $|\psi|^2 = n_s/2$. Taking a curl of Ampère's law and using $\nabla \cdot \mathbf{B} = 0$ yields

$$-\nabla^2 \mathbf{B} = \mu_0 \nabla \times \mathbf{j}_s = -\mathbf{B}/\lambda_L^2, \qquad \nabla^2 \mathbf{B} = \mathbf{B}/\lambda_L^2. \tag{10.29}$$

The positive sign on the right produces exponential screening rather than oscillation. A superconductor occupying $x > 0$ with $B_z(0) = B_0$ has $B_z(x) = B_0 e^{-x/\lambda_L}$ and $j_y = -\partial_x B_z/\mu_0 = B_0 e^{-x/\lambda_L}/(\mu_0 \lambda_L)$.

Example SC6 Screening length and surface current

For $n_s = 5 \times 10^{28}\,\mathrm{m}^{-3}$ and $m = m_e$, $\lambda_L = 23.765\,\mathrm{nm}$. A surface field $B_0 = 1\,\mathrm{mT}$ gives $j_y(0) \simeq 3.35 \times 10^{10}\,\mathrm{A\,m}^{-2}$. At $3\lambda_L$, 4.98% of the surface field remains. The integrated current $\int_0^\infty j_y dx = B_0/\mu_0$ agrees with Ampère's law. This example assumes a bare-mass ideal electron gas. Band mass, stiffness, disorder, and temperature alter the penetration depth of a real material.

10.13.2 The gauge-covariant GL functional

$$F = \int d^3r \left[f_n + \alpha|\psi|^2 + \frac{\beta}{2}|\psi|^4 + \frac{1}{2m_*}|(-i\hbar\nabla - q\mathbf{A})\psi|^2 + \frac{B^2}{2\mu_0} \right], \quad \beta > 0. \tag{10.30}$$

Usually $\alpha = \alpha_0(T - T_c)$. The transformations $\mathbf{A} \to \mathbf{A} + \nabla\chi$ and $\psi \to e^{iq\chi/\hbar}\psi$ preserve gauge covariance of the kinetic term. Writing $\psi = |\psi|e^{i\theta}$ separates amplitude gradients from

$$\frac{|\psi|^2}{2m_*}(\hbar\nabla\theta - q\mathbf{A})^2. \tag{10.31}$$

The observable combination involves both phase gradient and vector potential. An $\mathbf{A}^2$ term in a chosen gauge should not be interpreted as a failure of gauge invariance. Phase stiffness coupled to electromagnetism gives Meissner screening; longitudinal phase dynamics is related to the plasma response of the charged system. This is the relevant Anderson–Higgs connection.

Variation and boundary conditions

Variation with respect to ψ^*, including integration by parts, gives

$$\alpha\psi + \beta|\psi|^2\psi + \frac{1}{2m_*}(-i\hbar\nabla - q\mathbf{A})^2\psi = 0. \tag{10.32}$$

Variation with respect to $\mathbf{A}$ gives

$$\mathbf{j}_s = \frac{q}{m_*}\,\mathrm{Re}[\psi^*(-i\hbar\nabla - q\mathbf{A})\psi] = \frac{q}{m_*}|\psi|^2(\hbar\nabla\theta - q\mathbf{A}). \tag{10.33}$$

The natural insulating boundary condition is $\mathbf{n}\cdot(-i\hbar\nabla - q\mathbf{A})\psi = 0$, which prohibits current through the boundary. Surface pair breaking requires a modified condition with an extrapolation length. Derivation from BCS assumes proximity to T_c and slow variation of the order parameter. Its critical formulas should not be extrapolated indiscriminately to zero temperature and strong fields.

10.13.3 Two lengths and the condensation energy

The uniform zero-field minimum is $|\psi_\infty|^2 = -\alpha/\beta$. Define

$$\xi^2 = \frac{\hbar^2}{2m_*|\alpha|}, \qquad \lambda^2 = \frac{m_*}{\mu_0 q^2|\psi_\infty|^2}, \qquad \kappa = \lambda/\xi. \tag{10.34}$$

The condensation energy is $-\alpha^2/(2\beta)$, hence

$$B_c = \frac{\Phi_0}{2\sqrt{2}\pi\lambda\xi}, \qquad \Phi_0 = \frac{h}{2e}. \tag{10.35}$$

At zero field write $\psi = \psi_\infty f(x)$, giving $\xi^2 f'' + f - f^3 = 0$. A fully pair-suppressing planar boundary with $f(0) = 0$ and $f(\infty) = 1$ has solution $f = \tanh[x/(\sqrt{2}\xi)]$. Far from the boundary the deviation decays as $e^{-\sqrt{2}x/\xi}$. Thus the GL parameter ξ differs by a numerical factor from this particular recovery length. It should also be distinguished from the weak-coupling zero-temperature pair-size estimate $\xi_0 = \hbar v_F/(\pi\Delta_0)$.

10.13.4 Deriving the upper critical field from Landau levels

At nucleation from the normal state, ψ is small and the cubic term can be neglected. For a uniform field $B\hat{z}$ and $A_y = Bx$, the linearized GL operator is a Landau-level problem for charge magnitude $|q| = 2e$. Taking $\psi = e^{ik_y y + ik_z z} f(x)$ gives kinetic eigenvalues

$$\epsilon_{n,k_z} = \hbar\frac{|q|B}{m_*}(n + \tfrac{1}{2}) + \frac{\hbar^2 k_z^2}{2m_*}. \tag{10.36}$$

The lowest eigenvalue must not exceed $|\alpha|$. The first nucleating solution has $n = 0, k_z = 0$, so

$$B_{c2} = \frac{2m_*|\alpha|}{\hbar|q|} = \frac{\Phi_0}{2\pi\xi^2} = \sqrt{2}\kappa B_c. \tag{10.37}$$

Here B is magnetic induction and the answer is in tesla. The linearized equation determines the onset, not the amplitude and full structure of a vortex lattice. The quartic term is needed for the latter.

Example SC7 Estimating three critical fields

At a fixed temperature let $\lambda = 150\,\text{nm}$ and $\xi = 10\,\text{nm}$. Then $\kappa = 15$, $B_c = 0.15514\,\text{T}$, and $B_{c2} = 3.29106\,\text{T}$. For $\kappa \gg 1$,

$$B_{c1} \simeq \frac{\Phi_0}{4\pi\lambda^2}(\ln\kappa + 0.5) = 0.02346\,\text{T}. \tag{10.38}$$

The additive 0.5 is a commonly used large-κ core correction, not an exact expression at every κ. The GL distinction between type I and type II occurs at $\kappa = 1/\sqrt{2}$. Pauli limiting or strong multiband effects can invalidate the simple orbital single-band estimate of B_{c2}.

Figure 10.4 connects this theory to experiment. Each singly quantized vortex carries $\Phi_0 = h/(2e)$. Approximating the mean induction by $B = 1\,\text{T}$ gives an areal density $n_v = B/\Phi_0 \simeq 4.84\times10^{14}\,\text{m}^{-2}$. For a triangular lattice, $\sqrt{3}a_v^2/2 = \Phi_0/B$, predicting $a_v \simeq 48.9\,\text{nm}$. This connects the image scale to a quantitative flux-quantization test. STM contrast probes a local tunnelling response rather than magnetic flux density directly. Identifying vortex-core states requires comparison of spectra at different biases; a periodic vortex image alone cannot establish a topological origin for a zero-energy spectral feature.

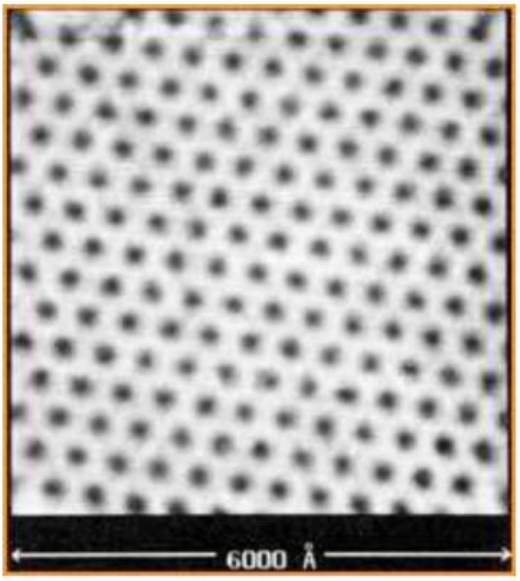

Figure 10.4: Scanning-tunnelling image of the Abrikosov vortex lattice in $NbSe_2$ at an applied field of approximately $1\,\mathrm{T}$ and $T = 1.8\,\mathrm{K}$. The scale bar is $6000\,\text{Å} = 600\,\mathrm{nm}$. Spatial contrast in the gap-edge tunnelling response reveals an approximately triangular vortex array. Source: H. F. Hess et al., Physical Review Letters **62**, 214–216 (1989).[61]

10.13.5 Superflow and suppression of the order parameter

For a thin uniform wire with negligible self-field, define mechanical velocity by $m_*\mathbf{v}_s = \hbar\nabla\theta - q\mathbf{A}$. At fixed velocity,

$$f - f_n = \left(\alpha + \tfrac{1}{2}m_* v_s^2\right)|\psi|^2 + \frac{\beta}{2}|\psi|^4. \tag{10.39}$$

The kinetic energy multiplies $|\psi|^2$, not $|\psi|^4$. Minimizing gives

$$|\psi|^2 = |\psi_\infty|^2(1 - Q^2), \quad Q = \frac{m_*\xi v_s}{\hbar}, \quad |j_s| = \frac{|q|\hbar|\psi_\infty|^2}{m_*\xi}Q(1 - Q^2). \tag{10.40}$$

The current reaches its maximum at $Q = 1/\sqrt{3}$, when the pair density remains $2/3$ of its zero-current value. The GL depairing current density is

$$j_d = \left(\frac{2}{3}\right)^{3/2}\frac{B_c}{\mu_0\lambda}. \tag{10.41}$$

Example SC8 Depairing current versus a measured critical current

Using SC7 parameters yields $j_d = 4.4801 \times 10^{11}\,\mathrm{A\,m^{-2}}$. An ideal uniform cross-section of $100\,\mathrm{nm} \times 20\,\mathrm{nm}$ would carry $I_d \simeq 0.896\,\mathrm{mA}$. Real devices can develop voltage earlier through weak links, vortex entry, phase slips, thermal instability, or current crowding. The calculation is the depairing limit of a specific uniform GL model, not a substitute for an engineering critical-current measurement.

10.13.6 Fluxoid quantization and Little Parks oscillations

Single-valuedness requires $\oint \nabla\theta \cdot d\mathbf{l} = 2\pi n$. Integrating the gauge-invariant momentum and using the current relation gives

$$\Phi + \mu_0\lambda^2 \oint \mathbf{j}_s \cdot d\mathbf{l} = n\Phi_0, \qquad \Phi_0 = 2.067833848 \times 10^{-15}\,\mathrm{Wb}. \tag{10.42}$$

The sign of n can be changed with the loop orientation. Strictly, the quantized quantity is the fluxoid. The flux itself approaches an integer flux quantum when the path lies deep inside a thick superconductor and the current contribution is negligible.

For a thin ring of radius R, neglect self-inductance and assume a uniform amplitude. The kinetic energy per pair is $\hbar^2(n - \Phi/\Phi_0)^2/(2m_*R^2)$. Requiring the linear GL coefficient plus this kinetic term to vanish gives

$$\frac{T_c(\Phi)}{T_{c0}} = 1 - \frac{\xi_{\mathrm{GL},0}^2}{R^2} \min_{n\in\mathbb{Z}} \left(n - \frac{\Phi}{\Phi_0}\right)^2, \qquad \xi_{\mathrm{GL},0}^2 = \frac{\hbar^2}{2m_*\alpha_0 T_{c0}}. \tag{10.43}$$

The parameter $\xi_{\mathrm{GL},0}$ is defined from the temperature coefficient. It is not the divergent $\xi(T_c)$ inserted into the formula.

Example SC9 Period and amplitude of Little–Parks oscillations

For $R = 500\,\mathrm{nm}$, the field period is $\Delta B = \Phi_0/(\pi R^2) = 2.63285\,\mathrm{mT}$. If $\xi_{\mathrm{GL},0} = 100\,\mathrm{nm}$ and $T_{c0} = 1.2\,\mathrm{K}$, the maximum suppression at half-integer flux is $T_{c0}\xi_{\mathrm{GL},0}^2/(4R^2) = 0.012\,\mathrm{K}$. Resolving the oscillation requires roughly millitesla field resolution and temperature sensitivity better than 12 millikelvin. Ring width, thickness, inductance, and inhomogeneity modify this ideal estimate.

10.13.7 The Josephson effect and superconducting interference

For two weakly coupled condensates, take the junction energy $E_J(1-\cos\varphi)$, where φ is the gauge-invariant phase difference. Its derivative gives

$$I = I_c \sin\varphi, \quad I_c = \frac{2eE_J}{\hbar}, \qquad \hbar\dot{\varphi} = 2eV. \tag{10.44}$$

Voltage and phase-difference orientations must be defined consistently; the magnitude of the oscillation frequency is $f_J = 2e|V|/h$. These are coherent pair relations and do not contradict the quasiparticle thresholds discussed above[44].

Example SC10 Microwave frequencies and SQUID interference

A voltage $V = 10\,\mu\mathrm{V}$ produces $f_J = 4.83598\,\mathrm{GHz}$. Irradiation at $10\,\mathrm{GHz}$ gives the first Shapiro voltage $hf/(2e) = 20.6783\,\mu\mathrm{V}$. In a symmetric two-junction SQUID with negligible self-inductance, $\varphi_2 - \varphi_1 = 2\pi\Phi/\Phi_0$. Adding the two sinusoidal currents gives

$$I_c^{\mathrm{SQUID}}(\Phi) = 2I_c \left|\cos\frac{\pi\Phi}{\Phi_0}\right|. \tag{10.45}$$

For unequal junctions the expression becomes $\sqrt{I_{c1}^2 + I_{c2}^2 + 2I_{c1}I_{c2}\cos(2\pi\Phi/\Phi_0)}$, so the minima need not vanish. This distinguishes phase interference from a simple field-induced reduction of the pairing amplitude.

10.13.8 Superconducting-electrodynamics exercises and solution notes

1. Integrate the London half-space current and check the boundary discontinuity of the field. Distinguish current density from integrated current per unit length.
2. Halve ξ in SC7 at fixed λ. Then B_{c2} increases fourfold, B_c doubles, and κ doubles; B_{c1} changes only logarithmically through κ.
3. Double the SC9 ring radius. Both the field period and the temperature-oscillation amplitude decrease by a factor of four. Explain why a larger ring is not necessarily easier to measure.
4. Set $I_{c2} = 0.6 I_{c1}$ in SC10. The maximum and minimum are $1.6 I_{c1}$ and $0.4 I_{c1}$; a nonzero minimum does not imply loss of flux coherence.

Chapter 11

Unconventional pairing and topological superconductivity

The term unconventional needs a stated criterion. It may describe a nontrivial crystal-symmetry representation, a sign change between Fermi surfaces, or a pairing mechanism beyond a simple phonon weak-coupling model. These meanings are not equivalent. Nodes do not automatically imply topological superconductivity, and a full gap does not automatically imply ordinary s-wave pairing. Pairing-kernel eigenvectors, nodal structure, and BdG invariants provide quantitative criteria for these distinctions; interpretation in materials also requires phase-sensitive evidence.

11.1 Antisymmetry and the pairing matrix

For even-frequency, equal-time pairing, fermionic antisymmetry requires

$$\Delta_{\alpha\beta}(\mathbf{k}) = -\Delta_{\beta\alpha}(-\mathbf{k}), \qquad \widehat{\Delta}(\mathbf{k}) = [\psi(\mathbf{k}) + \mathbf{d}(\mathbf{k}) \cdot \boldsymbol{\sigma}] i\sigma_y. \tag{11.1}$$

Thus the singlet scalar obeys $\psi(-\mathbf{k}) = \psi(\mathbf{k})$ and the triplet vector obeys $\mathbf{d}(-\mathbf{k}) = -\mathbf{d}(\mathbf{k})$. Orbital indices must also be exchanged in a multiorbital problem. With strong spin-orbit coupling, classification often uses Kramers pseudospin. Without inversion, singlet and triplet components may mix; the simple pure-spin versus pure-parity correspondence cannot be applied mechanically.

In a single-band tetragonal D_{4h} example, A_{1g} includes a constant or $\cos k_x + \cos k_y$, B_{1g} includes $\cos k_x - \cos k_y$, and B_{2g} includes $\sin k_x \sin k_y$. An irreducible representation fixes transformation properties, not the nodes by itself. Nodes occur where $\Delta(\mathbf{k}) = 0$ intersects the actual Fermi surface. Even an A_{1g} function can have accidental nodes for some parameters.

11.2 Pairing as an eigenvalue problem

The linearized gap equation is

$$\Delta_{a\mathbf{k}} = -\sum_{b\mathbf{k}'} V_{ab}(\mathbf{k}, \mathbf{k}') \frac{\tanh(\xi_{b\mathbf{k}'}/2T)}{2\xi_{b\mathbf{k}'}} \Delta_{b\mathbf{k}'}. \tag{11.2}$$

After extracting the radial energy logarithm $L(T) = \ln(1.13\omega_c/T)$, discretization on the Fermi surface produces $\lambda_{\text{pair}}\Delta = -Vw\Delta$. The largest positive eigenvalue determines the first instability. The weights w include the surface measure and $1/|\mathbf{v}_F|$. An unweighted sum over unevenly spaced points incorrectly emphasizes densely sampled regions.

A repulsive kernel can have a positive pairing eigenvalue on a sign-changing function. If its dominant momentum transfer is $\mathbf{Q}$ and $\Delta(\mathbf{k}+\mathbf{Q}) = -\Delta(\mathbf{k})$, the minus sign in the gap equation converts repulsion into enhancement in that channel. This algebra does not by itself establish spin-fluctuation pairing in a particular material. Real interactions, orbital matrix elements, and experimental constraints remain necessary.

11.2.1 Example SC11 Sign-changing pairing on two pockets

Consider two equal-density-of-states pockets with only interband repulsion $V_{12} = V_{21} = V > 0$. For $\lambda = \nu V$,

$$\begin{pmatrix} \Delta_1 \\ \Delta_2 \end{pmatrix} = -\lambda L(T) \begin{pmatrix} 0 & 1 \\ 1 & 0 \end{pmatrix} \begin{pmatrix} \Delta_1 \\ \Delta_2 \end{pmatrix}. \tag{11.3}$$

The symmetric vector $(1, 1)$ has pairing eigenvalue $-\lambda$, while $(1, -1)$ has $+\lambda$. Therefore $T_c = 1.13\omega_c e^{-1/\lambda}$, even though each pocket may be fully gapped. For unequal densities the leading eigenvalue is $V\sqrt{\nu_1\nu_2}$ and $\Delta_1/\Delta_2 = -\sqrt{\nu_2/\nu_1}$. Taking $\nu_2 = 4\nu_1$ gives ratio -2. This is a minimal mathematical realization of $s_\pm$ pairing. The original iron-based proposal is Ref. [45]; Fermi surfaces and competing channels vary across that materials family.

11.3 Nodal quasiparticles and low-temperature powers

On a circular two-dimensional Fermi surface, choose $\Delta(\theta) = \Delta_d \cos 2\theta$. The four nodes are at $\theta = \pi/4$, $3\pi/4$, $5\pi/4$, and $7\pi/4$. Near one node, take $q_\perp$ normal and $q_\parallel$ tangent to the Fermi surface:

$$E(\mathbf{q}) \simeq \sqrt{(\hbar v_F q_\perp)^2 + (\hbar v_\Delta q_\parallel)^2}, \qquad \hbar v_\Delta = \left| \frac{\partial \Delta}{\partial k_\parallel} \right|_{\text{node}}. \tag{11.4}$$

For each independent Dirac cone the density of states is proportional to $|E|/(2\pi\hbar^2 v_F v_\Delta)$. Count spin and node multiplicities separately. A clean two-dimensional d-wave system consequently has electronic $C \propto T^2$ and often a linear-T penetration-depth increment. Disorder, three-dimensional dispersion, nonlocal response, and multiple bands can modify the accessible power-law regime.

11.3.1 Example SC12 Locating nodes on a square lattice

Let $\xi_{\mathbf{k}} = -2t(\cos k_x + \cos k_y) - \mu$ and $\Delta_{\mathbf{k}} = \Delta_d(\cos k_x - \cos k_y)$, with $t = 1$, $\mu = -1$, and $\Delta_d = 0.2$. Along $k_x = k_y = k_N$, the Fermi-surface condition is $-4\cos k_N + 1 = 0$, giving $k_N = \arccos(1/4) = 1.318116$. The normal band slope is $\hbar v_F = 2\sqrt{2}t \sin k_N = 2.738613$, and the tangential gap slope is $\hbar v_\Delta = \sqrt{2}\Delta_d \sin k_N = 0.273861$. Their ratio is 10. Constant-energy contours are elongated ellipses rather than circles. This provides a direct test of whether a numerical calculation has assigned the local normal and tangent directions correctly.

11.4 Phase-sensitive evidence and interpretation in materials

Heat capacity and tunnelling often reveal low-energy excitations but do not directly measure the *sign* of a gap. Josephson coupling is phase-sensitive, so loops involving different crystallographic orientations can test sign changes. Tricrystal YBCO experiments observed half-flux behavior consistent with d-wave symmetry[46]. Such evidence should be combined with nodal power laws and momentum-resolved spectra. An arbitrary half-flux signal is not automatically evidence for the same pairing state.

A loop with an odd number of effective π junctions obeys a closure condition of the form

$$2\pi\Phi/\Phi_0 + \sum_j \varphi_j + \pi = 2\pi n. \tag{11.5}$$

In an ideal strong-screening limit with small remaining junction phase deviations, the minimum approaches $\Phi = (n + 1/2)\Phi_0$. Finite inductance and junction energy shift the spontaneous flux from exactly half a quantum. The experiment tests phase frustration around a closed path; it does not change the Cooper-pair charge to $4e$.

Heavy-fermion compounds, ruthenates, and other candidates illustrate diverse possibilities. Calling a material unconventional does not uniquely specify its pairing representation. In particular, Sr_2RuO_4 should not be presented as an established chiral p-wave example. The spin-susceptibility reduction in oxygen NMR constrained earlier simple equal-spin chiral interpretations[47]. The p-wave models below are theoretical examples, not an identification of that material.

11.5 BdG wavefunctions and topological classification

A BdG Hamiltonian with a specified pairing field has particle–hole redundancy. In a spinless Nambu basis $(c_k, c_{-k}^\dagger)$, $\mathcal{C} = \tau_x K$ obeys

$$\mathcal{C}\mathcal{H}(k)\mathcal{C}^{-1} = -\mathcal{H}(-k), \qquad \mathcal{C}^2 = +1, \tag{11.6}$$

where K is complex conjugation. It relates $+E$ and $-E$ states. A localized zero-energy state that can be chosen self-conjugate corresponds to a Majorana zero mode. A generic finite-energy Bogoliubov excitation is not itself an isolated Majorana zero mode.

A topological invariant cannot change continuously while the bulk remains gapped and its protecting symmetries remain intact. A common one-dimensional superconducting system without additional symmetries is in class D and has a $\mathbb{Z}_2$ distinction; two-dimensional class D has an integer Chern number. Time reversal squaring to -1 can produce class DIII and Kramers-paired boundary modes. A real-parameter Kitaev chain has an additional effective symmetry allowing a BDI description; that extra integer classification does not survive every allowed class-D perturbation.

11.6 The Kitaev chain from a matrix to end modes

Take real t, Δ in

$$H = -\mu \sum_j (c_j^\dagger c_j - \tfrac{1}{2}) - t \sum_j (c_j^\dagger c_{j+1} + \text{h.c.}) + \sum_j (\Delta c_j c_{j+1} + \text{h.c.}). \tag{11.7}$$

With a consistent phase convention its Bloch matrix and spectrum are

$$\mathcal{H}(k) = (-\mu - 2t\cos k)\tau_z + 2\Delta \sin k\, \tau_y, \qquad E_\pm(k) = \pm\sqrt{(\mu + 2t\cos k)^2 + 4\Delta^2 \sin^2 k}. \tag{11.8}$$

For $\Delta \neq 0$, gap closings occur only at $k = 0, \pi$ and $\mu = \mp 2t$. The product of endpoint masses gives

$$\mathcal{M} = \text{sgn}[(-\mu - 2t)(-\mu + 2t)] = \text{sgn}(\mu^2 - 4t^2). \tag{11.9}$$

Our convention assigns $\mathcal{M} = -1$ to the topological region $|\mu| < 2|t|$.

At $\mu = 0, \Delta = t$, write $c_j = (a_j + ib_j)/2$, with $a_j^\dagger = a_j$ and $b_j^\dagger = b_j$. The Hamiltonian pairs different Majorana operators on neighboring sites, leaving one unpaired operator at each end. Away from this special point the end wavefunctions decay into the bulk. Their overlap in a finite chain generally produces exponentially small splitting[48].

11.6.1 Example SC13 Open-boundary spectrum and finite-size checks

For N sites, form $h_{ii} = -\mu$, $h_{i,i+1} = h_{i+1,i} = -t$ and the antisymmetric pairing block $D_{i,i+1} = \Delta$, $D_{i+1,i} = -\Delta$. Diagonalize

$$\mathcal{H}_{\text{open}} = \begin{pmatrix} h & D \\ -D & -h \end{pmatrix}. \tag{11.10}$$

With $t = 1, \Delta = 0.6$, the smallest absolute energies are

	$N = 20$	$N = 40$	$N = 80$
$\mu = 0.5$	1.31×10^{-6}	1.20×10^{-12}	$< 10^{-14}$
$\mu = 3.0$	1.034817	1.009610	1.002525

For the topological parameters, the probability averaged over the two closest-to-zero states has approximately 99.903% of its weight on the first and last five sites combined. In the trivial case the lowest excitation approaches the bulk gap of 1. A result below numerical precision should be reported as numerical zero, not as a precisely measured splitting of order 10^{-17}. Eigenvectors in a nearly degenerate subspace can rotate arbitrarily; a single computed vector can occupy both ends. Inspecting the low-energy subspace is more reliable than selecting one vector.

The comparison checks Hermiticity, positive–negative spectral pairing, an open bulk gap, and boundary localization. A small eigenvalue alone is insufficient evidence of topology. Replacing open boundaries by periodic boundaries must remove isolated boundary zero modes even in the topological parameter range.

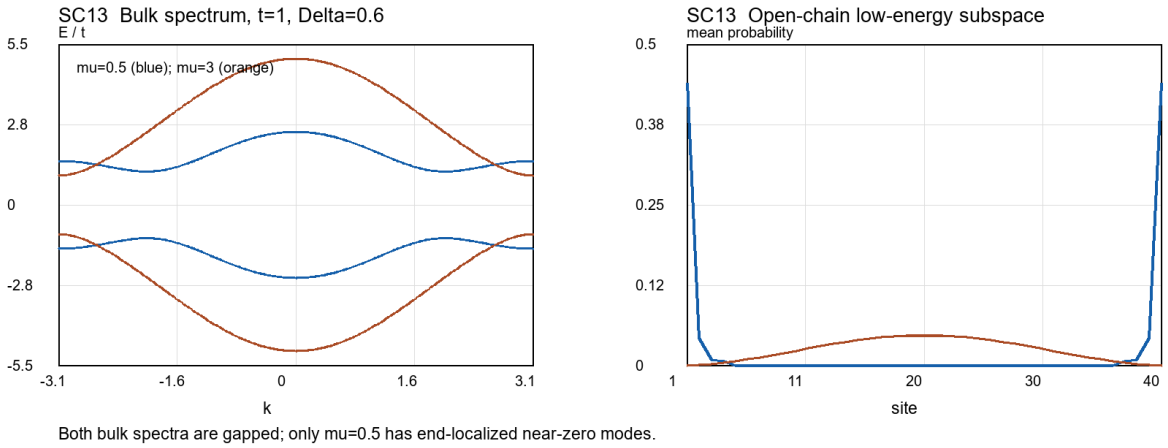

Figure 11.1: SC13: both bulk spectra are gapped. The open-chain low-energy subspace is end-localized only for the topological parameters. Averaging over its two states avoids misleading dependence on a basis choice within the nearly degenerate subspace.

11.7 Two-dimensional chiral pairing and Majorana edge transport

A continuum spinless $p_x + ip_y$ model can be written

$$\mathcal{H}(\mathbf{k}) = \Delta_p k_x \tau_x - \Delta_p k_y \tau_y + \left(\frac{\hbar^2 k^2}{2m} - \mu \right) \tau_z. \tag{11.11}$$

The quadratic high-momentum term provides ultraviolet regularization, fixing the direction of $\hat{\mathbf{d}}$ at infinity. For $\mu > 0$, the mass at the origin opposes its asymptotic value, and the map can wrap the sphere once: $|C| = 1$. For $\mu < 0$, the strong-pairing phase is trivial. Chirality and Berry-curvature conventions fix the sign of C. The gap closes at $\mu = 0$, illustrating how nonzero pairing amplitudes can belong to different topological phases[49].

A chiral Majorana edge channel gives $\kappa_{xy}/T = C\pi^2 k_B^2/(6h)$, half the thermal conductance of a complex chiral fermion with the same integer index. BdG quasiparticles do not conserve electronic charge, so the insulating relation $\sigma_{xy} = Ce^2/h$ cannot simply be copied into a superconductor. Its electrical response also involves the condensate and gauge field.

11.8 From effective models to heterostructures

11.8.1 A spin-orbit-coupled nanowire

In a common Nambu basis, the Rashba-wire model is

$$\mathcal{H}(k) = \left(\frac{\hbar^2 k^2}{2m_*} - \mu\right)\tau_z + \alpha_R k \sigma_y \tau_z + V_Z \sigma_x + \Delta \tau_x. \tag{11.12}$$

At $k = 0$ the spin-orbit term vanishes, and the eigenvalues include $\pm V_Z \pm \sqrt{\mu^2 + \Delta^2}$. The gap-closing condition is therefore $V_Z^2 = \mu^2 + \Delta^2$. In the ideal single-channel model with finite spin-orbit coupling and a gapped remaining spectrum, $V_Z > \sqrt{\mu^2 + \Delta^2}$ selects the topological branch[50]. At $\alpha_R = 0$, this inequality alone does not ensure a useful fully gapped topological phase.

11.8.2 Example SC14 The field scale of an ideal topological threshold

Take $\Delta = 0.20\,\text{meV}$, $\mu = 0.10\,\text{meV}$, and effective g factor 20. Since $V_Z = |g|\mu_B B/2$, the threshold $V_{Z,c} = 0.223607\,\text{meV}$ corresponds to $B_c^{\text{model}} \simeq 0.386\,\text{T}$. This is not a guaranteed device operating point. The parent superconductor may be suppressed first; multiple subbands, disorder, orbital effects, interface potentials, and a field-dependent induced gap all matter. The next calculation should minimize the positive spectrum over the entire momentum interval, rather than checking only the $k = 0$ mass.

11.8.3 A topological-insulator surface with proximity pairing

Spin–momentum locking on a single Dirac surface permits ordinary s-wave proximity pairing to project into an effectively spinless structure. The Fu–Kane model shows that vortices can bind Majorana zero modes under appropriate conditions[51]. The time-reversal properties of the full system differ from those of a standalone chiral p-wave band. Similar projected equations do not imply identical symmetries.

11.9 Experimental criteria for topological superconductivity

A zero-bias conductance peak is a clue, not a unique identifier. Trivial Andreev bound states, smooth confinement, and multiband mixing can also generate near-zero states or peaks[52]. A stronger analysis combines bulk gap closing and reopening, correlations between ends, gate and field dependence, finite-size splitting, nonlocal transport, and control models. Stronger claims can additionally require parity, fusion, or braiding information.

Topological criteria in a model also require independent checks. Periodic boundaries determine the bulk phase diagram, open boundaries reveal the boundary spectrum, and a local potential tests the range of stability. A trivial defect state tuned accidentally close to zero provides a useful control. The bulk invariant, response to perturbations, and finite-size scaling distinguish protected boundary zero modes from accidental low-energy states.

11.10 Unconventional and topological superconductivity: exercises

1. Add equal intraband repulsion u to SC11. For equal densities the sign-changing eigenvalue is $\nu(V-u)$, so this channel is attractive only when $V > u$.
2. Replace the SC12 gap by $\Delta_d(\cos k_x - \cos k_y) + i\Delta_s$, with $\Delta_s \neq 0$. The old nodes acquire a minimum energy $|\Delta_s|$. Explain why the complex relative phase differs from a real $s + d$ combination.
3. Set $\Delta = 0$ in SC13. Even when $|\mu| < 2t$, the chain is now a gapless metal and the gapped topological-superconductor criterion cannot be applied.
4. Increase μ in SC14 and explain why the threshold rises. Then test whether the minimum bulk gap grows monotonically above threshold; the threshold formula alone does not establish that behavior.

An effective model establishes a topological mechanism under specified assumptions. Identifying that mechanism in a candidate material requires mutually consistent evidence for its pairing structure, bulk gap, and boundary response.

Bibliography

[1] J. C. Slater and G. F. Koster, Simplified LCAO Method for the Periodic Potential Problem, Physical Review **94**, 1498–1524 (1954). https://doi.org/10.1103/PhysRev.94.1498.

[2] F. D. M. Haldane, Model for a Quantum Hall Effect without Landau Levels: Condensed-Matter Realization of the Parity Anomaly, Physical Review Letters **61**, 2015–2018 (1988). https://doi.org/10.1103/PhysRevLett.61.2015.

[3] T. Fukui, Y. Hatsugai, and H. Suzuki, Chern Numbers in Discretized Brillouin Zone: Efficient Method of Computing (Spin) Hall Conductances, Journal of the Physical Society of Japan **74**, 1674–1677 (2005). https://doi.org/10.1143/JPSJ.74.1674; https://arxiv.org/abs/cond-mat/0503172.

[4] C. L. Kane and E. J. Mele, Z_2 Topological Order and the Quantum Spin Hall Effect, Physical Review Letters **95**, 146802 (2005). https://doi.org/10.1103/PhysRevLett.95.146802.

[5] B. A. Bernevig, T. L. Hughes, and S.-C. Zhang, Quantum Spin Hall Effect and Topological Phase Transition in HgTe Quantum Wells, Science **314**, 1757–1761 (2006). https://doi.org/10.1126/science.1133734; https://arxiv.org/abs/cond-mat/0611399.

[6] L. Fu and C. L. Kane, Topological Insulators with Inversion Symmetry, Physical Review B **76**, 045302 (2007). https://doi.org/10.1103/PhysRevB.76.045302.

[7] X.-L. Qi, Y.-S. Wu, and S.-C. Zhang, Topological Quantization of the Spin Hall Effect in Two-Dimensional Paramagnetic Semiconductors, Physical Review B **74**, 085308 (2006). https://doi.org/10.1103/PhysRevB.74.085308.

[8] R. Bistritzer and A. H. MacDonald, Moiré Bands in Twisted Double-Layer Graphene, Proceedings of the National Academy of Sciences **108**, 12233–12237 (2011). https://doi.org/10.1073/pnas.1108174108.

[9] C.-Z. Chang et al., Experimental Observation of the Quantum Anomalous Hall Effect in a Magnetic Topological Insulator, Science **340**, 167–170 (2013). https://doi.org/10.1126/science.1234414.

[10] L. Fu, Topological Crystalline Insulators, Physical Review Letters **106**, 106802 (2011). https://doi.org/10.1103/PhysRevLett.106.106802.

[11] W. A. Benalcazar, B. A. Bernevig, and T. L. Hughes, Quantized Electric Multipole Insulators, Science **357**, 61–66 (2017). https://doi.org/10.1126/science.aah6442; https://arxiv.org/abs/1611.07987.

[12] R. Chen, C.-Z. Chen, J.-H. Gao, B. Zhou, and D.-H. Xu, Higher-Order Topological Insulators in Quasicrystals, Physical Review Letters **124**, 036803 (2020). https://doi.org/10.1103/PhysRevLett.124.036803; https://arxiv.org/abs/1904.09932.

[13] A. P. Schnyder, S. Ryu, A. Furusaki, and A. W. W. Ludwig, Classification of Topological Insulators and Superconductors in Three Spatial Dimensions, Physical Review B **78**, 195125 (2008). https://doi.org/10.1103/PhysRevB.78.195125; https://arxiv.org/abs/0803.2786.

[14] T. H. Hsieh, H. Lin, J. Liu, W. Duan, A. Bansil, and L. Fu, Topological Crystalline Insulators in the SnTe Material Class, Nature Communications **3**, 982 (2012). https://doi.org/10.1038/ncomms1969.

[15] G. Sundaram and Q. Niu, Wave-packet dynamics in slowly perturbed crystals: Gradient corrections and Berry-phase effects, Physical Review B **59**, 14915 (1999). https://doi.org/10.1103/PhysRevB.59.14915.

[16] D. Xiao, J. Shi and Q. Niu, Berry phase correction to electron density of states in solids, Physical Review Letters **95**, 137204 (2005). https://doi.org/10.1103/PhysRevLett.95.137204.

[17] K. Leo et al., Observation of Bloch oscillations in a semiconductor superlattice, Solid State Communications **84**, 943 (1992). https://doi.org/10.1016/0038-1098(92)90798-E.

[18] C. Waschke et al., Coherent submillimeter-wave emission from Bloch oscillations in a semiconductor superlattice, Physical Review Letters **70**, 3319 (1993). https://doi.org/10.1103/PhysRevLett.70.3319.

[19] E. H. Hwang and S. Das Sarma, Single-particle relaxation time versus transport scattering time in a two-dimensional graphene layer, Physical Review B **77**, 195412 (2008). https://doi.org/10.1103/PhysRevB.77.195412.

[20] I. Sodemann and L. Fu, Quantum nonlinear Hall effect induced by Berry curvature dipole in time-reversal invariant materials, Physical Review Letters **115**, 216806 (2015). https://doi.org/10.1103/PhysRevLett.115.216806.

[21] D. T. Son and B. Z. Spivak, Chiral anomaly and classical negative magnetoresistance of Weyl metals, Physical Review B **88**, 104412 (2013). https://doi.org/10.1103/PhysRevB.88.104412.

[22] B. Skinner and L. Fu, Large, nonsaturating thermopower in a quantizing magnetic field, Science Advances **4**, eaat2621 (2018). https://doi.org/10.1126/sciadv.aat2621.

[23] F. Han et al., Quantized thermoelectric Hall effect induces giant power factor in a topological semimetal, Nature Communications **11**, 6167 (2020). https://doi.org/10.1038/s41467-020-19850-2.

[24] R. Kubo, Statistical-Mechanical Theory of Irreversible Processes. I, Journal of the Physical Society of Japan **12**, 570 (1957). https://doi.org/10.1143/JPSJ.12.570.

[25] K. F. Mak et al., Measurement of the optical conductivity of graphene, Physical Review Letters **101**, 196405 (2008). https://doi.org/10.1103/PhysRevLett.101.196405.

[26] M. Büttiker, Four-terminal phase-coherent conductance, Physical Review Letters **57**, 1761 (1986). https://doi.org/10.1103/PhysRevLett.57.1761.

[27] J. Tworzydło et al., Sub-Poissonian shot noise in graphene, Physical Review Letters **96**, 246802 (2006). https://doi.org/10.1103/PhysRevLett.96.246802.

[28] N. D. Mermin and H. Wagner, Absence of Ferromagnetism or Antiferromagnetism in One- or Two-Dimensional Isotropic Heisenberg Models, Physical Review Letters **17**, 1133–1136 (1966). https://doi.org/10.1103/PhysRevLett.17.1133.

[29] T. Dietl, H. Ohno and F. Matsukura, Hole-mediated ferromagnetism in tetrahedrally coordinated semiconductors, Physical Review B **63**, 195205 (2001). https://doi.org/10.1103/PhysRevB.63.195205.

[30] Q.-Z. Wang, X. Liu, H.-J. Zhang, N. Samarth, S.-C. Zhang and C.-X. Liu, Quantum Anomalous Hall Effect in Magnetically Doped InAs/GaSb Quantum Wells, Physical Review Letters **113**, 147201 (2014). https://doi.org/10.1103/PhysRevLett.113.147201. Supplement: https://link.aps.org/supplemental/10.1103/PhysRevLett.113.147201.

[31] L. Šmejkal, J. Sinova and T. Jungwirth, Beyond Conventional Ferromagnetism and Antiferromagnetism: A Phase with Nonrelativistic Spin and Crystal Rotation Symmetry, Physical Review X **12**, 031042 (2022). https://doi.org/10.1103/PhysRevX.12.031042.

[32] Z. Xiao, J. Zhao, Y. Li, R. Shindou and Z.-D. Song, Spin Space Groups: Full Classification and Applications, Physical Review X **14**, 031037 (2024). https://doi.org/10.1103/PhysRevX.14.031037.

[33] Y. Jiang, Z. Song, T. Zhu, Z. Fang, H. Weng, Z.-X. Liu, J. Yang and C. Fang, Enumeration of Spin-Space Groups: Toward a Complete Description of Symmetries of Magnetic Orders, Physical Review X **14**, 031039 (2024). https://doi.org/10.1103/PhysRevX.14.031039.

[34] J. Krempaský et al., Altermagnetic lifting of Kramers spin degeneracy, Nature **626**, 517–522 (2024). https://doi.org/10.1038/s41586-023-06907-7.

[35] S. Reimers et al., Direct observation of altermagnetic band splitting in CrSb thin films, Nature Communications **15**, 2116 (2024). https://doi.org/10.1038/s41467-024-46476-5.

[36] G. Yang et al., Three-dimensional mapping of the altermagnetic spin splitting in CrSb, Nature Communications **16**, 1442 (2025). https://doi.org/10.1038/s41467-025-56647-7.

[37] J. Song et al., Absence of magnetic order and magnetic fluctuations in RuO_2, Physical Review B **112**, 144444 (2025). https://doi.org/10.1103/cb99-6thg.

[38] Y. Liu, X. Chen, Y. Yu, J. Etxebarria, J. M. Perez-Mato and Q. Liu, Symmetry classification of magnetic orders using oriented spin space groups, Nature **652**, 869–873 (2026). https://doi.org/10.1038/s41586-026-10401-1.

[39] C. Lange, R. Jaeschke-Ubiergo, A. Chakraborty, X. H. Verbeek, L. Šmejkal, J. Sinova and A. Mook, Emergent Altermagnetism at Surfaces of Antiferromagnets: Full Symmetry Classification and Material Identification, Physical Review X **16**, 031066 (2026). https://doi.org/10.1103/6j6l-kb6x.

[40] S. Zeng and Y.-J. Zhao, Description of two-dimensional altermagnetism: Categorization using spin group theory, Physical Review B **110**, 054406 (2024). https://doi.org/10.1103/PhysRevB.110.054406.

[41] J. Ye, Y. B. Kim, A. J. Millis, B. I. Shraiman, P. Majumdar and Z. Tešanović, Berry Phase Theory of the Anomalous Hall Effect: Application to Colossal Magnetoresistance Manganites, Physical Review Letters **83**, 3737–3740 (1999). https://doi.org/10.1103/PhysRevLett.83.3737.

[42] M. Long, T. I. Weinberger, Z. Wu, M. F. Hansen, R. Tao, M. Shrestha, D. Graf, Y. Skourski, F. M. Grosche and A. G. Eaton, 3D bulk-resolved g-wave altermagnetic order parameter in CrSb, Nature **656**, 854–860 (2026). Published 26 August 2026. https://doi.org/10.1038/s41586-026-10902-z.

[43] J. Bardeen, L. N. Cooper and J. R. Schrieffer, Theory of Superconductivity, Physical Review **108**, 1175–1204 (1957). https://doi.org/10.1103/PhysRev.108.1175.

[44] B. D. Josephson, Possible new effects in superconductive tunnelling, Physics Letters **1**, 251–253 (1962). https://doi.org/10.1016/0031-9163(62)91369-0.

[45] I. I. Mazin, D. J. Singh, M. D. Johannes and M. H. Du, Unconventional Superconductivity with a Sign Reversal in the Order Parameter of $LaFeAsO_{1-x}F_x$, Physical Review Letters **101**, 057003 (2008). https://doi.org/10.1103/PhysRevLett.101.057003.

[46] C. C. Tsuei et al., Pairing Symmetry and Flux Quantization in a Tricrystal Superconducting Ring of $YBa_2Cu_3O_{7-\delta}$, Physical Review Letters **73**, 593–596 (1994). https://doi.org/10.1103/PhysRevLett.73.593.

[47] A. Pustogow et al., Constraints on the superconducting order parameter in Sr_2RuO_4 from oxygen-17 nuclear magnetic resonance, Nature **574**, 72–75 (2019). https://doi.org/10.1038/s41586-019-1596-2.

[48] A. Yu. Kitaev, Unpaired Majorana fermions in quantum wires, Physics–Uspekhi **44**, 131–136 (2001). https://arxiv.org/abs/cond-mat/0010440.

[49] N. Read and D. Green, Paired states of fermions in two dimensions with breaking of parity and time-reversal symmetries and the fractional quantum Hall effect, Physical Review B **61**, 10267–10297 (2000). https://doi.org/10.1103/PhysRevB.61.10267.

[50] R. M. Lutchyn, J. D. Sau and S. Das Sarma, Majorana Fermions and a Topological Phase Transition in Semiconductor-Superconductor Heterostructures, Physical Review Letters **105**, 077001 (2010). https://doi.org/10.1103/PhysRevLett.105.077001.

[51] L. Fu and C. L. Kane, Superconducting Proximity Effect and Majorana Fermions at the Surface of a Topological Insulator, Physical Review Letters **100**, 096407 (2008). https://doi.org/10.1103/PhysRevLett.100.096407.

[52] B. D. Woods, J. Chen, S. M. Frolov and T. D. Stanescu, Zero-energy pinning of topologically trivial bound states in multiband semiconductor-superconductor nanowires, Physical Review B **100**, 125407 (2019). https://doi.org/10.1103/PhysRevB.100.125407.

[53] D. L. Martin, Specific Heat of Copper, Silver, and Gold below 30 K, Physical Review B **8**, 5357–5360 (1973); erratum **10**, 5239 (1974). https://doi.org/10.1103/PhysRevB.8.5357.

[54] G. K. White and R. J. Tainsh, Lorenz Number for High-Purity Copper, Physical Review **119**, 1869 (1960). https://doi.org/10.1103/PhysRev.119.1869.

[55] A. T. Burkov, A. Heinrich, P. P. Konstantinov, T. Nakama, and K. Yagasaki, Experimental set-up for thermopower and resistivity measurements at 100–1300 K, Measurement Science and Technology **12**, 264–272 (2001), Table 2. https://doi.org/10.1088/0957-0233/12/3/304.

[56] K. S. Novoselov, A. K. Geim, S. V. Morozov, D. Jiang, M. I. Katsnelson, I. V. Grigorieva, S. V. Dubonos, and A. A. Firsov, Two-dimensional gas of massless Dirac fermions in graphene, Nature **438**, 197–200 (2005), Fig. 3(c–e). https://doi.org/10.1038/nature04233; author manuscript https://arxiv.org/abs/cond-mat/0509330.

[57] M. Long et al., Research data supporting "3D bulk-resolved g-wave altermagnetic order parameter in CrSb", University of Cambridge Apollo Repository (2026). Files `fig4b.csv` and `fig4c.csv`; CC BY 4.0. https://doi.org/10.17863/CAM.131869.

[58] Y. Zhang, Y.-W. Tan, H. L. Stormer, and P. Kim, Experimental observation of the quantum Hall effect and Berry's phase in graphene, Nature **438**, 201–204 (2005), Fig. 2a. https://doi.org/10.1038/nature04235; author manuscript https://arxiv.org/abs/cond-mat/0509355.

[59] Y. K. Kato, R. C. Myers, A. C. Gossard, and D. D. Awschalom, Observation of the Spin Hall Effect in Semiconductors, Science **306**, 1910–1913 (2004), Fig. 1A,B. https://doi.org/10.1126/science.1105514.

[60] P. Townsend and J. Sutton, Investigation by Electron Tunneling of the Superconducting Energy Gaps in Nb, Ta, Sn, and Pb, Physical Review **128**, 591 (1962). https://doi.org/10.1103/PhysRev.128.591.

[61] H. F. Hess, R. B. Robinson, R. C. Dynes, J. M. Valles, Jr., and J. V. Waszczak, Scanning-Tunneling-Microscope Observation of the Abrikosov Flux Lattice and the Density of States near and inside a Fluxoid, Physical Review Letters **62**, 214–216 (1989). https://doi.org/10.1103/PhysRevLett.62.214.

[62] N. E. Phillips, Heat Capacity of Aluminum between 0.1 K and 4.0 K, Physical Review **114**, 676 (1959), issue 3. https://doi.org/10.1103/PhysRev.114.676.